1990

Scanning Tunnel Microscopy studies of tetrahedrally bonded materials

Patricia E. Allen
Iowa State University

Order Number 9100476

Scanning tunnel microscopy studies of tetrahedrally bonded materials

Allen, Patricia E., Ph.D.

Iowa State University, 1990

U·M·I
300 N. Zeeb Rd.
Ann Arbor, MI 48106

Scanning Tunnel Microscopy studies of tetrahedrally bonded materials

by

Patricia E. Allen

A Dissertation Submitted to the
Graduate Faculty in Partial Fulfillment of the
Requirements for the Degree of
DOCTOR OF PHILOSOPHY

Department: Physics
Major: Solid State Physics

Approved:

Signature was redacted for privacy.

Signature was redacted for privacy.

In Charge of Major Work

Signature was redacted for privacy.

For the Major Department

Signature was redacted for privacy.

For the Graduate College

Iowa State University
Ames, Iowa
1990

TABLE OF CONTENTS

LIST OF FIGURES

LIST OF TABLES

DEDICATION

IN MEMORY

OF

MARK ALBERS

I. INTRODUCTION

A. Opening Comments

One of the major areas in solid state physics and chemistry to experience considerable growth in recent years is that of surface science.[1-4] Advances in vacuum technology and cleaning techniques have helped to generate and maintain atomically clean surfaces. Since "cleaning" can be achieved by cleaving or sputtering the surface, ultra high vacuum (UHV) systems with pressures, in the range of 10^{-10} torr or less, can maintain a clean surface for an hour or longer, which is necessary to study the material without contamination.

The surface is understood to be that region 5 to 15 Å on either side of the outermost plane of atoms. The bulk electronic properties are recovered within a few monolayers (~ 15 Å or more) of the surface, unless the surface is charged, as is often the situation with semiconductors and insulators. The interactions at the surface are the same as for the bulk: Coulomb's law, the wave equation and Pauli's principle. The surface boundary conditions, on the other hand, are different than for the bulk, resulting in new phenomena: structural relaxation and reconstruction, steps and other surface unique defects, adsorption, surface bonds, two-dimensional phase transitions, etc.

When working with surfaces, some of the problems encountered in technology today include: catalysis, crystal growth, oxidation and corrosion. Another area of technological importance is semiconductor device behavior which depends on the interface that is formed between

semiconductors and either:

a) metals (as for Schottky barrier diodes);

b) insulators (as for metal-insulator-semiconductor (MIS) devices); or

c) semiconconductor-semiconductor heterostructures. The physical and chemical properties of these surfaces and interfaces are sensitive to, and in some cases determined by, random roughness or surface disorder.[5] Experimental knowledge of the atomic structure of the surface is imperative, then, to understand the formation of the surface and its properties.

For crystalline surfaces, there are a variety of techniques that can be used to determine surface characteristics and behavior. LEED (low energy electron diffraction) is one of the most important structural methods available. Other methods include atomic beam scattering, FIM (field ion microscopy) and RHEED (reflection high energy electron diffraction). For polycrystalline, amorphous or inhomogeneous surfaces, however, the high resolution methods are limited mainly to versions of the electron microscope. The SEM (scanning electron microscope) has a resolution of approximately 100 Å. Higher resolutions (~ 2 Å) can be obtained with the TEM (transmission electron microscope), but preparing the thin films (~ 100 Å) required for study has been a problem experimentally.

The Scanning Tunnel Microscope (STM) is a real-time method for determining surface structure for periodic and non-periodic surfaces. It can provide electronic and geometric information about a surface while

other surface tools yield only one or the other. It is a very local, non-destructive, high resolution tool that, in conjunction with other techniques, can provide a plethora of information about surfaces. The resolution limits of various microscopes are compared in Figure 1.1.[6]

B. Historical Overview

The Scanning Tunnel Microscope is based on an effect that has been known for 60 years since R. H. Fowler and L. Nordheim[7] first used electron tunneling to explain electron emission from cold metals under the influence of a high external electric field. They were able to derive the current versus field relation which is shown in Figure 1.2.[8]

Gerd Binnig and Heinrich Rohrer used vacuum tunneling in combination with scanning as a new tool for the surface science work beginning at IBM Zurich. Vacuum tunneling was chosen because vacuum is the simplest barrier for tunneling.[9,10] Early devices such as the "stylus profilometer"[11] and the "topographiner"[12] contained the basic idea of the STM, but because of the difficulty in achieving the vibration isolation required for sub-nanometer resolution, the resolutions were not very different than the electron microscopes of the time.

The first generation STM used superconducting magnetic levitation of the tunnel unit combined with eddy current damping to minimize vibrations. Despite the complexity of the apparatus, in 1981, atomic steps on gold were obtained, with a resolution of approximately 2 Å instead of the expected resolution of approximately 45 Å.[13] This atomic resolution can be obtained with atomically large tips (~ 1,000 Å) because

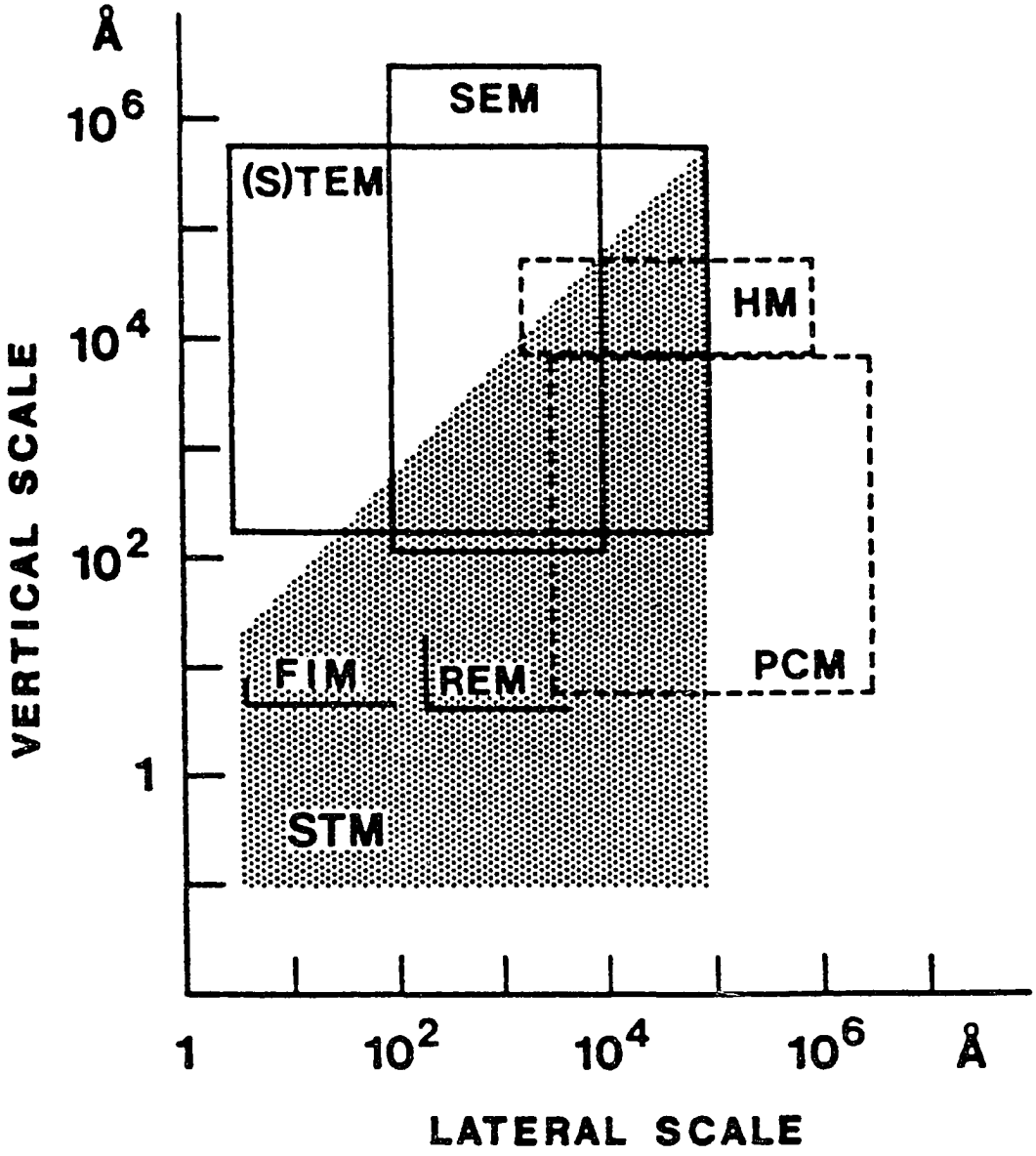

Figure 1.1. Comparison of resolutions of different microscopes. STM: shaded area. HM: high resolution optical microscope, PCM: phase contrast microscope, (S)TEM: (scanning) transmission electron microscope, SEM: scanning electron microscope, REM: reflection electron microscope and FIM: field ion microscope

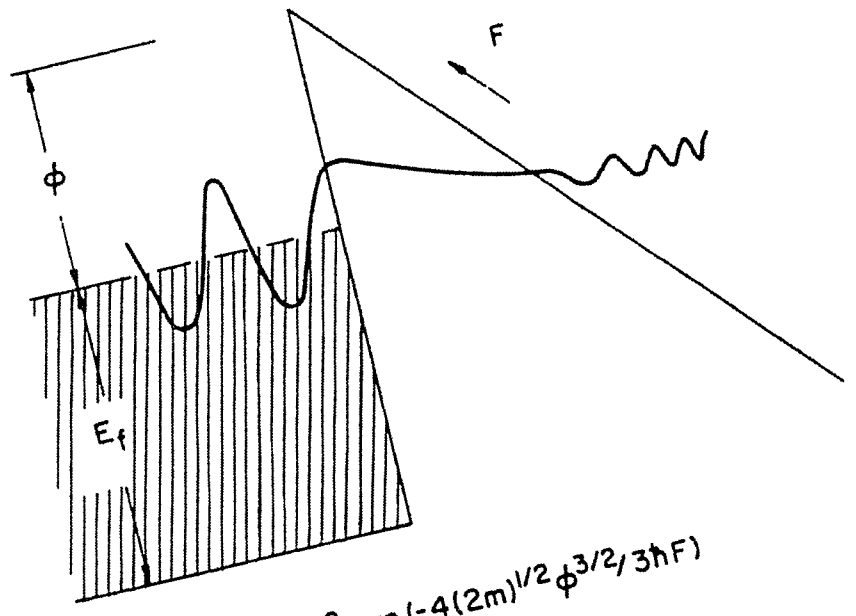

Figure 1.2. Fowler-Nordheim tunneling. Also shown is the current, J, versus field, F, relation

of the existence of "mini-tips."

The tunneling current depends exponentially on the distance separating two electrodes (refer to Section I.C.). In general, one mini-tip is closer to the surface than the others and is the main contributor to the current as demonstrated in Figure 1.3. These mini-tips are believed to possess only a few atoms close to the surface (thus supporting some of the theoretical work to be described in Chapter 2).

After their initial success with gold, Binnig et al. simplified their version of the STM and pursued one of the more interesting problems of the time: the 7x7 reconstruction of Si(111).[14,15] The Si(111) surface reconstructs to minimize the total energy by reducing the number of dangling bonds per unit cell,[16] but there existed some controversy as to the actual form of the reconstruction. Binnig and Rohrer's images of the Si(111) surface showed the surface atoms rearranged into a structure with basis vectors seven times longer than those that describe the bulk material, that is, the 7x7 reconstruction, as shown in Figure 1.4.[17]

The surface unit cells are diamond-shaped and characterized by deep depressions in the corners. One such unit cell is outlined in Figure 1.4. Each 7x7 cell contains 12 "bumps" that correspond to the surface of individual atoms. The two halves of the unit cell are dissimilar electronically due to an underlying stacking fault. This difference can be observed only for certain bias voltages and will be further described in Section I.D.

After Binnig's and Rohrer's results were made known, other groups investigated the Si(111) surface. Becker et al.[18] and Berghaus et al.[19]

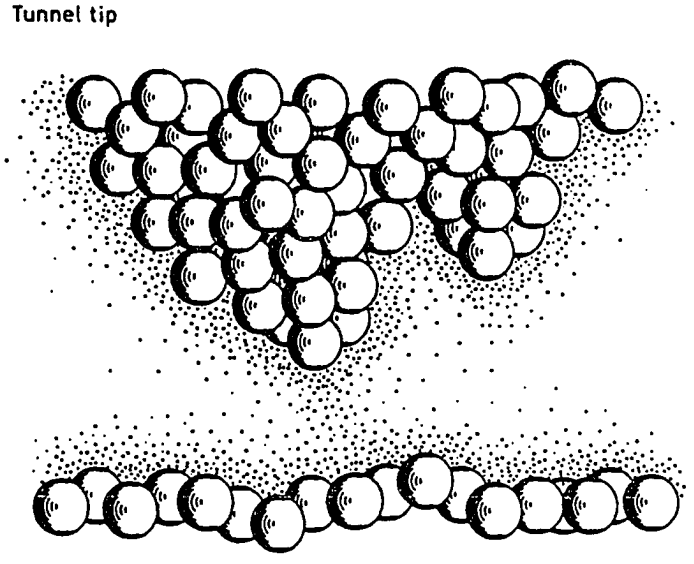

Figure 1.3. The tunnel tip showing the current contributions due to two "mini-tips"

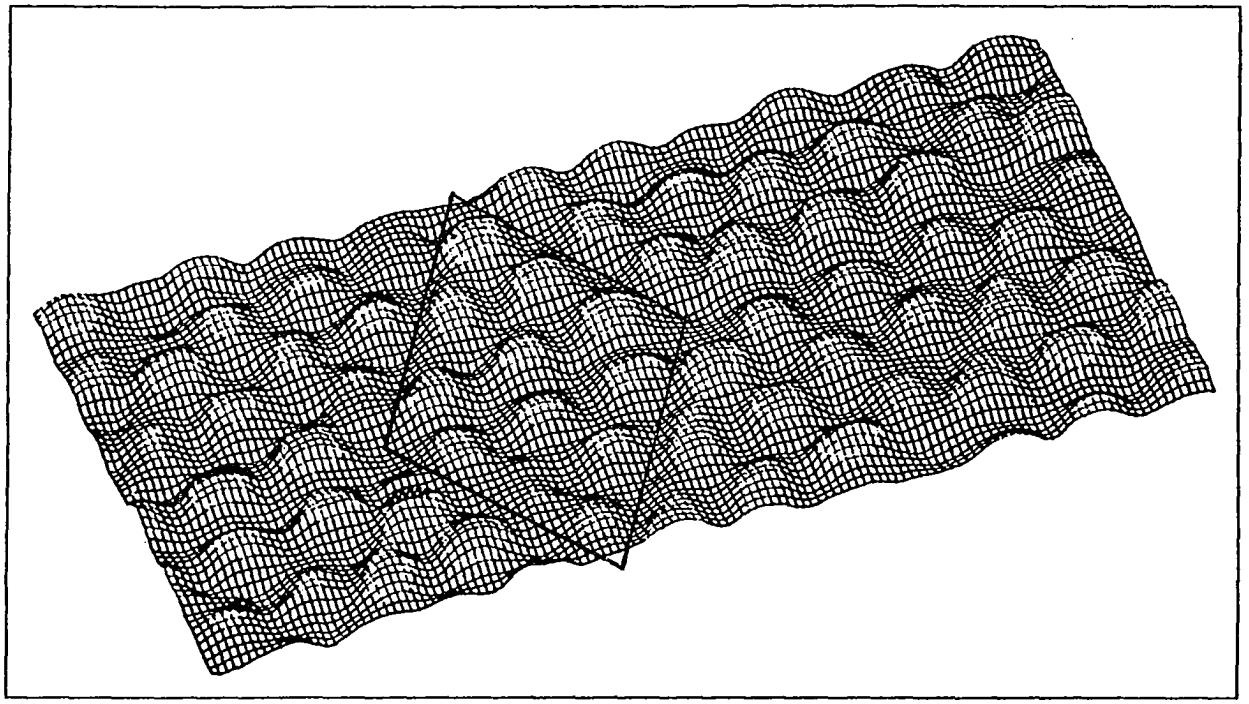

Figure 1.4. Surface of Silicon (111) showing the 7x7 reconstruction. One unit cell is outlined

observed atomic steps with the reconstruction extending to the step edge on both the upper and lower terrace, as seen in Figure 1.5. This resulted in the conclusion that the reconstruction begins at the step edges. The 7x7 experiments accelerated the first theoretical efforts of Scanning Tunneling Microscopy on a microscopic level. Some of the theoretical advances that have been made will be outlined in Chapter 2.

In 1986, the Nobel Prize in Physics was shared between Binnig and Rohrer and Ernst Ruska who built the first electron microscope in 1931.[20,21] Despite the similarity in both obtaining atomic resolution, half a century separates the two inventions and the methods of operation are completely different. The Swedish Academy did not explain this particular combination, but noted that in one case it was honoring a promise fulfilled and in the other honoring a promising future.

C. Basic Operation

The basic operation of the Scanning Tunnel Microscope depends on the quantum mechanical property of electron tunneling which allows, on the atomic scale, electrons to penetrate into classically forbidden regions in space. The one-dimensional relationship[22] between the tunneling current, I, and the distance, d, separating two electrodes is given by

$$I \propto V \exp(-2\kappa d) \tag{1.1}$$

where V is the potential across the electrodes and κ is the decay constant. For vacuum tunneling,

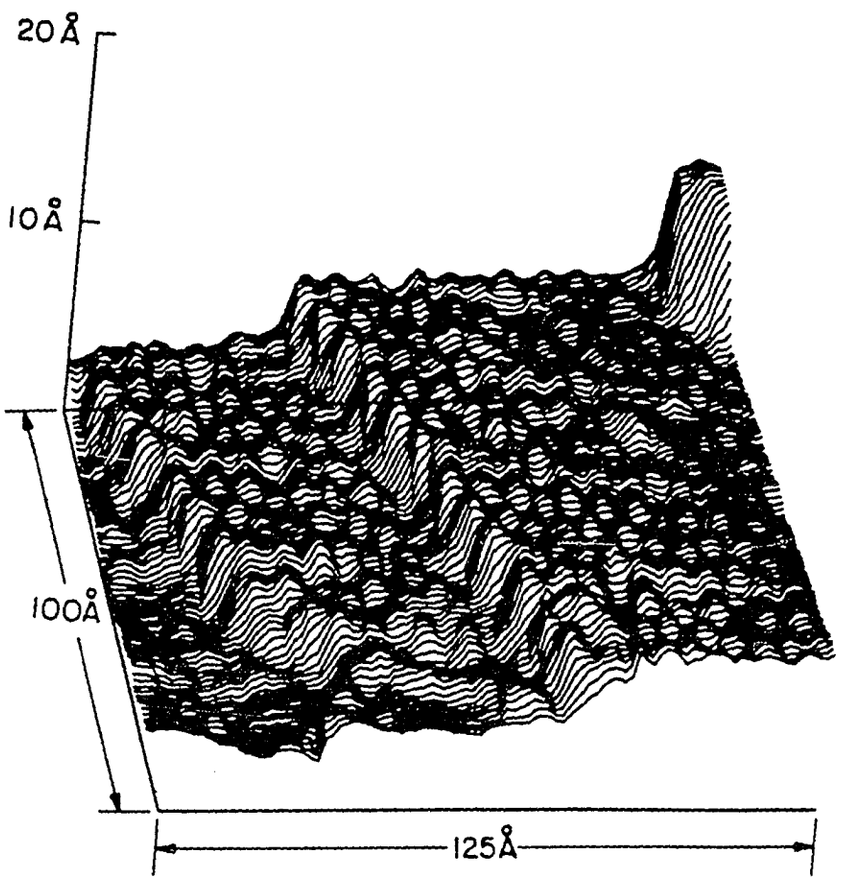

Figure 1.5. Atomic steps on a Si(111) 7x7 reconstructed surface

$$2\kappa = 2\ (8\pi^2 m\ \phi/h^2)^{1/2} = 1.025\ (\text{Å-eV}^{1/2})^{-1}\ \phi^{1/2} \qquad (1.2)$$

where ϕ is the barrier height or average work function and m is the electron mass. Using $\phi \sim 4$ eV (a typical value for metals) in Eq. (1.1), it is easy to see that for a 1 Å change in separation, the current changes by one order of magnitude. This sensitivity of tunnel current to distance variations is the basis of STM operation. By keeping I constant to within 2%, sub-angstrom resolution (0.01 Å) is possible in the z direction.[23]

To achieve vacuum tunneling, a metallic tip (usually tungsten or a platinum alloy), mounted on a piezoelectric transducer (PET) is mechanically brought close enough to the sample for tunneling to begin when a bias voltage (anywhere from 1 mV to 2 V) is applied. Piezoelectric ceramics are used for the transducers to provide a frictionless link between electronics and mechanics.

To avoid accidental contact of tip and sample, it is important that the sample and tip approach be vibration-free. Binnig and Rohrer developed a rough drive, the "louse" (refer to Figure 1.6),[24,25] to move the sample toward the tip. The louse consists of a piezoplate resting on three metal feet that are clamped electrostatically. The louse moves when voltages are applied to the feet in an appropriate sequence and the piezoplate contracts or expands in response to the voltages. The sample then "walks" toward the tip in increments (typically sub-micron) depending upon the applied voltages and the sequence of clamping and unclamping of the feet. Other arrangements for rough positioning are

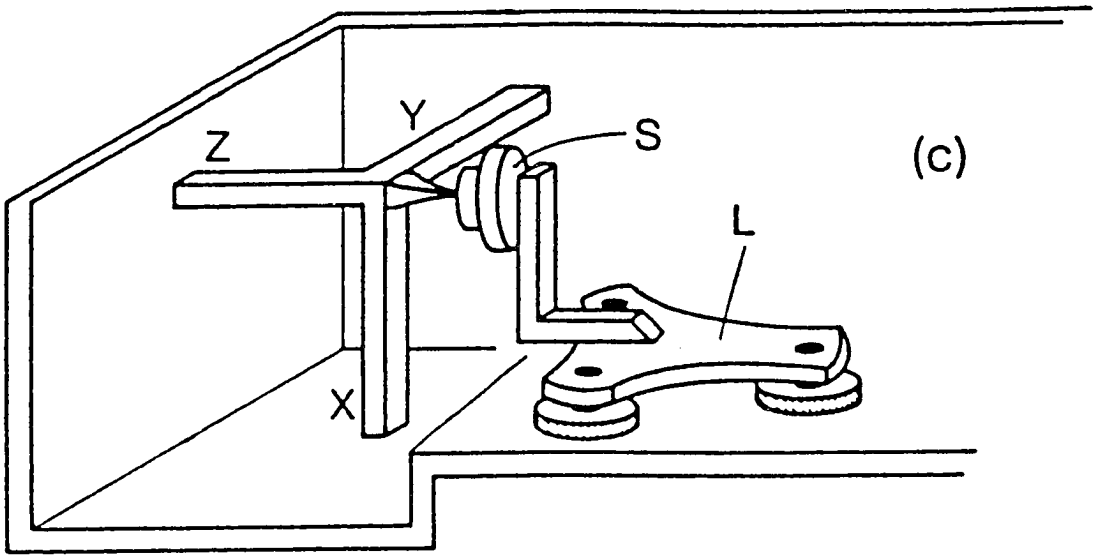

Figure 1.6. Schematic of the STM showing the rectangular PET at left and the "louse," L, for rough positioning of sample, S, at right

available, including the micropositioner approach used for this paper.

Once the tip is within tunneling range (5-10 Å), it can be scanned parallel to a surface by varying the voltages applied to the X and Y piezo's. The current is monitored by a feedback network which varies the voltage on the Z piezo to keep the current constant (see Figure 1.7). A typical value for the current is 1 nA. For a constant work function across the surface, this amounts to keeping the separation between tip and sample constant. The resulting STM image is a mapping of the Z piezo voltage (recorded as tip height, z) as a function of lateral position x and y. The tip height, z, is related to the Z piezo voltage by the piezoelectric constant, which is material dependent. This mode of operation is known as the constant current or topographic mode.

D. Applications

The topographic mode was the first historically, and is the most basic and commonly used mode of operation. For clean metal surfaces, the STM images correspond qualitatively with surface structures.[25,26] In addition to the topographic mode, the STM can be used for surface study in a variety of ways. The constant height mode is very useful for flat regions and/or fast scanning. In this mode, the height remains fixed at an "average" current value while the surface is scanned at a rate faster than the feedback loop can compensate. The change in current versus position is then recorded as shown in Figure 1.8.

One major advantage of the constant current mode is the speed with which a scan can be made, resulting in images that are less influenced by

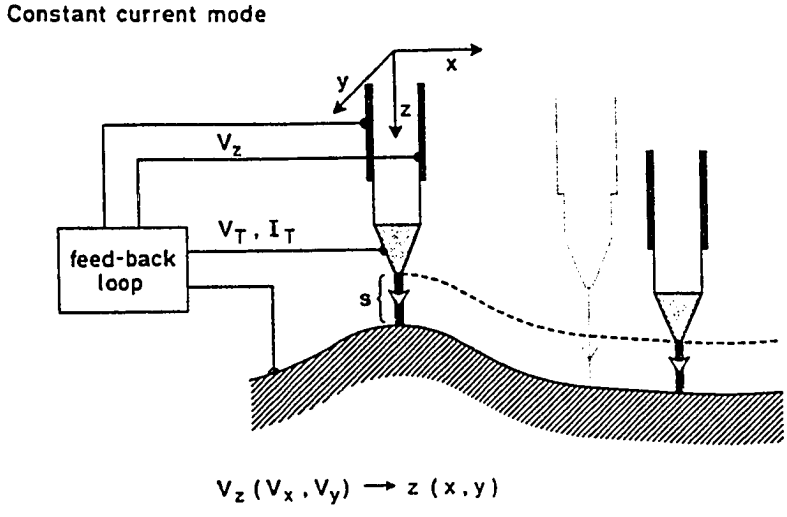

Figure 1.7. Constant current scanning schematic

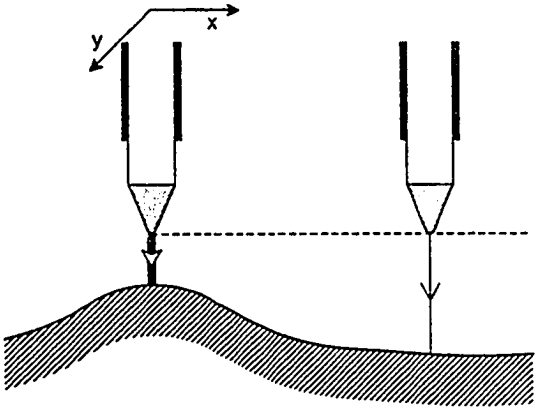

Figure 1.8. Constant height imaging

noise and thermal drift. (The scan speed is ultimately determined by the mechanical eigenfrequencies of the microscope itself.) For rough surfaces though, this mode will result in the tip crashing into surface features due to the inability of the feedback loop to adjust for large height variations.

By modulating the Z piezo voltage or the sample bias voltage, two additional applications are available. In either situation, a lock-in amplifier is used to synchronize the current variations with the input modulation. The resulting images provide information about the electronic structure of the surface. In both cases, Equation 1.1 holds the key to understanding the effects of a modulation signal applied to the STM.

1. Barrier Height Measurements

Modulation of the Z piezo voltage (or conversely, the electrode separation) results in barrier height measurements. For small modulations[6,24,27] in the electrode separation,

$$\frac{d\ln I}{ds} \propto \phi^{1/2} \tag{1.3}$$

Typical values for the modulating signal are a sine wave frequency of 5 kHz to 25 kHz with an amplitude of 0.1 volts peak-to-peak or less. The modulation frequency must be greater than the lowest mechanical eigenfrequency to avoid the introduction of unwanted oscillations.

Equation 1.3 indicates that the resulting signal is a function of the local work function or local barrier height. In this manner, the

spatial variation in the local barrier height can be obtained. This technique can be used to identify the existence of structures and/or differences in chemical species that the topography alone can not provide. Figure 1.9 shows the STM topography and the work-function scans for Au islands on silicon. The barrier height scans in this example are more sensitive to the locations of the Au islands than the conventional topographic scans.

2. Tunneling Spectroscopy

The most powerful and "quantitative" mode is the spectroscopic mode. Ever since the Nobel-prize winning research of I. Giaever,[28] tunneling spectroscopy has been used to obtain information about superconductors.[29] Because of the low temperatures involved, superconductors were nearly the ideal material with which to observe and utilize tunneling properties. With the development of the STM, other materials are now accessible to tunneling spectroscopy.

At present, there are two main methods of obtaining spectroscopic information. Both provide information about the local electronic density of states (DOS) of the surface from the dependence of the current on bias voltage. The one method involves linearly ramping the bias voltage over a suitable range (usually a few volts) and superimposing a small modulating voltage (around 0.1 V_{p-p} or less). The tunnel current along with the voltage modulation is connected to a lock-in amplifier. By examining the differential conductance, $d\bar{I}/dV$ of the resulting output, important features show up as peaks which are then related to the surface

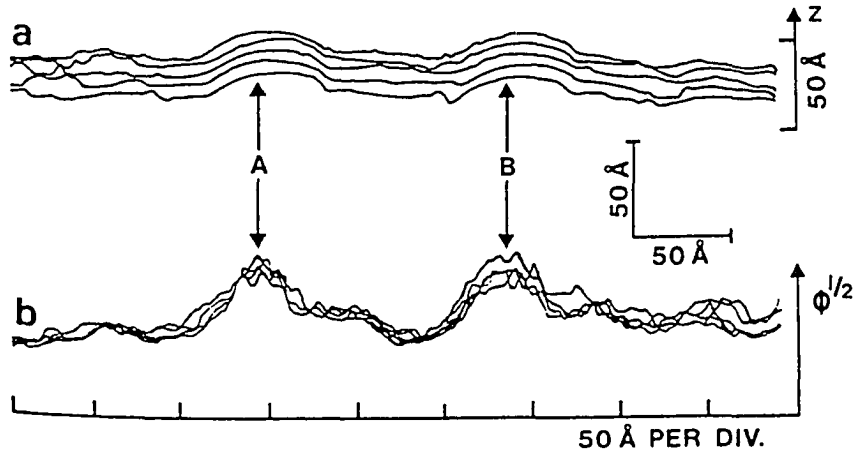

Figure 1.9. Au islands on Si: a) STM topography; b) corresponding work-function scans

density of states (the peaks define energies where the DOS is high).[30] The main limitation of this method is that it is performed only at selected points of the surface. On the other hand, it does allow for a wide range of bias voltages to be covered.

The alternate method combines imaging with spectroscopy. Tromp and coworkers developed one such combination which they named Current Imaging Tunneling Spectroscopy (CITS).[16,31-35] A sample and hold switch interrupts the feedback circuit at each scanned point at which time the current corresponding to various bias voltages is collected. The feedback circuit is re-engaged as the tip is moved to a new point and the process is repeated. When a scan is completed, there are n+1 images stored corresponding to n current images plus one topograph. The images at different bias voltages correspond to different DOS resulting in a spatially resolved map of bonding and/or antibonding orbitals.

Spectroscopy became a factor during the Si(111) 7x7 studies. The 7x7 images were seen to depend upon the magnitude and polarity of the bias voltage. Figure 1.10 shows the effect of polarity and Figure 1.11 the effect of both magnitude and polarity. As a result of such work, the STM images were found to be in excellent agreement with total charge density calculations for the dimer-adatom-stacking (DAS) fault model of Takayanagi et al.[36] For bias voltages of +2 V, the 7x7 images appear to reflect the geometric positions of the silicon surface atoms. In addition, conductance-voltage (σ-V) measurements revealed step-like onsets in the conductance that agreed with the energies of the peaks in the surface DOS as determined from photoemission and inverse

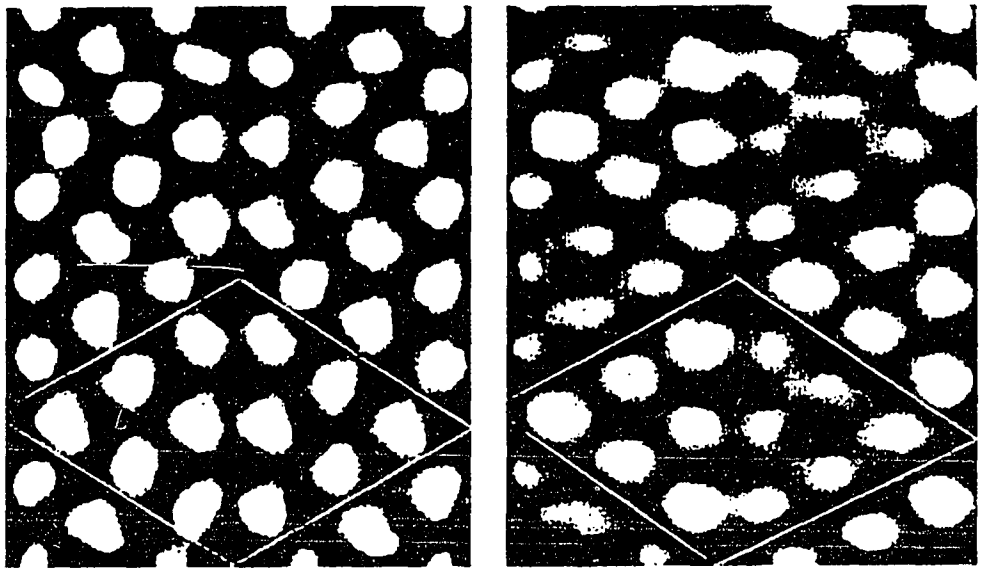

Figure 1.10. Bias dependent images of Si(111) 7x7 for +2 V on the sample (left) and -2 V on the sample (right). Under these bias conditions electrons tunnel into the sample or tip, respectively

Figure 1.11. Si(111) 7x7 images with applied voltages of:
A) -0.15 V; B) -0.25 V; C) -0.65 V; D) -0.75 V;
E) -0.95 V; F) -1.55 V; G) -2.00 V; H) +0.15 V;
I) +0.25 V; J) +0.65 V; K) +0.75 V; L) +0.95 V;
M) +1.55 V; N) +2.00 V

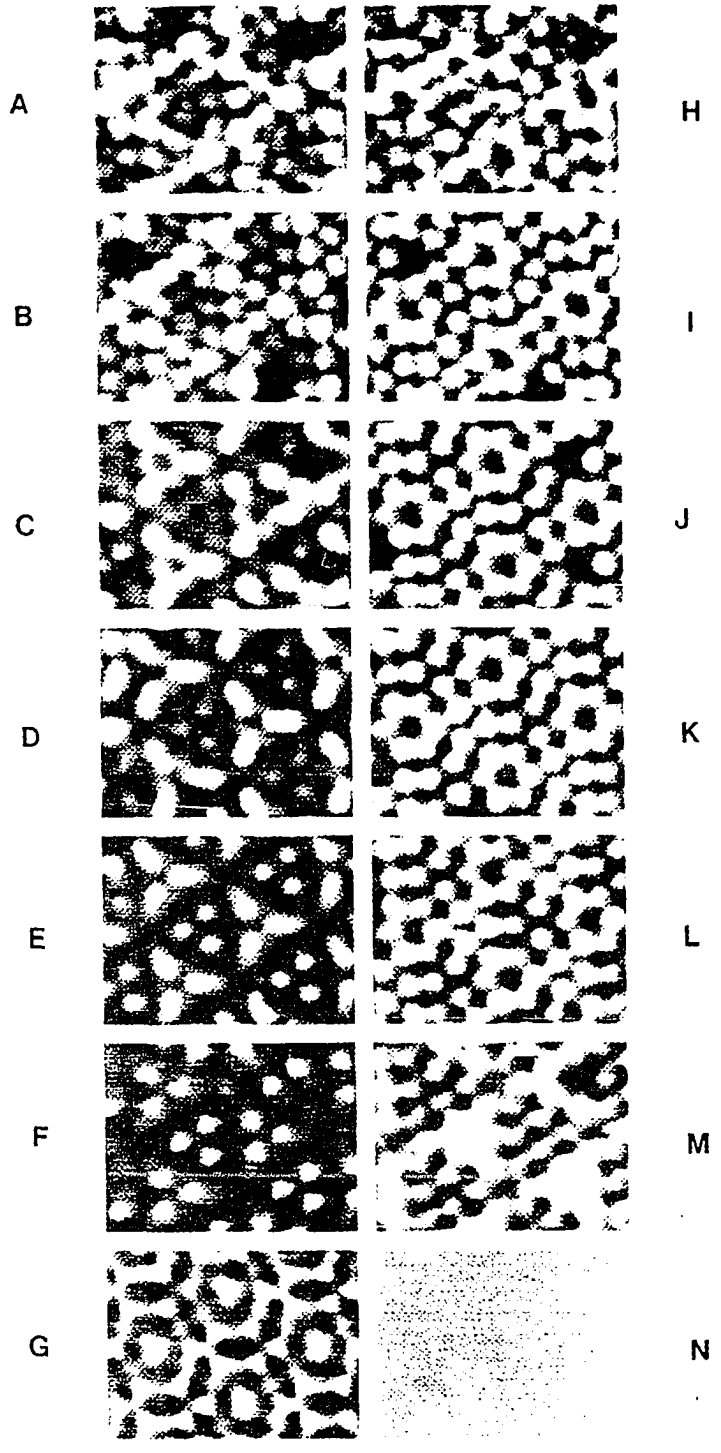
A
H
B
I
C
J
D
K
E
L
F
M
G
N

photoemission studies.[37,38] Figure 1.12[39] shows plots of σ, photoemission and inverse photoemission spectroscopies for the Si(111) 7x7 surface.

Other applications of the STM include lithography and surface modification,[40-42] micromanipulation of molecules,[43,44] and the study of biological material.[45] The STM can also be used to study low temperature effects as charge density waves and the spatial dependence of the superconducting energy gap.[46-49] An offshoot of the STM, the Atomic Force Microscope (AFM), may ultimately be the best tool for biological applications as well as for insulators[50-52] because of its ability to examine non-conductors.

E. Conclusions

One of the advantages of the STM is its simplicity of design and operation. It can be used to study the surfaces of metals, semiconductors, semimetals, etc., providing a real-time determination of surface structure including non-periodic structures. The materials can be studied under a variety of conditions: in vacuum, in air,[53] in cryogenic liquids,[54,55] in water,[56] in conductive solutions,[57] in oils or greases.[58] The surfaces can be sputtered or otherwise altered and the real-time effects recorded. Geometric, as well as electronic, information on the structure of the surface can be obtained; in some systems, they can be obtained simultaneously. In conjunction with other techniques (LEED, Auger, photoemission, etc.), a fairly complete picture of the surface can be generated.

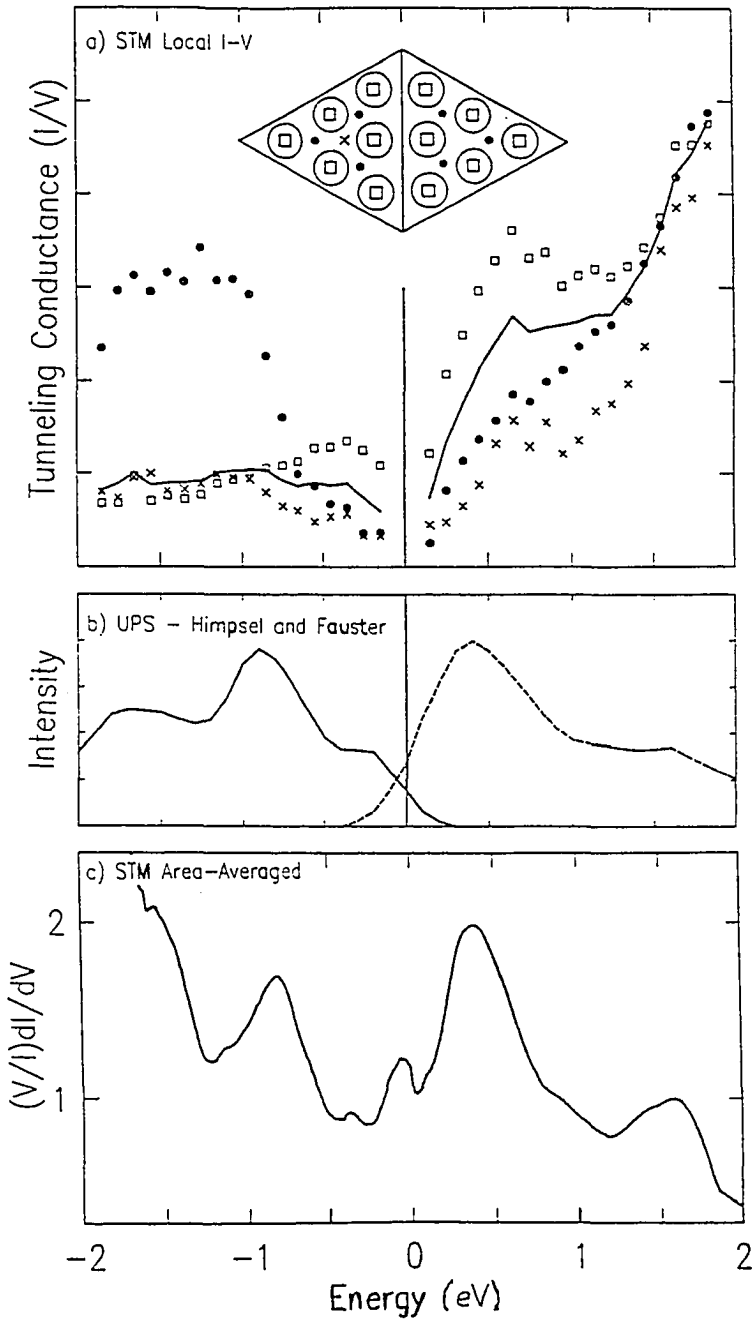

Figure 1.12. Tunneling conductance for Si(111): a) various locations within the 7x7 unit cell and c) normalized spectrum averaged over an area covering many unit cells. Also shown in b) are the photoemission and inverse photoemission results for comparison

The biggest disadvantage of the STM is the relative lack of theoretical information pertaining to the structure of various surfaces, including the electronic properties. In addition, the role of the tip presents one of the major stumbling blocks in interpreting the STM images (refer to Section IV.B). Many theorists are addressing this issue and are having some success with the increase in computing power.

Despite its youth, compared to methods such as the electron microscope or LEED, the STM and its offspring[59,60] (the AFM, Scanning Thermal Microscope, etc.) have had a large impact in the areas of biology, material science, surface physics and chemistry. The future role of the STM holds one of promise and excitement.

II. THEORY

A. Introduction

The theory required to explain the images obtained from STM research is still in its infancy. The basic tenets of tunneling have been known since the beginnings of quantum theory,[61] which has resulted in a qualitative correlation between the surface and the STM images, as observed for most metals. The problem arises when trying to separate the variety of factors contributing to the tunnel current, which is necessary to achieve a complete and quantitative understanding of the surface electronic and geometric properties. This is of particular interest in the understanding of semiconductor materials. Beginning with the basic concepts, the theory of tunneling microscopy will be traced to its present status with some emphasis placed on the areas yet to be developed.

B. One-Dimensional Tunneling

Classically, the probability that an electron can penetrate a one-dimensional, potential barrier, is zero. From quantum mechanics, however, electrons can exist in forbidden regions because of the exponential dependence on distance of the wave properties of an electrode. When two electrodes are close enough for their wave properties to overlap, yet not be in physical contact, the electrons from one electrode have a finite, non-zero probability of reaching the other electrode by tunneling through the barrier.

For the generalized, one-dimensional barrier shown in Figure 2.1, the WKB (Wentzel-Kramers-Brillouin) approximation[21,62] can be used to determine the probability, $D(E_x)$, that an electron can tunnel through the barrier, $V(x)-E_x$,

$$D(E_x) = \exp\{-4\pi/h \int_{s_1(E_x)}^{s_2(E_x)} [2m^*(V(x)-E_x)]^{1/2}\, dx\} \qquad (2.1)$$

where m^* is the electron effective mass and E_x is the energy component of the incident electron in the x direction and is given by $E_x = mv_x^2/2$. The classical turning points are given by s_1 and s_2. (The total energy and the transverse wavevector, $\mathbf{k}$, are conserved.)

For the rectangular barrier shown in Figure 2.2, the vacuum tunneling current, at small voltages and low temperature (to avoid dealing with thermal current), then has the form

$$I \propto \exp(-2\kappa s) \qquad (2.2)$$

where s is the distance between the electrodes and κ is the decay constant, given by

$$\kappa = 2\pi/h\ [2m(\bar{\phi})]^{1/2} \qquad (2.3)$$

where $\bar{\phi}$ is defined to be the mean barrier height, given by

$$\bar{\phi} = 1/\Delta s \int_{s_1}^{s_2} \phi(x)\, dx \qquad (2.4)$$

($\phi(x) = V(x)-\eta$).

The one-dimensional model adequately describes the qualitative behavior of the tunnel current, but it fails to address many of the important details that can influence the measured current. Some of these

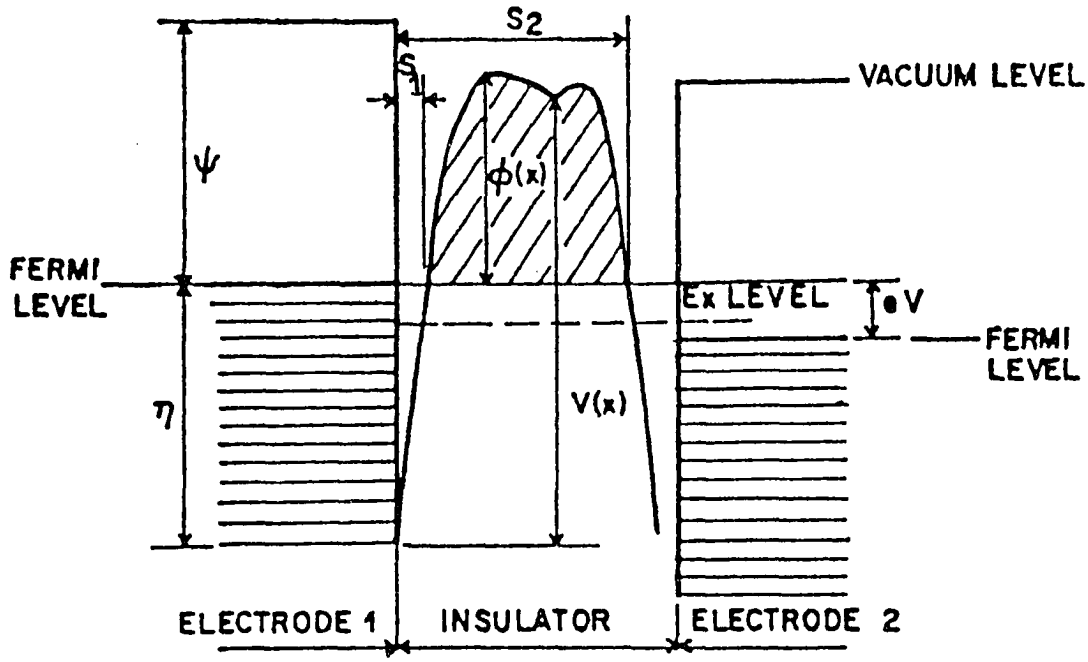

Figure 2.1. Generalized barrier between two electrodes.
s = thickness of insulating film
s_1, s_2 = limits of barrier at Fermi-level
V = voltage across film
η = Fermi level
ψ = metal electrode work function
$\phi(x)$ = barrier height function
V(x) = potential barrier

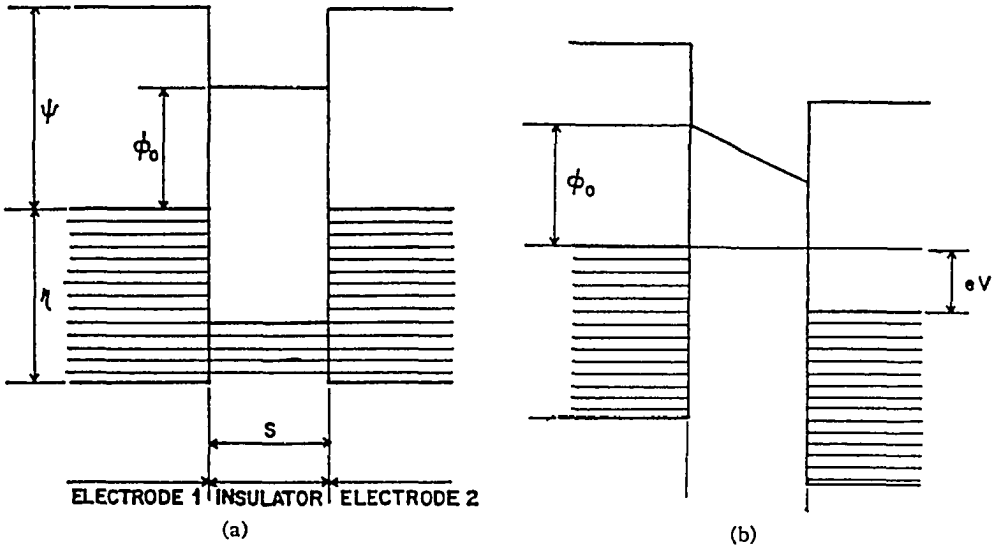

Figure 2.2. Rectangular potential barrier for: a) V = 0 and b) $V = \phi_o/e$

factors include: how s is measured, how the electronic structure of both the tip and the surface contribute to the current, what states are actually involved in the tunnel process, etc. To address these and other issues, a three-dimensional model is required.

C. Transfer Hamiltonian Formalism

The transfer Hamiltonian approach (first introduced by Bardeen to calculate the tunnel current)[63-65] is motivated by the fact that a near-unity probability of reflection by the barrier occurs in a typical tunnel structure, as shown in Figure 2.3. The barrier is then regarded as separating the system into two nearly independent regions coupled by a weakly perturbing Hamiltonian, H^T, which then drives the electron transitions from one side to the other according to the Golden Rule calculation, as given by

$$\omega_{\mu\nu} = \frac{4\pi^2}{h} |\langle\psi_\nu|H^T|\psi_\mu\rangle|^2 \rho(E_\nu) \delta(E_\nu - E_\mu) \qquad (2.5)$$

Equation 2.5 describes the transition rate, $\omega_{\mu\nu}$, from a given state μ (the left side of Figure 2.3) to a set of states of equal energy and density, $\rho(E_\nu)$, on the right.

The total set of wave functions for each electrode is assumed to be known, independently of the other (i.e., ψ_μ and ψ_ν are nonorthogonal eigenstates of different Hamiltonians). The wave function, ψ_μ, of the probe is taken as a standing wave normalized in the tip electrode and matched to an exponentially decaying wave in the barrier. Instead of oscillating in the region of the sample electrode, ψ_μ is assumed to decay

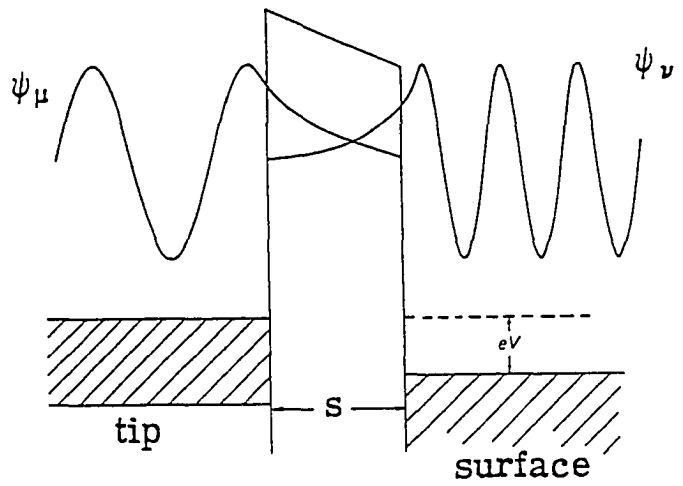

Figure 2.3. The tunneling Hamiltonian picture showing the exponential decrease of the wave-functions and the weak coupling in the barrier region

smoothly to zero. A similar expression applies for the sample wave function, ψ_ν. The wave functions ψ_μ and ψ_ν then overlap only in the barrier region.

Bardeen was able to show, using first-order perturbation theory, that the tunneling current is given by

$$I = \frac{4\pi^2 e}{h} \sum_{\mu,\nu} f(E_\mu)[1 - f(E_\nu + eV)] \, |M_{\mu\nu}|^2 \, \delta(E_\mu - E_\nu) \qquad (2.6)$$

where $M_{\mu\nu}$ is the tunneling matrix element, f(E) is the Fermi function, V is the potential across the barrier and E_μ is the energy of the state μ (in the absence of tunneling), where μ and ν run over all the states of the tip and surface, respectively.

Since most experiments are performed at room temperature, or below, and at small voltage (roughly 10 meV for metal-metal tunneling), the current can be rewritten[66] for the limit of small V and low temperature as

$$I = \frac{4\pi^2 e^2 V}{h} \sum_{\mu,\nu} |M_{\mu\nu}|^2 \, \delta(E_\nu - E_F) \, \delta(E_\nu - E_F) \qquad (2.7)$$

In the limit of small bias, the only states to contribute to the current are those near the Fermi-level.

The underlying problem with Equations 2.6 and 2.7 is calculating the matrix element, $M_{\mu\nu}$. Bardeen showed that $M_{\mu\nu}$ can be written in terms of the separate electrode wave functions, Ψ_μ and Ψ_ν. Namely,

$$M_{\mu\nu} = \frac{h^2}{8m\pi^2} \int dS \cdot (\Psi_\mu^* \nabla \Psi_\nu - \Psi_\nu \nabla \Psi_\mu^*) \qquad (2.8)$$

where the integral is over any surface in the barrier region. The

quantity in the paranthesis is the current operator.

In principle, only Equations 2.6 and 2.8 are required to calculate the tunnel current and, in turn, the STM image. The problem, though, with the above formulation in calculating the current is the convolution of the tip and surface electronic spectra in the expression for the tunnel matrix element. Without specific information about the tip (which is still experimentally and theoretically lacking at this time), information about the surface is difficult to obtain from the STM image alone. The method of J. Tersoff and D. R. Hamann[66,67] to approximate the effects of the tip and to examine the interpretations of STM images is the current method (pun intended) of choice in the theory of Scanning Tunnel Microscopy.

D. Present STM Theory: Tersoff and Hamann

The surface wave function can be written as a summation over all reciprocal lattice vectors of the surface;

$$\Psi_v=(1/\Omega_s)^{1/2} \sum_G a_G \exp[-(\kappa^2+|k_G|^2)^{1/2}z] \exp[i(k_G)\cdot x] \qquad (2.9)$$

where Ω_s is the sample volume, κ is defined above (Equation 2.3), and $k_G = k + G$, where k is the surface Bloch function and G is a reciprocal lattice vector. For non-periodic surfaces, the summation changes to an integral expression. The first few coefficients, a_G are of order unity.

In general, the tip wave function is not known, but Tersoff and Hamann observed that the ideal STM would have the greatest possible resolution and would measure properties of the unperturbed surface,

rather than the joint tip-surface system. This ideal tip would have localized potential and wave functions in the vicinity of the surface, so they assumed an asymptotic spherical form for Ψ_μ in the area of interest,

$$\Psi_\mu=(1/\Omega_t)^{1/2}\ c_t\kappa R\ (\kappa|r-r_o|)^{-1}\ e^{\kappa R}\ \exp(-\kappa|r-r_o|) \qquad (2.10)$$

where Ω_t is the tip volume, R is the tip radius of curvature, and κ is defined above. Figure 2.4 is a schematic picture of the tunneling apparatus conceived by Tersoff and Hamann. The electrode separation, s, is defined here as the distance of nearest approach. For simplicity, the work functions of the tip and surface are made equal. In addition, any angular dependence of Ψ_μ is ignored.

The tip wave function can be expanded into the same form as Equation 2.9 using

$$(\kappa r)^{-1}\exp^{-\kappa r} = \int d^2q\ b(q)\ \exp[-(\kappa^2+q^2)^{1/2}|z|]\ \exp(iq\cdot x) \qquad (2.11)$$

where

$$b(q) = 1/2\pi\kappa^2\ (1 + q^2/\kappa^2)^{-1/2} \qquad (2.12)$$

The tunnel matrix element can be found using the tip and surface wave functions, given in Equations 2.9 and 2.10, and then used to calculate the tunnel current,

$$I=\frac{32\pi^3V}{h}\left[\frac{e\phi R}{\kappa^2}\right]^2 D_t(E_F)\ \exp(2\kappa R)\ \sum_\nu|\Psi_\nu(r_o)|^2\delta(E_\nu-E_F) \qquad (2.13)$$

where $D_t(E_F)$ is the density of states per unit volume of the tip and r_o is the radius of curvature of the tip. This spherical tip model removes

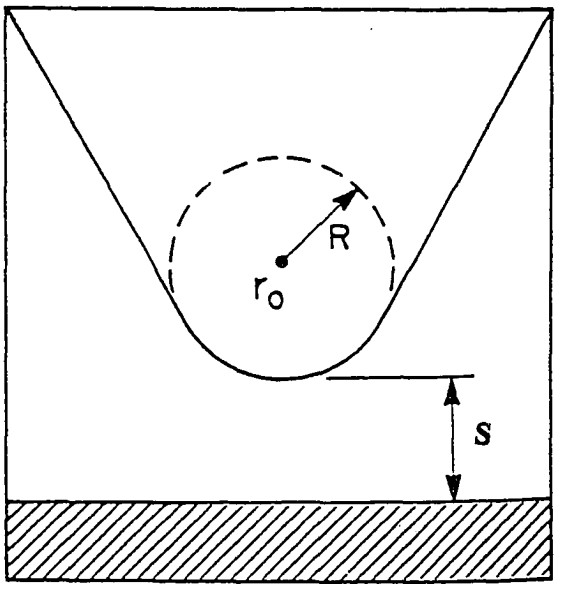

Figure 2.4. Schematic of tunneling geometry in the Tersoff and Hamann model

the tip properties from the calculations such that Equation 2.13 now depends only on the surface properties, as determined from Ψ_ν.

In the limit low temperature and small voltage, the tunneling conductance (chosen because, unlike the current, the conductance is independent of voltage in the limit of small voltage) is

$$\sigma \propto \rho(r_o, E_F) \tag{2.14}$$

where E_F is the Fermi energy and

$$\rho(r_o, E) \equiv \sum_\nu |\Psi_\nu(r_o)|^2 \, \delta(E_\nu - E) \tag{2.15}$$

is the surface local density of states (LDOS), or charge per unit energy from states of the surface at point r_o and energy E. From Equation 2.9, $|\Psi_\nu(r_o)|^2 \propto \exp[-2\kappa(R+s)]$ resulting in the expected behavior of $\sigma \propto \exp(-2\kappa s)$. The behavior of the state-density ($|\Psi_\nu(r_o)|^2$) with respect to the distance, z, from the surface is shown in Figure 2.5 for the bonding and anti-bonding states in the π-bonded models for the Si(111) 2x1 surface.[68]

In this limit, the current is proportional to the surface LDOS, that is, constant $\rho(r_o, E)$ at E_F at the tip position. The tip path then maps out a contour of constant Fermi-level LDOS of the bare surface. Lang[69-71] has shown that for an atomically sharp tip, the tip displacement closely follows the LDOS contour, as seen in Figure 2.6. In this manner, a property of the surface can then be used to calculate the STM images similar to the calculation of charge density. While due to the numerical complexity, few calculations have been made to date, two

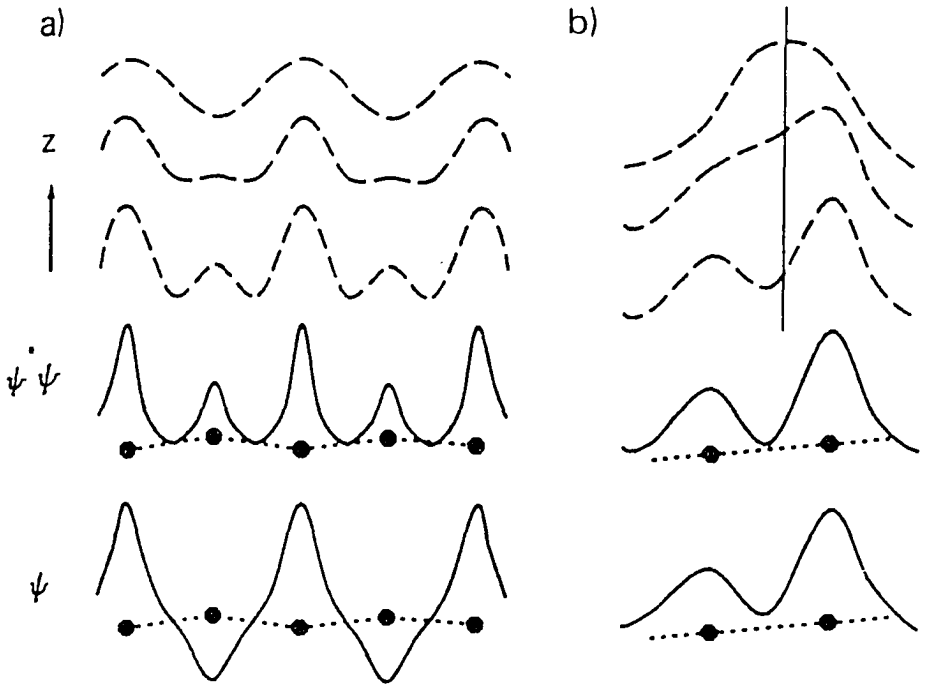

Figure 2.5. Schematic of the wave function, ψ, the state-density, $\psi^*\psi$, and the decay of the state-density with distance, z, from the surface for: a) antibonding states for π-bonded chain model and b) bonding states for π-bonded molecular model for Si(111) 2x1 surface

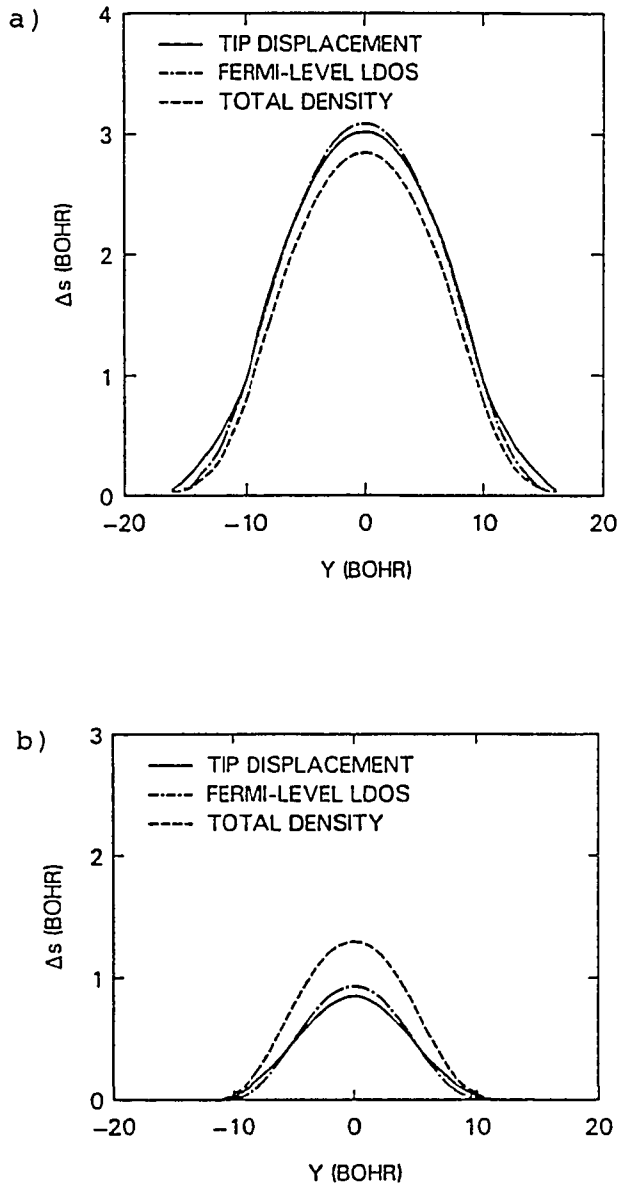

Figure 2.6. Tip displacement curves for: a) Na sample adatom (Na tip) and b) S sample adatom (Na tip). Contours of constant Fermi-level local density of states and constant total density are also shown

examples are considered in the next section.

As long as the tip wave functions at E_F can be approximated by an s-wave and $\mathbf{r}_o$ is taken at the center of curvature of the tip wave function, then the tip size is not a factor in the current expression. (Except in the case of large R, the higher l-wave components introduce only minor modifications.) The s-wave treatment of the tip is not intended to be an accurate description of the tip, but it is a useful method of parameterizing the effects of tip size on the resolution and sensitivity of the STM.

Because the STM image is a contour of constant $\rho(\mathbf{r}_o,E)$ of the surface, the behavior of $\rho(\mathbf{r}_o,E)$ is considered in more detail in the next section.

E. General Features of $\rho(\mathbf{r}_o,E)$

The surface wave function, ψ_ν, contributes a charge density, $|\psi_\nu|^2$ which has the periodicity of the lattice and can be Fourier expanded;

$$|\Psi_\nu|^2 = \sum_G u_{\nu G}(z)\ e^{iG\cdot r} \tag{2.16}$$

Similarly, the total $\rho(\mathbf{r},E)$ can be written as

$$\rho(\mathbf{r},E) = \sum_\nu |\Psi_\nu|^2\ \delta(E_\nu - E) = \sum_G \rho_G(z,E)\ e^{iG\cdot r} \tag{2.17}$$

where

$$\rho_G(z,E) = \sum_\nu u_{\nu G}(z)\ \delta(E_\nu - E) \tag{2.18}$$

For large $\mathbf{r}$, $\rho(\mathbf{r},E)$ becomes smooth and only the lowest non-zero Fourier components contribute. The task at hand then is to calculate $\rho(\mathbf{r},E)$ for a surface and to compare with experiment. Two such calculations are

presented below for the Au(110) surface.

The linear augmented plane wave (LAPW) method is first used to calculate $\rho(r,E)$ for the Au(110) 2x1 and 3x1 surfaces (refer to Reference 66 for details) as shown in Figure 2.7. The dashed line represents the tip path chosen to correspond with the corrugation observed by Binnig et al.,[15] resulting in an effective tip radius of 9 Å. Note the change of features of the contours as the distance increases.

For more complex structures, such as disordered surfaces, defects, impurities and steps, Atomic Superposition can be used to calculate $\rho(r,E)$. From Equations 2.16-2.18, $\rho(r,E)$ resembles the total charge density, $\rho(r)$, which can sometimes be approximated by the superposition of atomic charge densities,

$$\rho(r) = \sum_{R} \phi(r - R) \tag{2.19}$$

where $\phi(r)$ is the charge density of the free atom and R are the atomic positions. Equation 2.19 does not require a periodic lattice.

Assume

$$\rho(r,E) \approx \rho(r)/E_0 \tag{2.20}$$

To estimate E_0, write

$$\rho(r,E) \sim A \exp[-\frac{2\pi}{h} (2mE)^{1/2} z] \tag{2.21}$$

where A varies slightly with E over the range contributing to $\rho(r)$ and using

$$\rho(r) = \int_{-\infty}^{E_F} \rho(r,E)\, dE \tag{2.22}$$

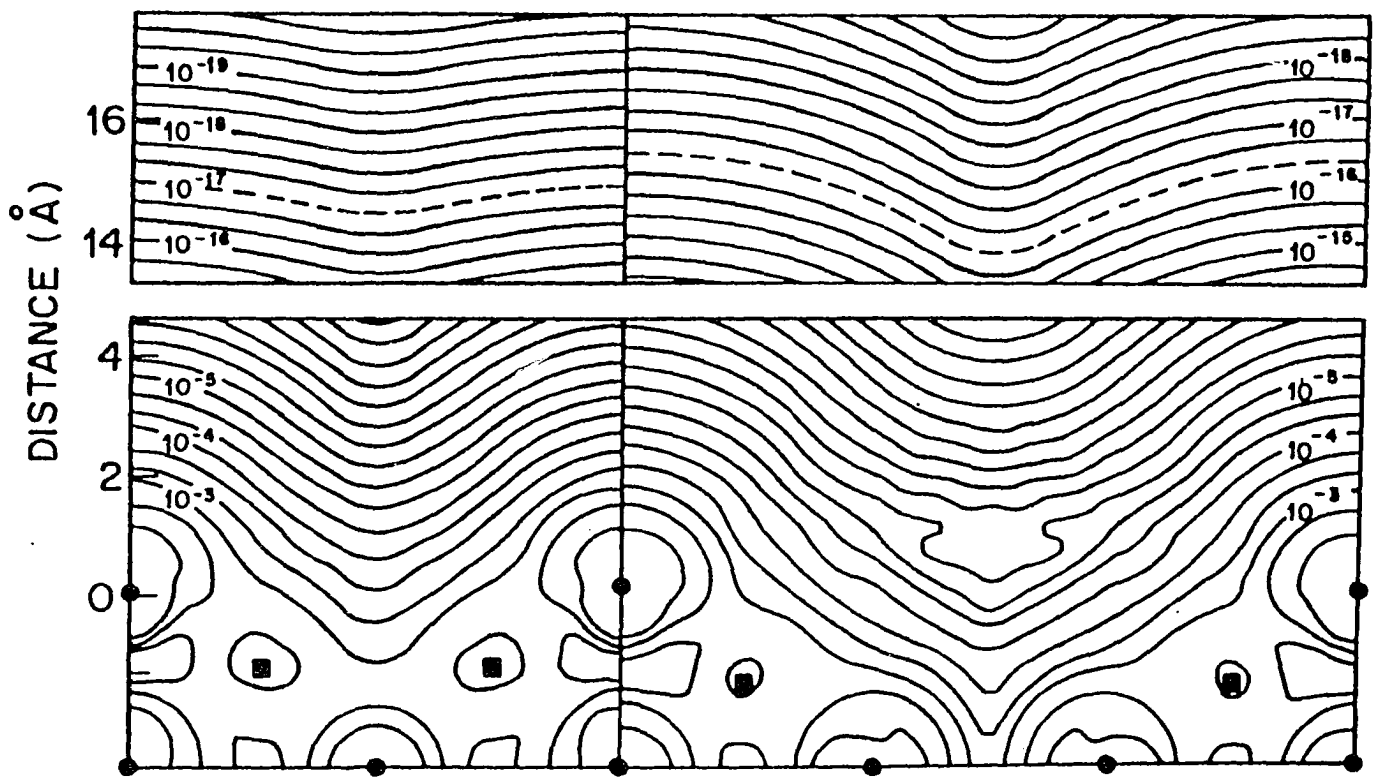

Figure 2.7. $\rho(r,E)$ calculated by LAPW for Au(110) 2x1 (left) and 3x1 (right) surfaces. Positions of outermost plane of nuclei are indicated by solid circles (in plane) and squares (out of plane). Contours of constant $\rho(r,E)$ are labeled in units of a.u.$^{-3}$eV^{-1}. Center of curvature of the tip follows the dashed contour

results in $E_o \approx E_F/\kappa z$ (assuming $\kappa z >> 1$ in order to expand $E^{1/2}$ about E_F).

Figure 2.8 shows the Atomic Superposition charge density for two geometries of the Au(110) 3x1 surface (also considered in right-hand side of Figure 2.7). Using a similar tip radius (9 Å) as for Figure 2.7, the tip would nearly follow the topmost contour. At this distance from the surface, it is nearly impossible to distinguish between the two geometries (in part due to relative inaccuracies of atomic superposition compared to self-consistent LAPW techniques). In this situation, alternative techniques, in conjunction with the STM images, are required to choose one geometry over the other.

One such approach is to improve the resolution in the system. The different contours obtained at different currents lead to an image of the electronic structure of the surface. While the Z resolution depends on instrument stability, the lateral resolution depends on the tip curvature, electrode separation, work functions of both tip and surface, microstructure of the tip, and the spatial extension of the surface state wave function.[72] Some of these issues are addressed in more detail by Lang's single-atom theory discussed in the next section.

F. Theory of Single-Atom Tunneling

The effects of single-atom imaging in Scanning Tunnel Microscopy have been realistically examined by N. D. Lang.[69-71] In his studies, Lang considered the behavior of the tunnel current between two metal electrodes, each with an adsorbed atom on its surface. The left-hand electrode, with adatom, S, is assumed to be the sample, while the right-

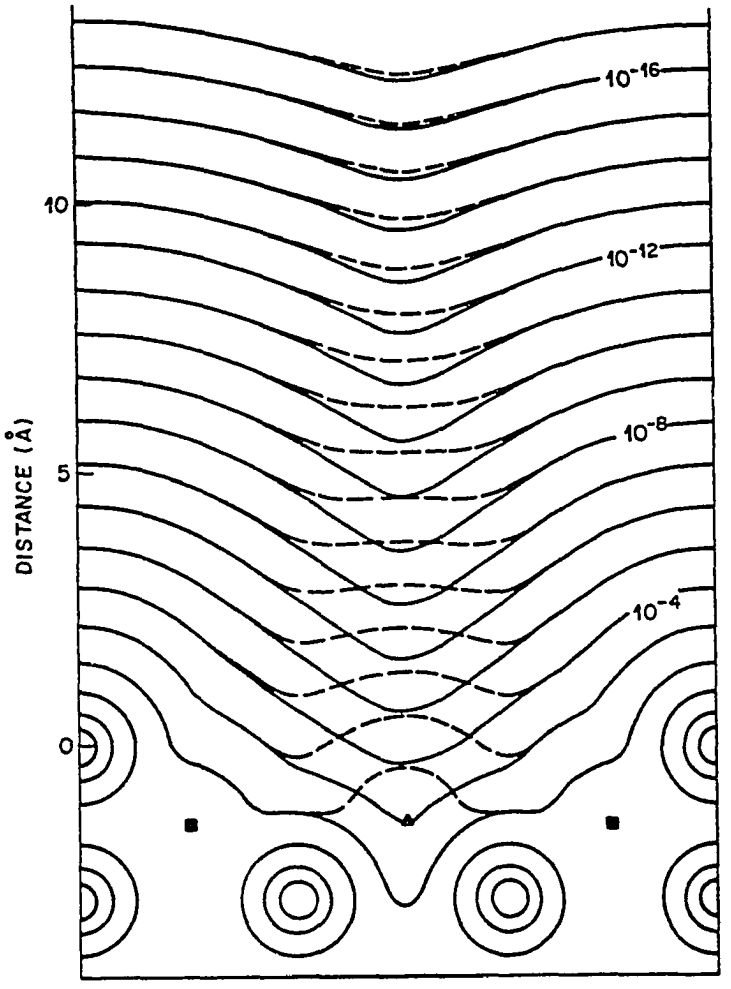

Figure 2.8. Atomic superposition charge density (a.u.$^{-3}$) for two possible geometries of Au(110) 3x1. Solid lines are for the same geometry as in Figure 2.7. Dashed lines are for geometry with no missing atom in the second layer. Triangle shows site of atom (out of plane of figure) present only in the latter case; squares show other out-of-plane atoms

hand electrode, with adatom, T, is the tip.

Lang developed an equivalent method to Bardeen's transfer-Hamiltonian formalism to calculate the current density distribution in terms of the wave functions which are determined separately for each electrode in the absence of the other. The jellium model, in cylindrical coordinates, is used for the metal surface because it yields adequate results for the properties that depend on the wave function well outside the surface. Both metal electrodes are taken to have the same high electron density, corresponding to $r_s=2$.

The difference in the eigenstate density between the metal-adatom system and the bare metal is shown in Figure 2.9. When the discrete, degenerate levels of the atom interact with the continuous electronic states of the metal, resonances occur in the state density, as seen by the 3p resonance peak for sulfur, S, and the 3s resonance peak for sodium, Na. The $m\neq0$ components are not considered because they make a much smaller contribution to the tunneling current than does the m=0 component.

For the two electrodes, each with their respective adatoms, let the total current between the electrodes be given by I_{ST}, and let I_S be the total current for the same arrangement in the absence of the T adatom. The quantity $\delta I=I_{ST}-I_S$ will then be sensitive to T being the tip. When the tip electrode is scanned past different atoms on the sample surface, these chemically different atoms produce different tunneling current behaviors. Figure 2.10 demonstrates this behavior for a Na tip and three sample adatoms: Na, S and He. The figure shows curves of tip distance,

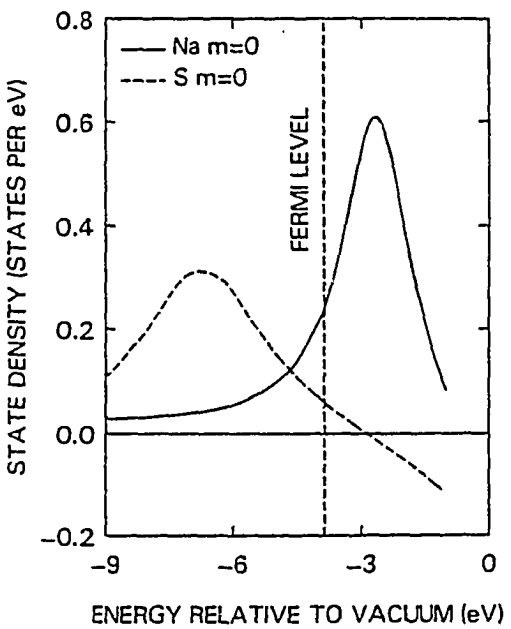

Figure 2.9. Curves of the difference in state density between metal-adatom system and the bare metal

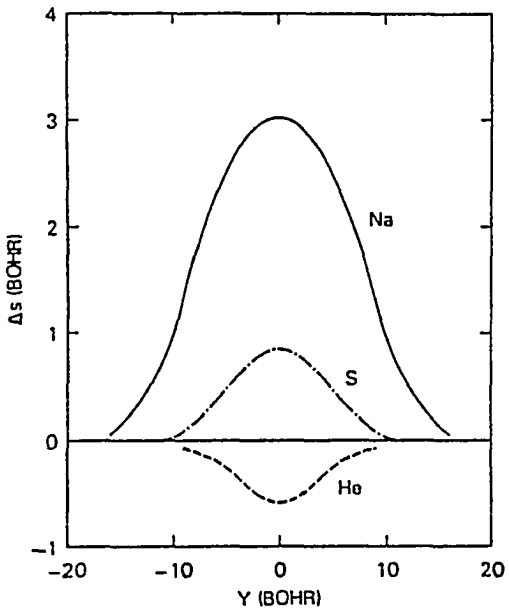

Figure 2.10. Plot of change in tip distance, Δs, versus Lateral separation, Y, for constant current. (1 bohr = 0.529 Å) Tip atom is Na, S and He

Δs, versus lateral separation, Y, of the adatoms for constant current, δI. (All distances are measured with respect to the nuclei of the adatoms.)

The maximum tip displacement is much smaller for S than for Na. This is due, in part, to the fact that S sits closer to the surface than Na, and, in part, to the fact that the Fermi-level state density for S is noticeably less than that for Na (refer to Figure 2.9). As mentioned in Section II.C, in the case of low bias, only the states near the Fermi-level contribute to the tunneling process.

In the situation with the He sample adatom, the tip displacement is actually negative despite the fact that the He atom sits further from the surface than does either S or Na. However, the closed valence shell is very far down in energy which polarizes the metal states away from the Fermi energy, producing a decrease in the Fermi-level state density and leads to the negative tip displacement. This could make an adsorbed molecule, with symmetry states similar to He, difficult to see with the STM because the negative tip displacement may be interpreted as a physical depression of the surface, instead of a change in the chemical properties.

The spatial distribution of the current can be found by considering the contour maps in Figure 2.11 of j_z/j_o for S and Na each, where j_z is the z-component of the current density and j_o is the current density in the absence of the other adatom. The left side of the contour maps mark the surface of the adatom electrode, while the right side is the other bare electrode. Results are given only for the center strip of the

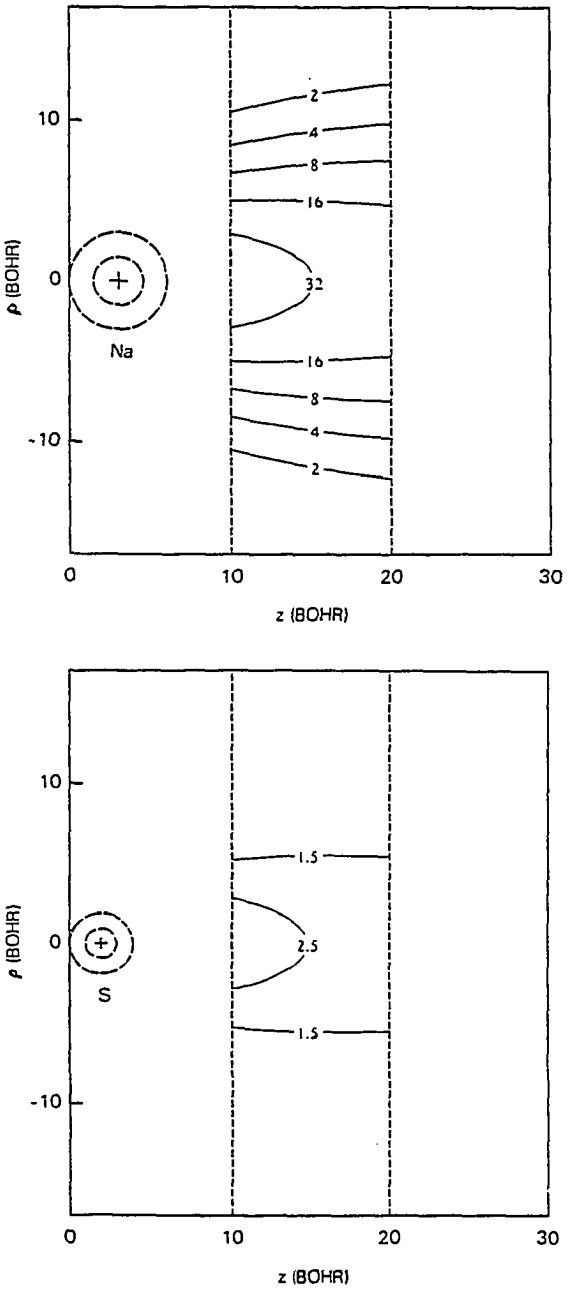

Figure 2.11. Contour map of j_z/j_o for a) Na and b) S atom adsorbed on the left electrode. The two dashed concentric circles with the cross in the center indicate the equilibrium distance of the nucleus

vacuum barrier because the equation used is not valid close to the surface (refer to Reference 69).

The contour maps show sharp peaks in the current distribution localized in the vicinity of the adsorbed atoms. (For Na, this enhancement is greater than for S because of the difference in the Fermi-level density, as described above.) This behavior around the adsorbed atom may indicate that the only contributors to the tunneling current are the atom being imaged, and the atom's nearest and next-nearest neighbors.

Current-density maps for the full two-atom case are shown for several values of Y in Figure 2.12. For large Y, the map is similar to Figure 2.11.a; the presence of S leads only to a small z-axis displacement of the Na tip. As Y is decreased, however, the displacement would have to grow to maintain constant current. With Y=0, the central channel narrows and the current between the electrodes is enhanced (the channel can be thought of as composed of two contours, one from each electrode).

Despite the simplicity of Lang's model, many experimental results can be explained in terms of single-atom tunneling: the enhancement of the tunnel current in the presence of an adatom (as well as its insensitivity, as in the case of He), the dependence of the current on the metal-adatom state density at the Fermi-level, and the spatial dependence of the total current density.

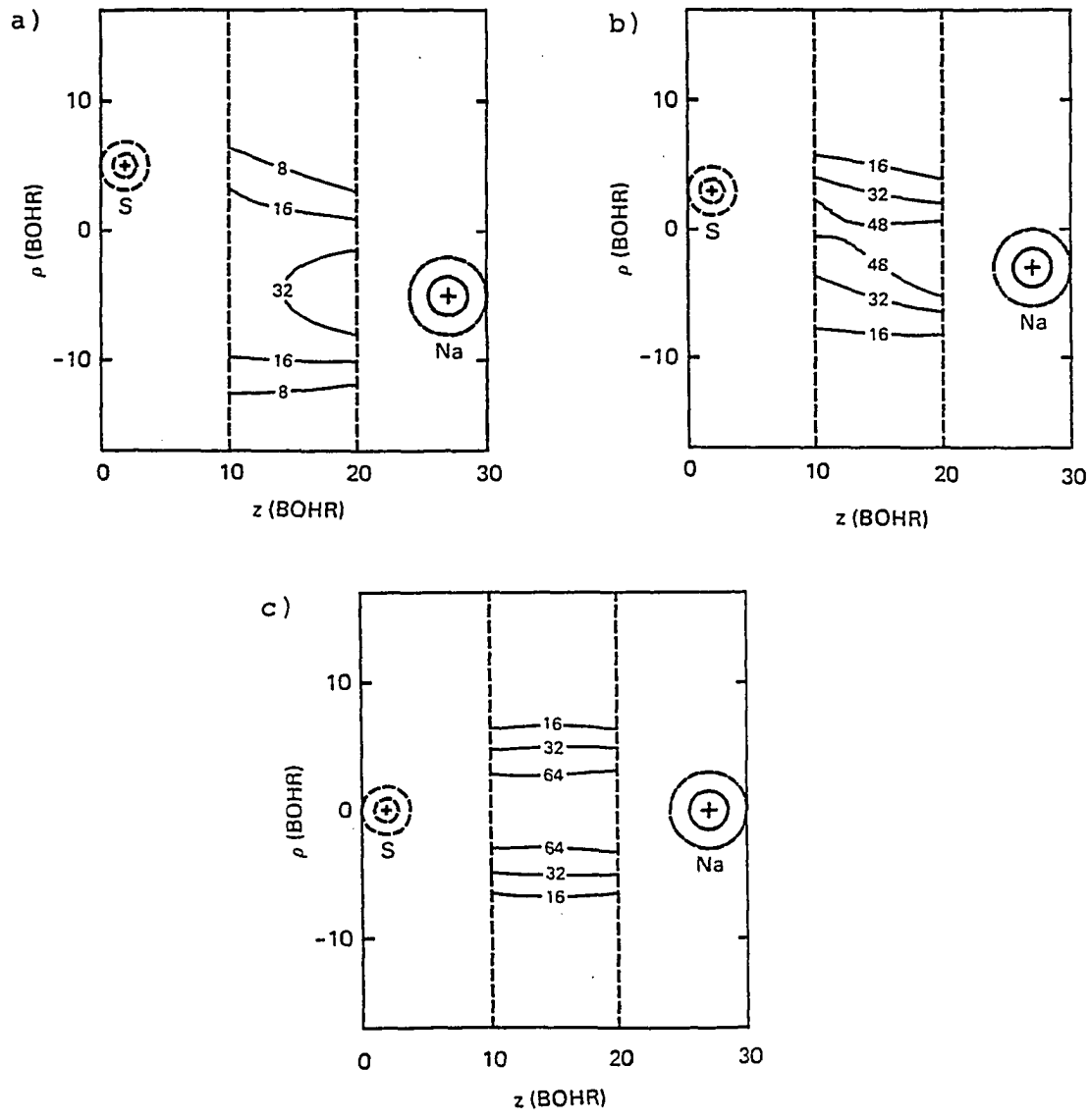

Figure 2.12. Contour maps of j_z/j_o for S adatom on the left electrode and Na adatom on the right electrode as a function of lateral separation, Y (measured in the plane normal to the surface that includes both atomic nuclei). a) 10, b) 6, and c) 0 bohrs (1 bohr = 0.529 Å)

G. Semiconductors

The tunneling picture alters slightly when considering the behavior of semiconducting surfaces. For the metal tip, the states below E_F are filled, while above E_F they are empty. Unlike metals, the Fermi level, E_F, for semiconductors is inside the band gap that separates the valence (completely filled) and conduction (empty) bands. The Fermi level can be near either the valence or the conduction depending on the doping. The characteristics of the states at E_F, and hence $\rho(r,E)$, may be different for the two cases which in turn can lead to very different STM images. In addition, at the semiconductor surface, there are additional energy levels associated with the surface that extend into the bulk band gap, known as surface states.

In the tunneling mode, for both metals and semiconductors, the relative energy levels between the tip and the sample for different sample biasing conditions are similar to that shown in Figure 2.13. For positive sample biasing (Figure 2.13.a), electrons flow from the filled states of the tip into the empty states of the surface. The situation is reversed for negative sample biasing; electrons flow from the filled surface states to the empty tip states. For low doping or high voltage situations, the bias polarity, not the doping, determines which of those states (conduction or valence) are involved in tunneling.

Because only those states between the tip and surface Fermi levels contribute to the tunnel process, changes in the bias voltage result in tunneling current changes that reflect changes in the states that are sampled. Conductance (I/V) measurements as a function of sample bias

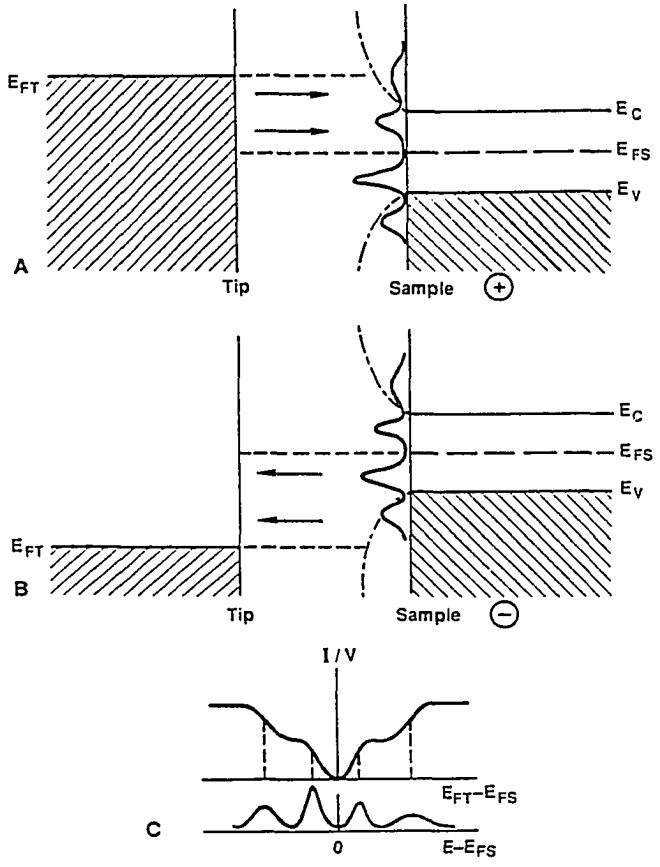

Figure 2.13. Relative energy level between tip and sample for: a) positive and b) negative bias conditions. The relation between surface state energies and conductance onsets is shown in c). E_n is the top of the valence band, E_c is the bottom of the conduction band, E is the electron energy and $E_{FT(S)}$ is the Fermi-level of the tip (sample)

voltage are sensitive to those changes and can be used to obtain information about filled and empty surface states. Figure 2.13.c shows the relation between conductance and surface state energy onsets.

The early STM work on semiconductors[14] reported appreciable voltages (~ 2.5 V) required for the onset on tunneling. This can be explained by the lack of states between the tip and surface Fermi levels, a non-Ohmic contact that developed, and/or a surface barrier due to band-bending. Later work has shown that the tunneling conditions for semiconductors are not much different than for metals resulting in the belief that the tunnel conductance can be obtained in a manner similar to that for metal images.

Figure 2.14 shows the calculated $\rho(r_o,E)$ for the GaAs(110) 1x1 reconstructed surface, based on the charge in states within 1 eV of the respective band edges. The total charge density is also shown. Far from the surface, the valence-edge charge looks very similar to the total charge density. The charge is concentrated on the As atoms, which are raised by the presence of the Ga in the reconstruction. The image is then well represented by the superposition of As atom charge densities.

The conduction-edge charge, however, looks quite different. Charge is concentrated on the Ga atoms, which sit lower on the surface than do the As atoms, resulting in a smaller corrugation than for the valence charge. In addition, the difference in the maxima between As and Ga densities results in a difference in the occupied and unoccupied states of the surface. By varying the tunnel bias voltage[73], the STM image can selectively display either the As or the Ga atom positions, as shown in

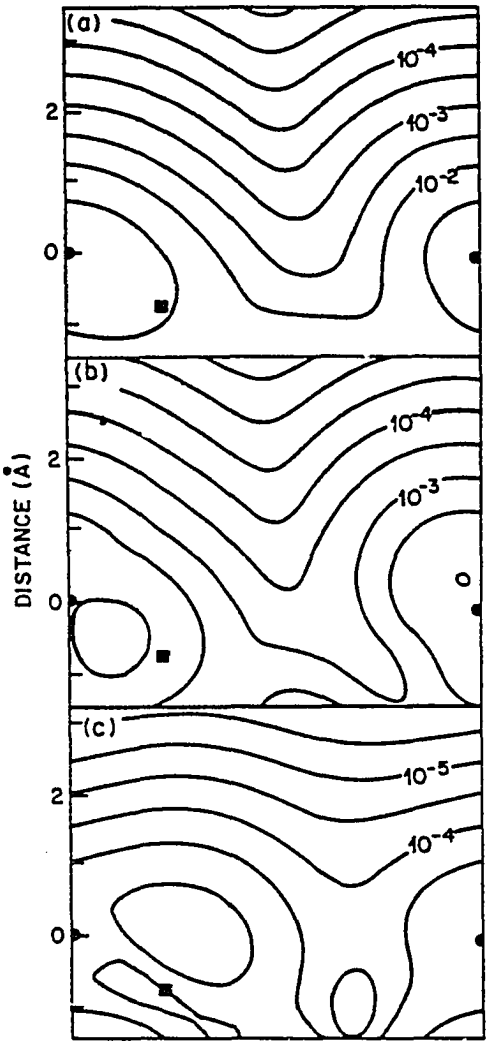

Figure 2.14. Projected charge densities of the GaAs(110) 1x1 surface. The three panels show: a) total charge, b) charge in states within 1 ev of the valence band edge, and c) charge in states within 1 ev of the conduction band edge. Positions of the atoms are given by circles (As) and squares (Ga)

Figure 2.15.

Even though many surface characteristics of semiconductors differ from metals, it is possible not only to image them, but to account for their behavior theoretically using similar methods as for metals. One area in which caution must be exercised, though, is that of dangling bonds. Initial reports from Tromp and coworkers[31-34] indicate that dangling bonds play an important role in determining the state-density contours. By using tunneling spectroscopy to map the I-V characteristics of surfaces, a better understanding of the behavior of surface states and dangling bonds on the LDOS can be obtained, and the electronic and geometric effects on the images can be isolated.

H. Conclusions

The Atomic Superposition approach used by Tersoff and Hamann yields some quantitative information, but it is only an approximation for determining the characteristics of STM images. A full, microscopic theory to interpret the images in detail is required and should include the following:

a) modifications of the bulk electronic properties in the last few atomic layers, up to and outside the surface of each electrode;

b) tunneling through the space-dependent potential barrier, including the effects of local electric fields and polarization, especially in the presence of adsorbates and surface states, and which accounts for the complete multiple image interaction and the non-planar geometry of the tunneling junction;

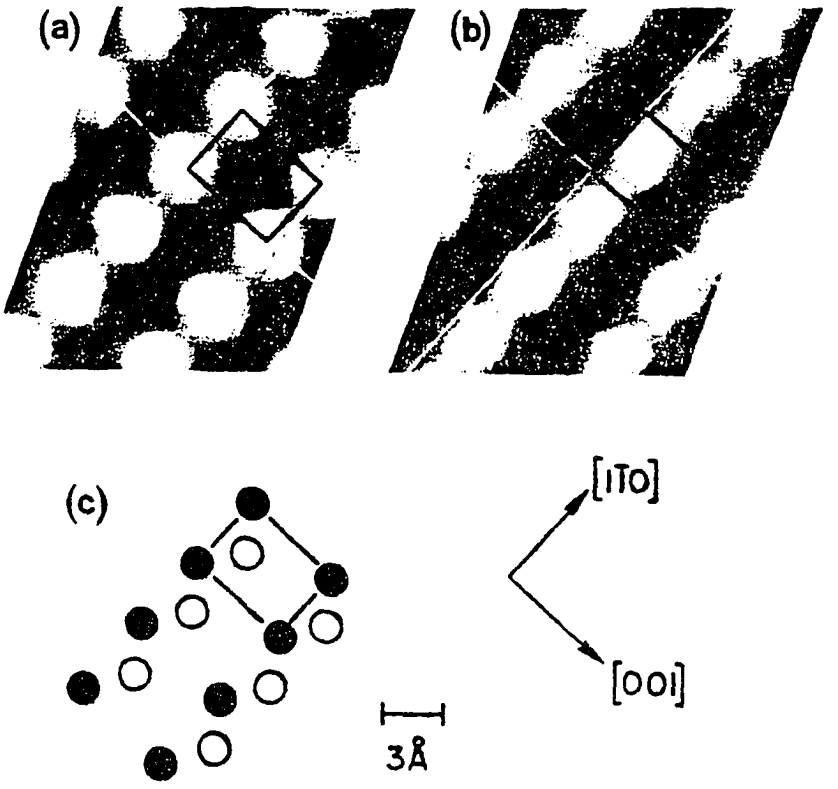

Figure 2.15. Constant current images at sample voltages of a) +1.9 V and b) -1.9 V. Grey scale surface heights range from 0 (black) to a) 0.83 Å and b) 0.65 Å (white). A top view of surface atoms is shown in c) where open circles represent As atoms and closed circles represent Ga atoms. Rectangle indicates the same unit cell

c) the effects of the microstructure of the tip;

d) inelastic and non-equilibrium phenomena;

e) identification of the actual physical quantities being probed by the STM; and

f) a definition of the resolution and an analysis of its practical limits.

Many groups[74-80] have tackled this huge task, but have yet to reveal a complete theory that satisfies all of the above features. Although the transfer Hamiltonian formalism developed by Tersoff and Hamann is incomplete because of underlying assumptions of a thick barrier and low bias voltages, it is still the best theory available today in explaining the current STM and STS (Scanning Tunnel Spectroscopy) images. It is the hope that future experimental work in barrier height measurements and tunneling spectroscopy, along with improved computational techniques, will provide the means to more fully develop Scanning Tunnel Microscopy theory.

III. EQUIPMENT

A. Scanning Tunnel Microscope

The Scanning Tunneling Microscope (STM) used in this work was developed by Robert McAllister of McAllister Technical Services (MTS) and Adam Kollin of RHK Technology, with the cooperation of Dr. Miguel Salmeron and the University of California, Berkeley. MTS builds the microscope head, while RHK is responsible for the electronic controls.

1. Microscope Head

The MTS/RHK STM was one of the first commercially available STM's and was designed for use in air or under UHV (ultra high vacuum) conditions. The microscope head, as shown in Figure 3.1, is built onto an eight inch Conflat flange and, excluding the suspension system and piezoelectric transducers (PETs), all the materials are UHV compatible. (The viton in the suspension system and the ceramic PETs tend to outgas for a long time resulting in an order of magnitude reduction in the base pressure of the system.)

The sample is held onto a one-inch square aluminum sample holder by copper clips or Aquadag. The holder slides into a U-shaped fork that is mounted on an aluminum deflection bar and is electrically isolated from the bar by ceramic washers. By applying a slight pressure away from the tip, the holder is clamped into position. The deflection bar fits onto the ends of two micrometer screws which control the movement of the sample toward the tip in a coarse (roughly 300 microns per turn) and in a

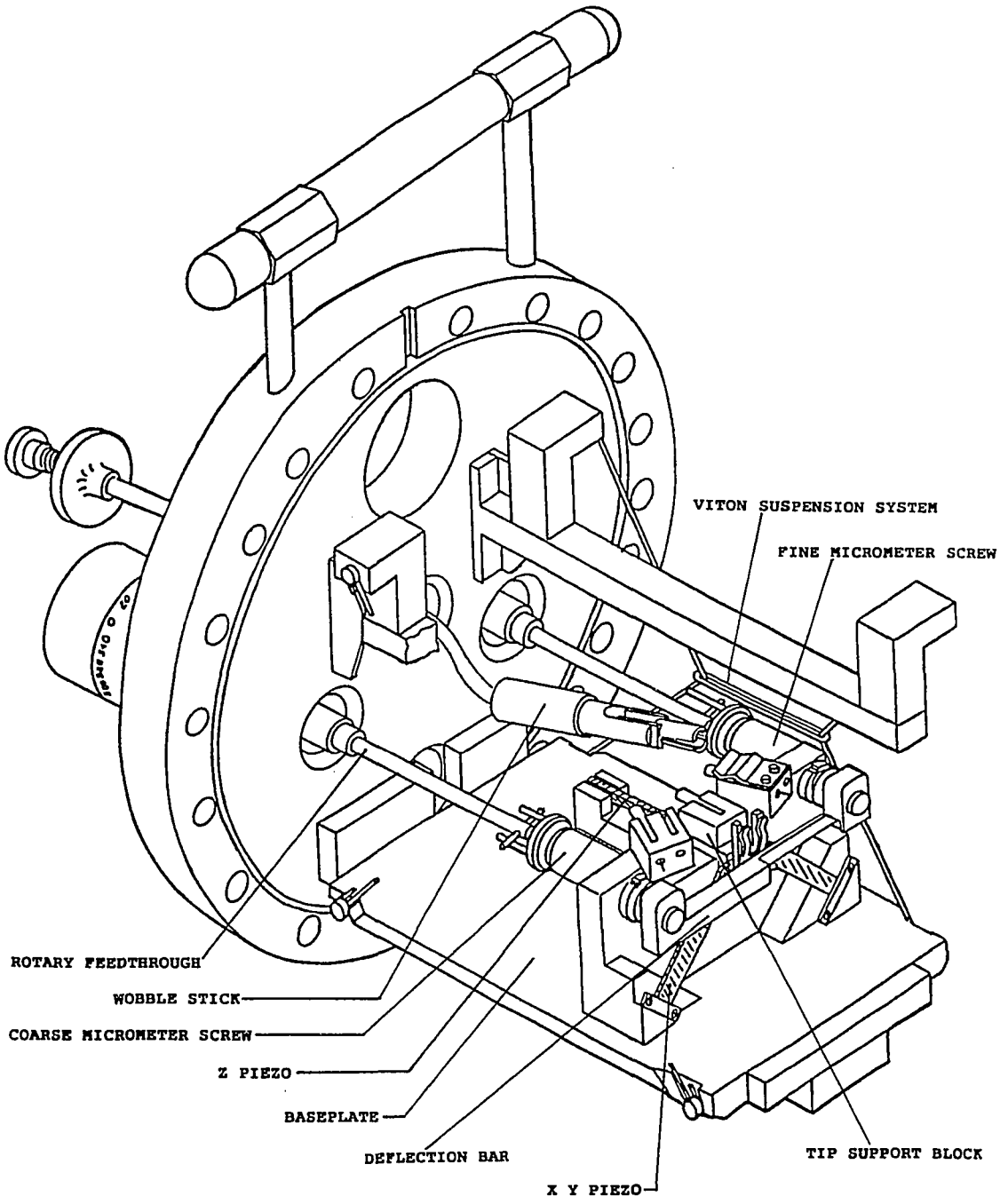

Figure 3.1. Cut-away view of the McAllister Technical Services Scanning Tunnel Microscope head

fine (roughly 3 microns per turn) manner. The end of the bar closest to the fine micrometer screw is much thinner than the rest of the bar in order to demultiply its motion. Both micrometer screws are operated from the atmosphere side of the flange by rotary feedthroughs that can be decoupled from the micrometers after use.

The tip is held in an aluminum block that is attached to, and yet is electrically isolated from, the junction of the PETs. The PETs are machined from piezoelectric ceramics, typically Channel 5500, Navy II, into two pieces that form the traditional tripod piezoscanner.[26] Figure 3.2 shows the specifications for the two piezoelectric pieces that form the MTS orthogonal scanner. One piece is the Z-piezo (Fig. 3.2.b) with sensitivity of approximately 1.3 nm per volt and the other is the X,Y plate (each direction with the sensitivity of roughly 1.5 nm per volt). The shaded areas are grounded and are separated from the high/low voltage regions by scratching a line in the metallized coating. The two pieces slide into an aluminum frame and are held in place by TorrSeal (a UHV compatible binder which also helps to minimize some vibrations as well as electrically isolating the ceramics).

The tip/sample arrangement is attached to a baseplate that is clamped during the tip and/or sample loading by a linear feedthrough and free to hang otherwise. The baseplate hangs from a stacked plate arrangement that alternates aluminum bars with viton spacers to provide some vibration isolation. The main source of vibration isolation at this stage, though, is from the viton "strings" that hang from a stacked bar arrangement near the top of the flange and form an "X" arrangement on

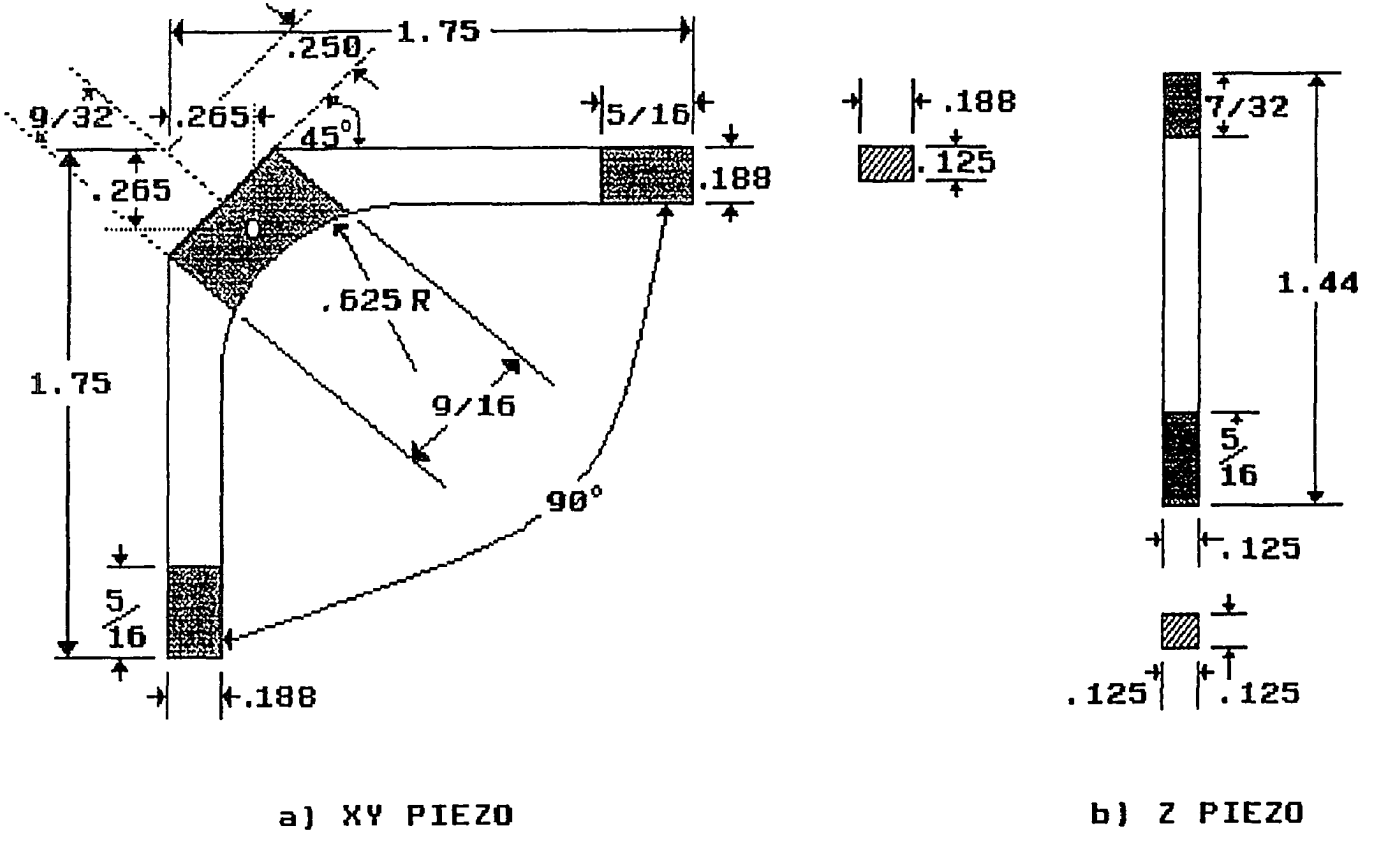

Figure 3.2. Design parameters for the piezoelectric transducers

either side of the baseplate (refer to Figure 3.1). Despite the simplicity of the arrangement, the resonant frequency of the STM is greater than approximately 2 kHz.

The system can hold up to four tips at one time (two on either side of the PETS) to allow UHV study without having to break vacuum as often for an exchange of tips. A wobble stick with a flexible bellows is used to interchange the tips. A mirror above the tip/sample assembly allows a Nikon SMZ-2B stereoscopic microscope to be used during the coarse adjustment by viewing the tip and its mirror image in the sample through a 1.50 inch viewport located above the wobble stick. A fiber optic cable is used for illuminating the tip/sample area from a Nikon MKII fiber optic light source.

A platinum alloy ($Pt_{.87}Rh_{.13}$) is used instead of tungsten as tip material to minimize the effects of oxides and other contaminants on the probe tip. The tips are mechanically cut from 20 mil wire (0.02") with wire cutters at an angle on the order of 45 to 60°. This technique yields tips that are fairly blunt on the visual scale but contain the necessary mini-tips for good images (refer to Figure 1.3). More than 80% of the cut tips have resolutions that are in the nanometer range or better. In-situ "sharpening" can, in some instances, improve the quality of the tip. This can be accomplished by gently touching the tip to the surface or by applying a high electric field (on the order of 10^8 V/cm) across the electrodes for a few minutes.

2. Electronic Control

The STM is electronically controlled by the STM 100 electronics package from RHK Technologies. The STM 100 can be divided into three sections: the preamplifier, the feedback loop and the X-Y scanning.

The preamplifier is housed in a small box that is mounted near the microscope head. It is attached to the microscope flange by a short cable to reduce the effects of stray signals. It is located outside of the the flange to avoid problems during the bakeout of the vacuum chamber. A 15 foot cable connects the preamp to the electronic control box. The zero offset and gain of the I/V converter in the preamp can be adjusted by using a small screwdriver.

The feedback loop circuit is schematically shown in Figure 3.3. The signal from the preamp is compared to the Current set value which is set using a ten turn pot on the front panel and can range from 0 to 10 nA. An invertor before this comparator stage ensures that the signals to be compared are of the appropriate sign. The sign of the tunneling current can be adjusted by switching the polarity of the bias voltage, which can range from 0 to 10 volts. Another ten turn pot on the front panel sets the gain from 0 to 10, with the higher gain resulting in a faster response time of the loop. If there is too much noise in the signal though, the higher gain may lead to oscillations in the feedback loop.

After the comparator, the difference or error signal is sent to the integrator stage. The time constant can vary from 1 to 20 msec, as determined by the integrator pot. The total response of the feedback loop then depends on both the gain and the integrator settings. It is

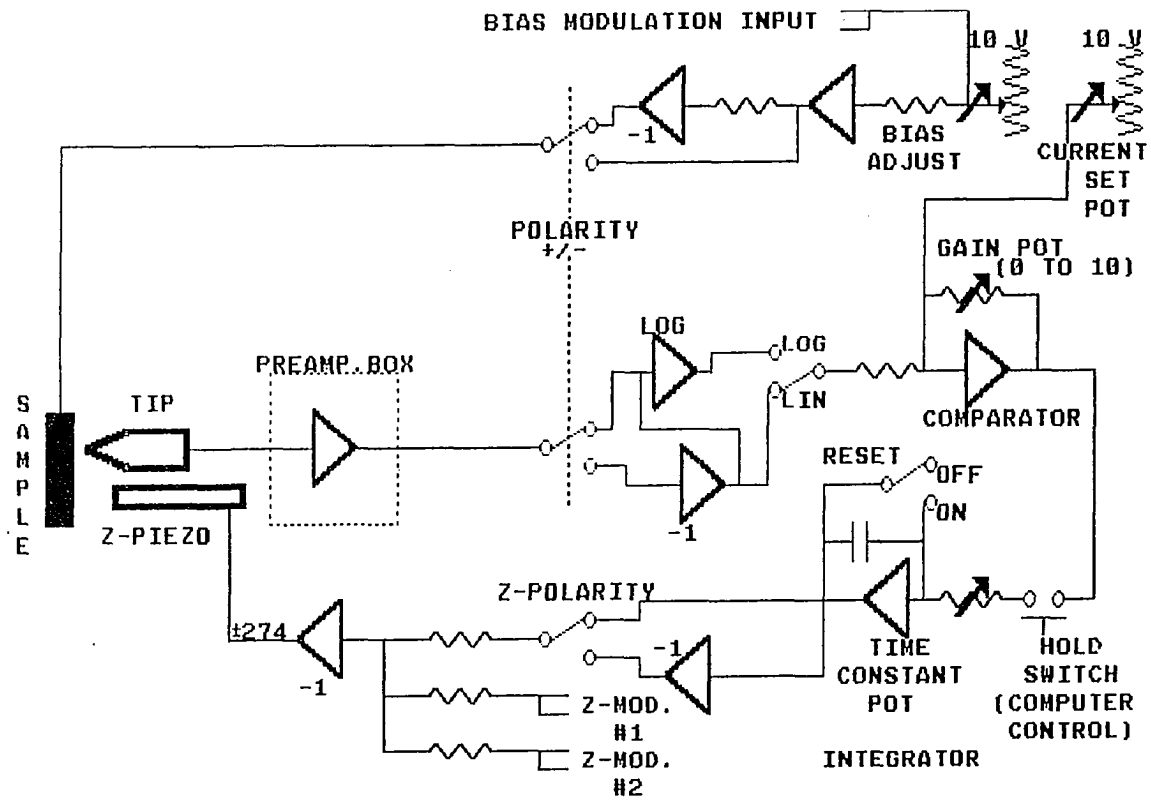

Figure 3.3. Schematic of the STM 100 feedback loop

convenient to start with a low gain and a high time constant and then vary one or both until the stability limit of the loop is reached (the system will oscillate). The optimum response for the system will then have the time constant set slightly higher than its unstable value.

The output of the integrator is sent to a high voltage op-amp for amplification. This feedback voltage output controls the length of the z-piezo on the low voltage side. The total voltage range is roughly +/- 137 volts corresponding to a length range of approximately 3,500 Å. Larger extensions can be obtained by application of higher voltages on the high voltage side of the piezo. This bias voltage can be set by the coarse and fine pots on the front panel with a variation of 0 to 2,000 volts (~ 2.6 microns). Because of possible depolarization of the piezo, the practical range is half the above range.

The X-Y scan size is determined by the settings of the X and Y amplitude pots, which range from 0 to 270 volts. One problem with operating at the larger scan sizes is the non-orthogonality of the piezos with respect to the surface at the larger voltages. As the X and Y scan voltages increase, the piezos flex instead of moving in orthogonal directions. This introduces an artificial slope to the images that is directly proportional to the scan size. (A slope correction is available in the STiMage 1.3 software package as described in the following section.) For scan sizes much larger than 0.1 microns, some information can actually be lost due to the sloping and the inability of the z piezo to compensate for the large tip displacememts. (Scan heads capable of covering larger areas are now on the market.)

The X scanning is made in 4,096 steps/line. The number of lines per frame (image) is determined by a three position switch on the front panel (64, 128 or 256 lines/frame). The scan speed is determined by a multiposition switch, "ms/line" in combination with the multiplier switch above it and the X amplitude. The image frame can be moved over the surface by varying the offset (bias) voltage on the high side of the X and Y piezos. The voltages can range from 0 to 2,000 volts, but as explained above, the practical range is 0 to 1,000 volts.

Scanning can be controlled in two ways: the "local" mode and the computer mode. In the local mode, the X-Y scans are controlled by the start, stop and reset switches on the front panel. While scanning, a red indicator light will be on. The data can be viewed using a chart recorder or a storage oscilloscope (with the former being too slow for most applications). The X voltage ramp (0 to 10 volts) drives the X axis of the oscilloscope (or X-Y recorder) and is available from the BNC connector on the back panel. The X+Z output drives the Y axis. To avoid an overlap of image lines, a constant voltage is added to the Z output voltage after each X line scan. This constant voltage can be varied by the Y Chart Amplitude pot on the front panel and is proportional to the Y voltage. Therefore, the Y axis of the image is in reality a Y+Z axis. This process is equivalent to a change in perspective angle or inclination of the image.

In the computer mode, the X-Y scans and the resulting display are controlled by the STiMage software package to be described in the next section.

B. Computer Hardware and Software

The STiMage 1.3 program is an integrated software package developed by Dr. Frank Ogletree at the University of California, Berkeley in cooperation with McAllister Technical Services and RHK Technology. The program controls the data acquisition, storage, display and processing of STM images. The software is run on a Compaq 286 Deskpro computer with a 40 Mb hard drive and a 1.2 Mb floppy drive. A Data Translation DT-2821-F (130 kHz) High-Speed Analog and Digital I/O System board is required for STM data acquisition. A 80287 math co-processor is installed to improve the performance of STiMage (screen drawing and image processing take three to seven times longer without it). An EGA graphics adaptor is the minimum required to properly display the STM images, however, the above system has a VGA graphics adaptor. The images are displayed on a NEC Multisync II monitor or printed by a Tektronix 4696 ink jet color printer.

The STiMage program is a menu driven program controlled primarily by the function keys (F1 - F10) and the escape (ESC) key, with additional numbered options and commands entered through the keyboard. The main menu is divided into four major areas, as shown in Figure 3.4. The left area is a listing of the main menu options and their corresponding function key. The center section is for listing sub-menu options. The right side of the screen lists information on the currently active STM image (in display, storage and processing modes as chosen by F2, F3 and F4, respectively) or on the current status of the STM electronics (in the data acquisition mode, entered by F1). The bottom half of the main menu

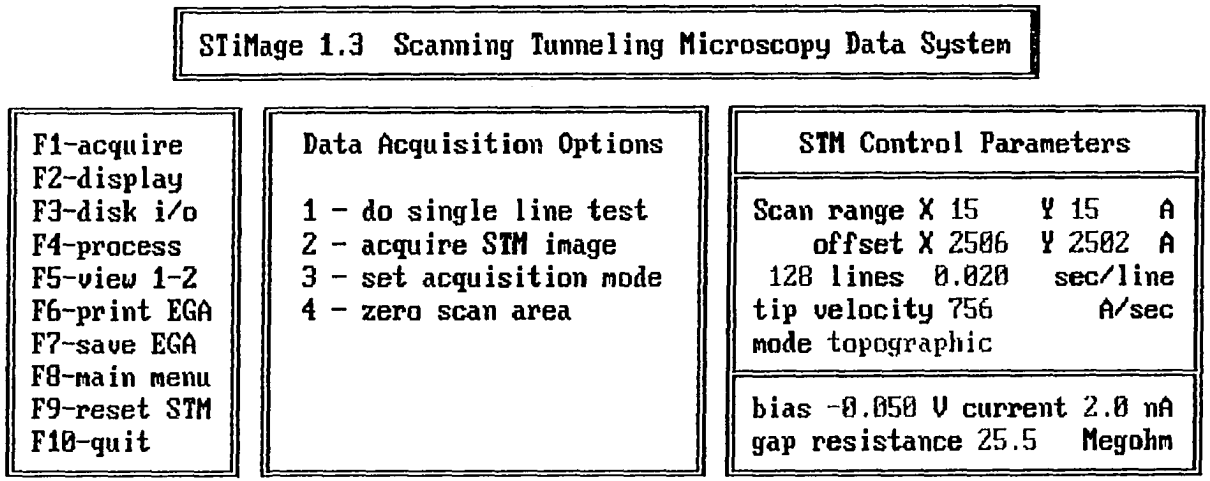

Figure 3.4. Menu screen of the STiMage 1.3 program

screen is used to input or display text information on the operation of the STiMage program. Figure 3.5 lists all of the menu options and their corresponding sub-menu choices.

StiMage allows data to be acquired in one of three main modes: the topographic or constant current mode, the current or constant height mode, and the auxiliary or spectroscopic mode. The program can acquire either full two-dimensional STM images or quick single-line scans for testing parameters.

The parameters for data acquisition are all controlled by the RHK STM 100, as described above in Section 3.A.2. These parameters can be read out by the STiMage program through the DT2821 interface board except for the feedback controls (gain, integrator time constant, and the lin/log mode). When the data acquisition sub-menu (F1) is selected and the electronics set to the computer-control mode, the parameter values are displayed in the STM Control Parameter portion of the computer screen. Figure 3.4 shows the numerical values for a graphite sample in a lighter shade as compared to the text shade. As the control settings are altered, the displayed values change.

The data acquisition sub-menu has four options. Option 1 collects data for a single line scan. In this mode, complete traces (one line going from left to right, the other from right to left) of both the current and the Z-piezo (or other contrast variable) signals are acquired simultaneously. The traces can be used to check things such as the stability of the feedback loop, the tip condition, and the reproducibility of the images.

STiMage 1.3 MENU AND SUB-MENU OPTIONS

F1 - acquire
Data Acquisition Options
1 - do single line scan
2 - acquire STM image
3 - set acquisition mode
4 - zero scan area

F2 - display
Image Display Options
1 - 2D image plot
2 - 2D even/odd switch
3 - 3D image plot
4 - cursor/cross section
5 - control side plot
6 - set color mapping
7 - choose colors

F3 - disk i/o
File I/O Options
1 - retrieve image file
2 - store image file
3 - edit file parameters
4 - store file parameters
5 - set printer mode
6 - recall EGA screen

F4 - process
Image Processing Options
1 - slope correction
2 - smooth image data
3 - median filter image
4 - zoom in on image
5 - check buffer memory
6 - image data histogram

F5 - view 1-2

F6 - print EGA

F7 - save EGA

F8 - main menu

F9 - reset STM

F10 - quit

Figure 3.5. STiMage 1.3 menu options and corresponding sub-menu choices

Option 2 acquires a normal 2-D STM image associated with the settings of the STM electronic controls. If the X,Y offset and amplitude pots on the STM 100 are changed, a white-outlined box on the old image shows the location of the next image relative to the top view display. This box cursor can be viewed by keying F5 which changes the screen from one graphics page to another allowing quick comparison of the cursor position and the control settings.

Option 3 selects one of the three contrast modes: topographic, current and auxiliary. In the auxiliary mode, an image is created from any signal with a -10 to +10 volt range. Possible applications include spectroscopic mechanisms, such as barrier height and density-of-states imaging. Contrast in spectroscopic modes may be measured using an external lock-in amplifier and bias or Z-piezo modulation, and connecting the lock-in output to the auxiliary-signal a/d channel.

Option 4 is used to calibrate the STM scan area for areas 50 Å or less to minimize the effect of the A/D offset error. When the X and Y scan amplitudes are set to zero, the zero offsets are recorded and the size of small-area images will be correct. This calibration is lost on program exit or reset.

The STiMage program displays the STM images on a two-dimensional computer screen using three possible views: the "top view," the "side view" and the "3-D view." The top and side views are displayed together on the 2-D screen options, while the 3-D view has its own 3-D screen.

In the top view, the image area displayed is seen as a square view from above with the color of each pixel representing the "contrast,"

either the height in the topographic images or the local tunneling current in the current images. The top view is shown at the left of the 2-D screen. A color bar at the extreme left shows the different colors used with yellow representing a peak value. The colors span a linear range over the image contrast. The screen text below gives the number of angstroms or nanoamps per color step.

In the side view shown on the right of the computer screen, the contrast variation along individual horizontal scans is displayed as a function of X (horizontal) position. Scans recorded at different Y positions are displaced by an arbitrary amount in the vertical direction so they can be distinguished. The left-going and right-going STM scans are usually different, so the three display modes show only even (left) or odd (right) lines. The scan direction is indicated by an arrow at the lower left of the image. Above the arrow, the scale in the Z (contrast) direction is given

The 3-D view utilizes individual scan lines to generate a hidden line two-dimensional projection of a three dimensional plot. The color of the lines change as the Z (contrast) coordinate changes. The polar (θ) and azimuthal (ϕ) angles of the point of view may be adjusted, as well as the Z magnification and the number of lines drawn. The main drawback of the 3-D view is the relatively slow plotting speed compared to the other views.

At any time, the STM screen can be saved using F7 - save EGA. This creates a file in the PCX format which then can be edited or modified by a "paint" program. Publisher's Paintbrush by Z-Soft is the paint program

used to prepare the STM images for printing. The STiMage program (using the F6, print EGA option) directly supports only a few printers at this time so Paintbrush (which supports a variety of printers, including color printers like the Tektronix 4696) is essential for creating a hard copy of the images. Future updates of STiMage will provide direct printing of the screen without the use of intermediary software.

C. Support Equipment

The STM mounts into a vacuum chamber that has a load lock for cleaning and loading purposes. Two Huntington rotary-linear motion magnetically coupled feedthroughs are used for transferring the sample holder from the load lock to the deflection bar. A Balzer 50 l/sec turbo pump is connected to the load lock to provide ~ 10^{-7} torr in the load lock area and to rough out the entire chamber when necessary. An Ultek 200 l/sec ion pump is mounted on the main chamber. Typical operating pressures are of order 2 x 10^{-9} torr after bakeout. Figure 3.6 is a block diagram of the vacuum chamber showing some of the items described above and below.

A PHI model 20-005 ion gun and a dc heater are installed on the load lock for cleaning purposes. The ion gun can be replaced by a dc sputtering arrangement.

The vacuum chamber is braced on a Newport quarter-ton, steel vibration isolation table donated by IBM, Rochester. The table is capable of being floated by four cannisters of air, but the inertia of the table (plus chamber, ion pump and peripherals) is sufficient to damp

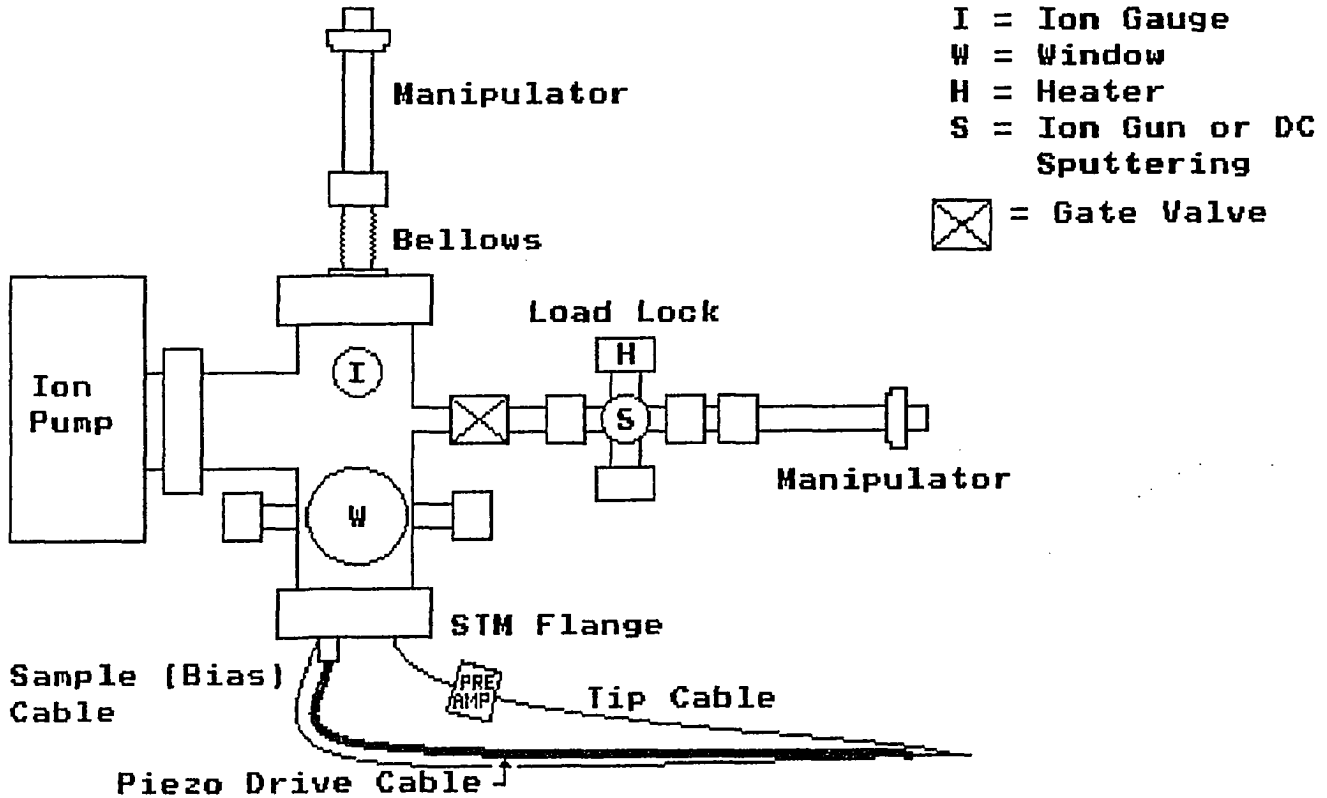

Figure 3.6. Block diagram of the vacuum system including components for loading and manipulating the sample

out building vibrations, so that to date, the cannisters are used merely for support. Also on the table is a station for doing studies in air, in which a glass bell jar (or facsimile) is required to reduce acoustic vibrations.

To do barrier height measurements, an Exact function generator (type 301) and a PAR JB-5 lock-in amplifier are connected to the STM 100. The signal from the function generator is first passed to a voltage divider in order to reduce the voltage to the range 0 to 1 volt peak-to-peak. All signals are monitored using a Kikusui COS5020-ST storage oscilloscope. The storage scope is very useful for tracking down noise sources as well as providing a quick determination of tip qualilty. (Poor tips, and sometimes poor samples, result in a noise pattern that contains voltage spikes on the order of 1 V or more that do not diminish with time.) The storage scope can also provide STM grey scale images as well as line scans as an alternative to the computer generated images.

D. Comments

Although the described MTS/RHK system uses the tripod scanning arrangement, there are many other orthogonal piezoelectric scanners available.[81-86] The most versatile scanner is the tube scanner first used by Binnig and Smith.[81] The tube scanner is machined from a single, cylindrical piece of piezoelectric ceramic and, as a result, is inherently more stable than the tripod arrangement. The tube scan head is more compact and rigid resulting in higher mechanical eigenfrequencies which allow for higher scan rates and real-time imaging. The scan heads

can be machined into a variety of sizes providing some flexibility in the maximum scan size.

There are three major disadvantages to the MTS/RHK tripod arrangement: fixed orientation of the scan head, sample loading, and limited scan size. Because of the orientation of the microscope head on the flange, sample imaging can only be done with the flange vertical. This limits the imaging to that done in air or in vacuum only. (Imaging in liquids or at low temperatures is not possible in this configuration.)

In addition, the location of the tripod with respect to the suspension system limits sample loading. From Figure 3.1, it can be seen that the only way a sample can be loaded is along the z-direction, from the end of the baseplate heading into the tip. This configuration presents a loading challenge under UHV conditions, and also limits the types of surface studies that can be performed due to sample transfer considerations. Last, in order for the tripod arrangement to have resonant frequencies on the order of 2 kHz (or better), the Z and X,Y pieces are made smaller. This in turn limits the maximum scan size, as described above.

Despite the disadvantages of the MTS/RHK system, atomic resolution is still possible with the system. In addition, the variety of available imaging techniques compensates, to some degree, for the present limitations.

IV. RESULTS AND DISCUSSIONS

Images were obtained for three different classes of materials: a metal (gold), a semimetal (graphite), and a semiconductor (germanium). The various tunneling conditions for the images of gold and graphite presented in this paper, are listed in Table 4.1, while those for germanium are listed in Section IV.C. Each investigation provided information about the electronic and geometric behavior of surfaces, the utility of the Scanning Tunnel Microscope in surface analysis, or both.

A. Gold on Glass

As a preliminary study of the STM system, an evaporated gold film, deposited onto glass, was examined in air. When viewed under an optical microscope, the film contained scratches and rough regions, as well as areas that appeared smooth. To examine the quality of the film under a resolution which is better than the optical microscope, smooth regions were chosen for the STM images.

Images were taken under a variety of tunneling conditions, with the majority of the images showing features similar to those shown in Figure 4.1. Despite the visual smoothness of the film, the tunneling images were filled with holes of varying sizes, typically of order 100 nm, as shown in the closeup view in Figure 4.2. The edges of the holes were fairly sharp indicating that the features were due to the formation of the film as opposed to underlying surface features on the glass slide, or tip quality. The film was approximately one micron

Table 4.1. Tunneling conditions and data processing steps for annealed pyrolytic graphite (APG) and gold samples

File	Sample	V_B (mV)	I (nA)	R_g (MΩ)	ΔP[a] (Å)	F4[b] Opt. #'s	Figure Number
PG 33a[c]	APG	-50	2.0	25.4	2.67	2,3,4	4.5
VPG 14	APG	-50	1.9	26.6	2.84	2,3,4	4.11
VPG 27	APG	-75	1.0	73.5	2.70	2,4,3	4.6,4.7
VPG 29	APG	-75	2.0	37.1	2.64	2,3,4	4.10
VPG 36a	APG	-60	1.5	39.7	2.53	4,2,3	4.20
VPG 39	APG	-55	1.5	36.4	2.65	2,3,4	4.12
VPG 44	APG	-50	2.5	19.9	2.60	2,4,3	4.16
VPG 58a	APG	-34	1.0	33.7	2.56	2,4,3	4.13
VPG 77	APG	-10	2.0	5.0	——	2,4,3	4.17
VPG 86d	APG	-40	2.0	19.7	2.63	2,3,4	4.19
82903[d]	APG	-50	2.5	19.6	2.61	2,3,4	4.18
61501	APG	-50	2.0	25.5	2.30	2,3,4	4.14
61502	APG	-50	2.0	25.0	2.34	2,3,4	4.9
61511	APG	-50	2.0	25.4	2.34	2,3,4	4.15
AU 11[c]	AU	+1500	2.2	597.0	——	1,2,3,4	4.2,4.3
AU 13[c]	AU	+1500	3.0	454.0	——	1,2,3,4	4.1

[a] ΔP = average peak-to-peak distance in graphite images.

[b] F4 Processing features: 1 = slope correction; 2 = smoothing; 3 = median filter; 4 = zoom.

[c] PG and AU samples were examined in air; the other materials were all examined in UHV.

[d] 829 sample was the same as for VPG, but with a different tip used to image.

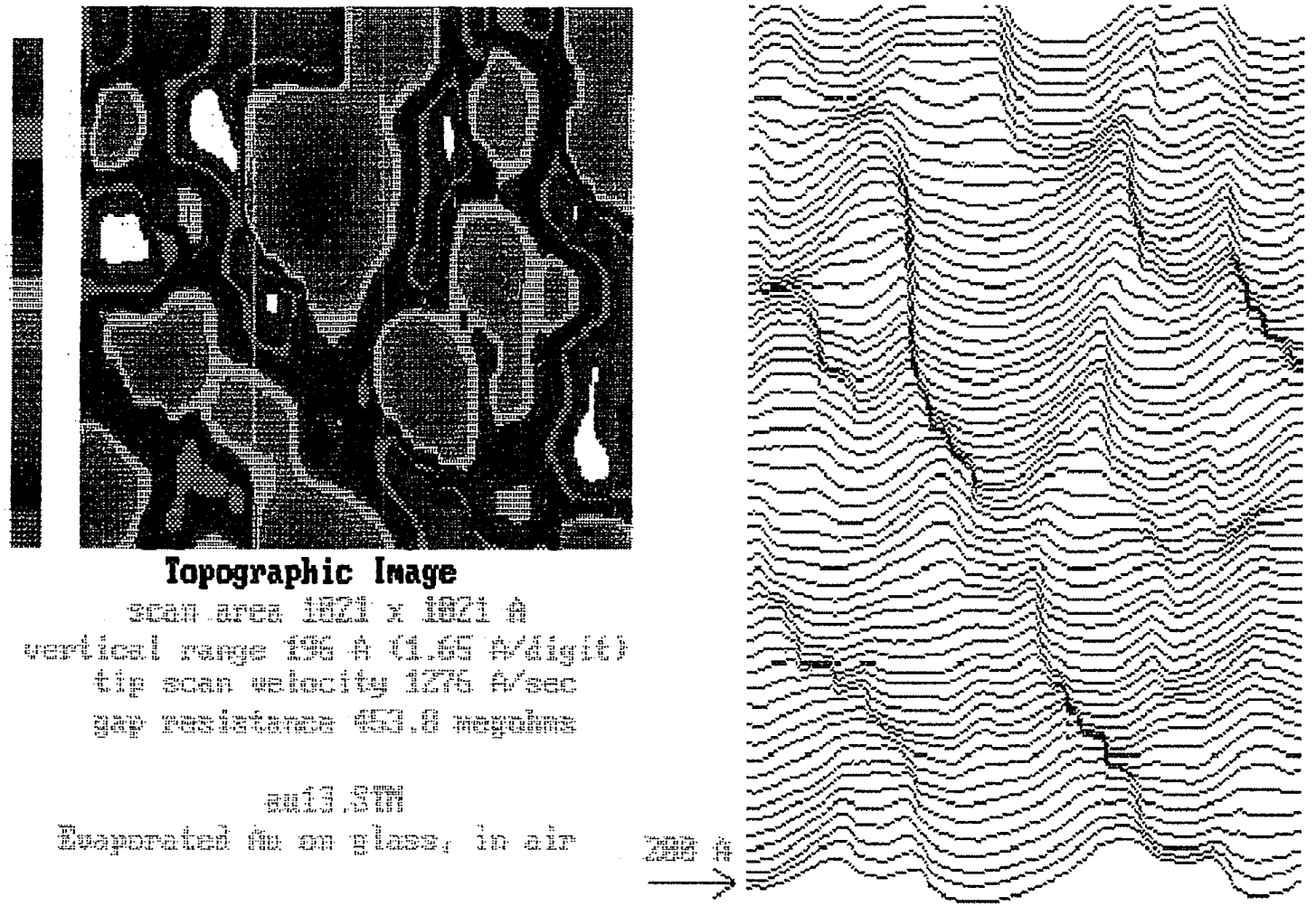

Figure 4.1. Large area scan of evaporated gold on glass

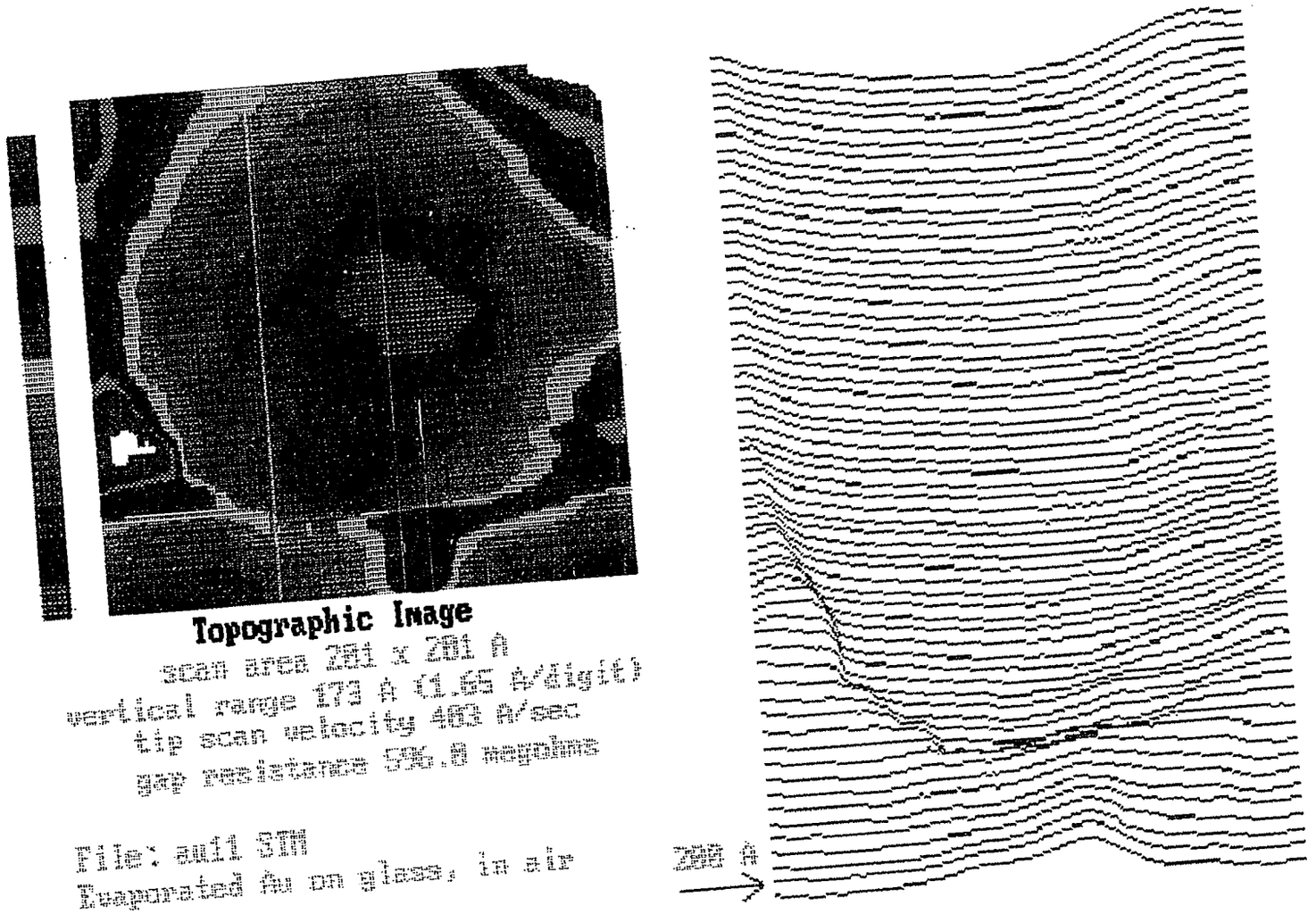

Figure 4.2. Close-up scan of evaporated gold on glass

thick, which was sufficiently thick to smooth over any defects on the glass; sharp features on the glass look rounded after many layers of gold have been deposited.

Poor tips are not capable of resolving sharp surface features because of the increased contribution of multiple tips to the tunnel current (refer to Figure 1.3). As the tip scans over the surface, the mini-tip closest to a surface feature is the primary contributor to the current. When the feature changes abruptly, mini-tips, other than the tip apex, are now closer to the surface feature. These mini-tips then contribute more to the current than the tip apex, and sharp features appear smooth.

The line scans on the right hand side of the figures represent the actual data, while the left hand side is an overhead view of the line scans with yellow as high (blue as low) points. The vertical range is listed in line two under the image description. As mentioned in Section III.B., the data are separated into the two scan directions. By comparing the two scans, tip asymmetry, especially any contribution to the current from multiple tips, can be examined. Figure 4.3 shows the corresponding left (-x direction) scan for Figure 4.2. By overlaying the two images, similar features can be compared resulting, in this instance, in a shift of roughly 10 Å. This shift is probably due to a double tip with roughly a 10 Å spacing, but it is also due, in part, to some hysteresis of the piezoelectric transducers (PETs).

The films, which had been deposited for use as optical mirrors, were smooth optically, but the higher resolution of the STM demonstrated that,

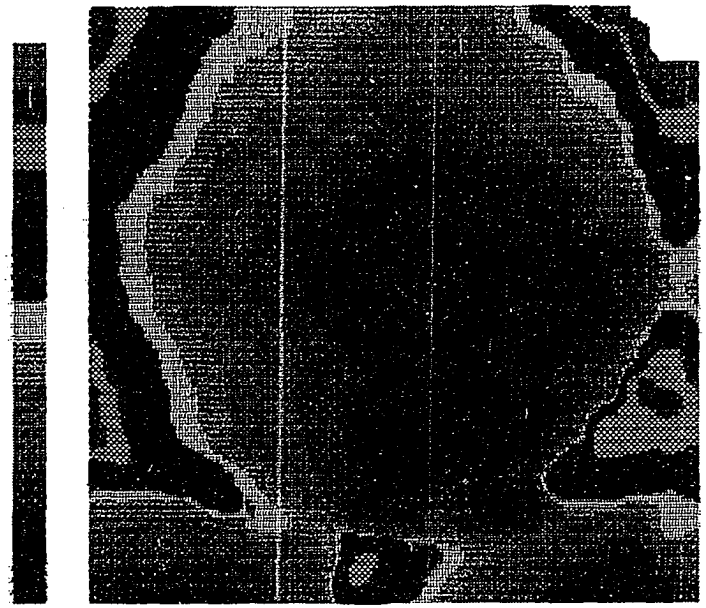

Topographic Image

scan area 201 x 201 Å
vertical range 173 Å (1.65 Å/digit)
tip scan velocity 403 Å/sec
gap resistance 596.0 megohms
File : testau11.STM
Evaporated Au on glass, in air;
Left (-x) scan of AU11

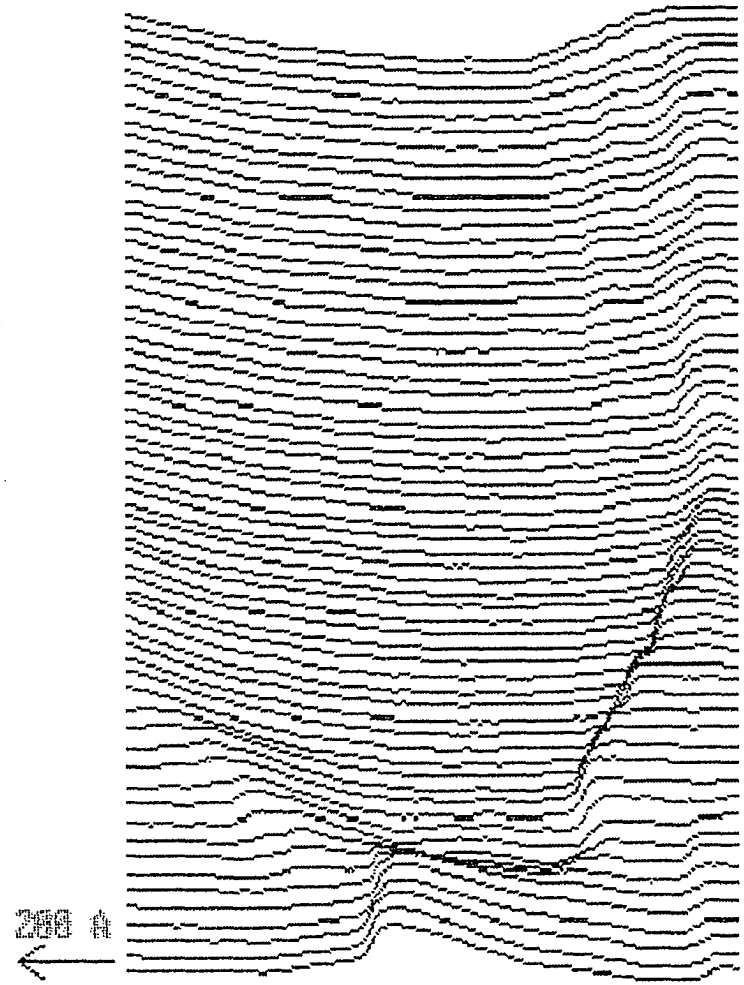

Figure 4.3. Left (-x) direction scan of Figure 4.2. Note the similarity of features and their locations

on the atomic scale, the films were very rough and uneven. This provided a valuable first test of the STM system as the films were easy to image, and the results were consistent with what has been reported elsewhere.[52,87-90]

B. Graphite

The next material examined with the STM was annealed pyrolytic graphite (APG), obtained from Dr. Doug Robinson at the Microelectronics Research Center of Iowa State University. APG (and its relative, HOPG, highly oriented pyrolytic graphite) is a layered compound with the interaction between the layers over an order of magnitude less than the interaction within the layer.[91,92] Because of the low gas absorption coefficient of graphite, the surface is inert and can be examined in vacuum[93], in air[94] or in liquids.[56] Graphite can be cleaned by cleaving, and yet is relatively impervious to contamination. This results in STM images that are relatively easy to obtain. In addition, extensive total-energy and local charge-density calculations[95,96] for the graphite surface close to the Fermi Level, E_F, are available for comparison with the STM images.

The surface atoms of APG form a hexagonal lattice with interatomic spacing of 1.42 Å, as seen in Figure 4.4. Each carbon atom has four valence electrons, three of which form sp^2 hybrids oriented toward the three nearest-neighbors. The fourth electron goes into a p-orbital oriented perpendicular to the surface (a p_z orbital). The electronic wave functions contributing to the tunnel current (for low bias voltage)

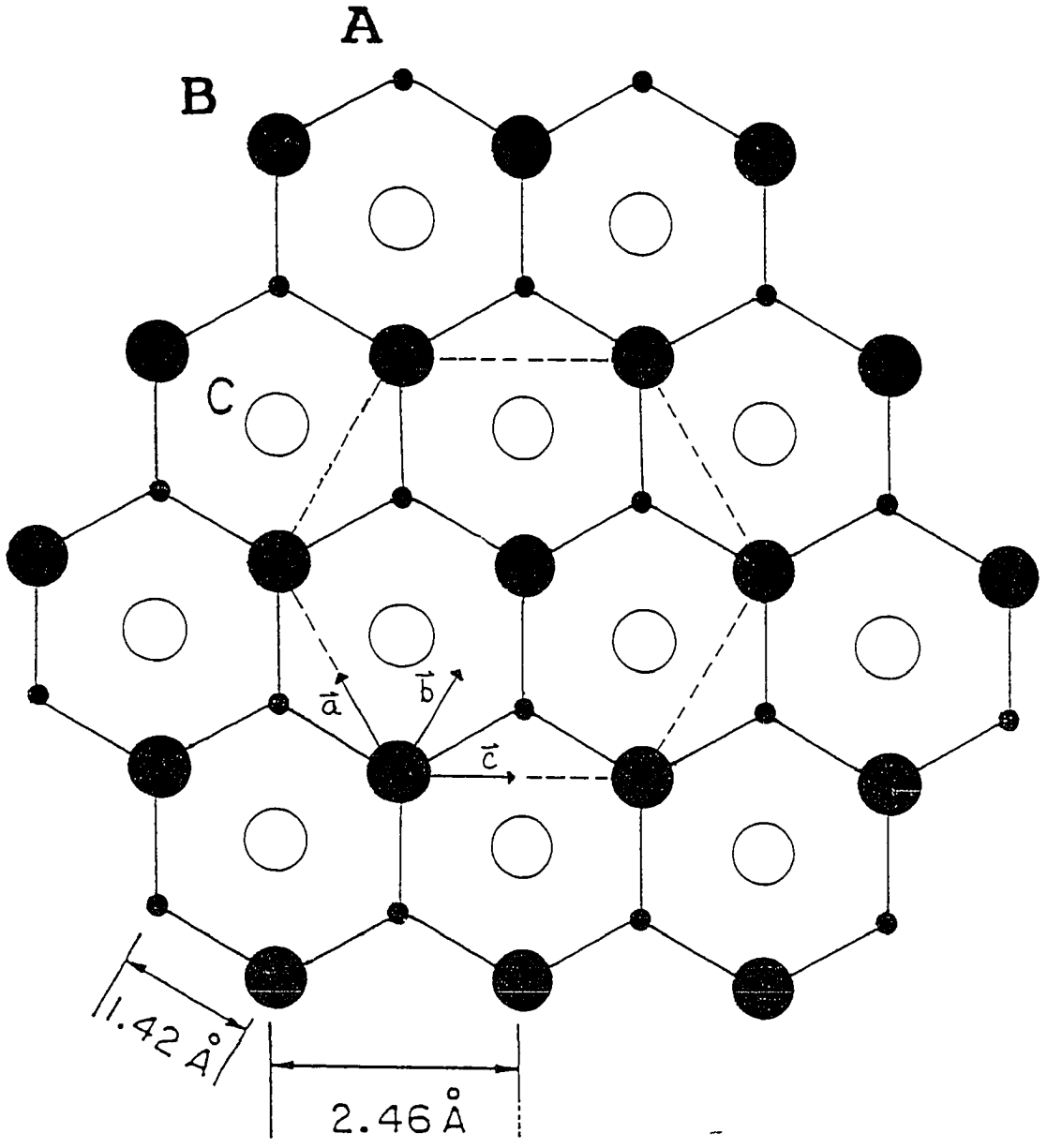

Figure 4.4. Structure of graphite with alternate layers displaced. Large (small) filled circles represent A (B) atoms in the upper layer with an (no) atom in the second layer below. Open circles represent no atom in the upper layer, but atoms (C) in the second layer. Solid (dashed) lines represent the graphite (STM image) unit cell. **a**, **b**, and **c** represent reference vectors for the STM image unit cell

originate mainly from the p_z orbitals and have large amplitudes only around the carbon site.

The graphite planes, separated by 3.35 Å, are bonded to each other through a Van der Waals attraction. This interaction gives rise to a band overlap near the Fermi level, yielding the semimetallic properties of graphite. The interlayer interaction also breaks the six-fold symmetry of the top layer thus creating two sets of inequivalent atoms.[97,98] One half of the atoms have carbon atoms directly beneath them (A atoms), while the other half do not (B atoms), as depicted in Figure 4.4. Also shown in the figure are those atoms that exist in the second layer (C atoms), but do not have surface atoms directly above them. This inequivalence of the carbon sites results in a difference in the local density of states (LDOS) such that only the B atoms are imaged.[99,100] The resulting unit cell for an STM image is also depicted in Figure 4.4 by the dashed lines, with peak spacing given by 2.46 Å. Because the peak positions are well known, graphite is often used to calibrate STM systems.

1. STM Calibration

Figures 4.5 and 4.6 show images of APG obtained in air and in UHV (base pressure ~ 2×10^{-8} torr), respectively. Tunneling conditions, for the graphite images presented in this thesis, are listed in Table 4.1. Most of the listed images were obtained under UHV conditions because they were more stable than those obtained in air. In air, acoustic noise adversely effects the tunneling current by introducing vibrations into

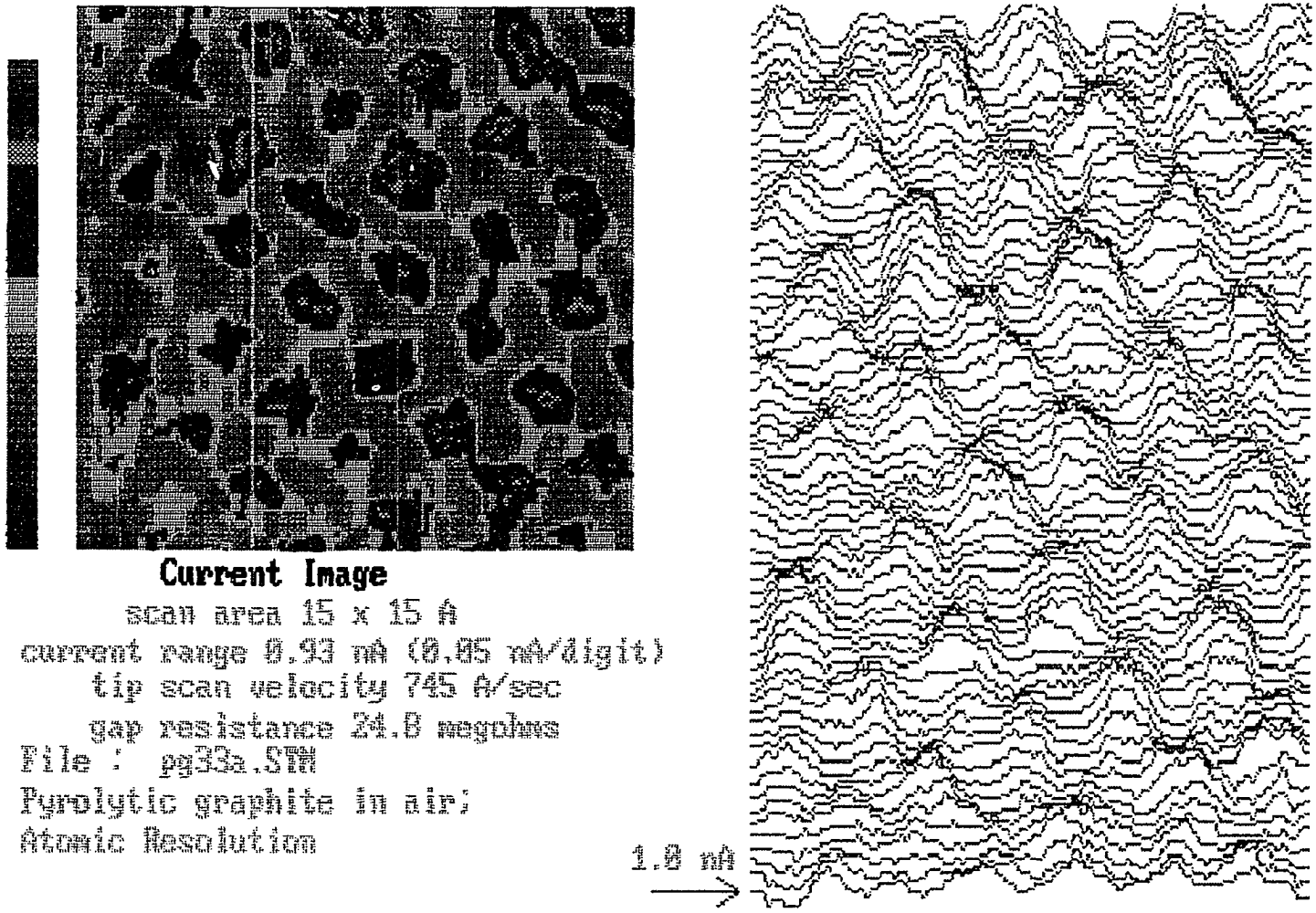

Figure 4.5. Constant height image of APG in air

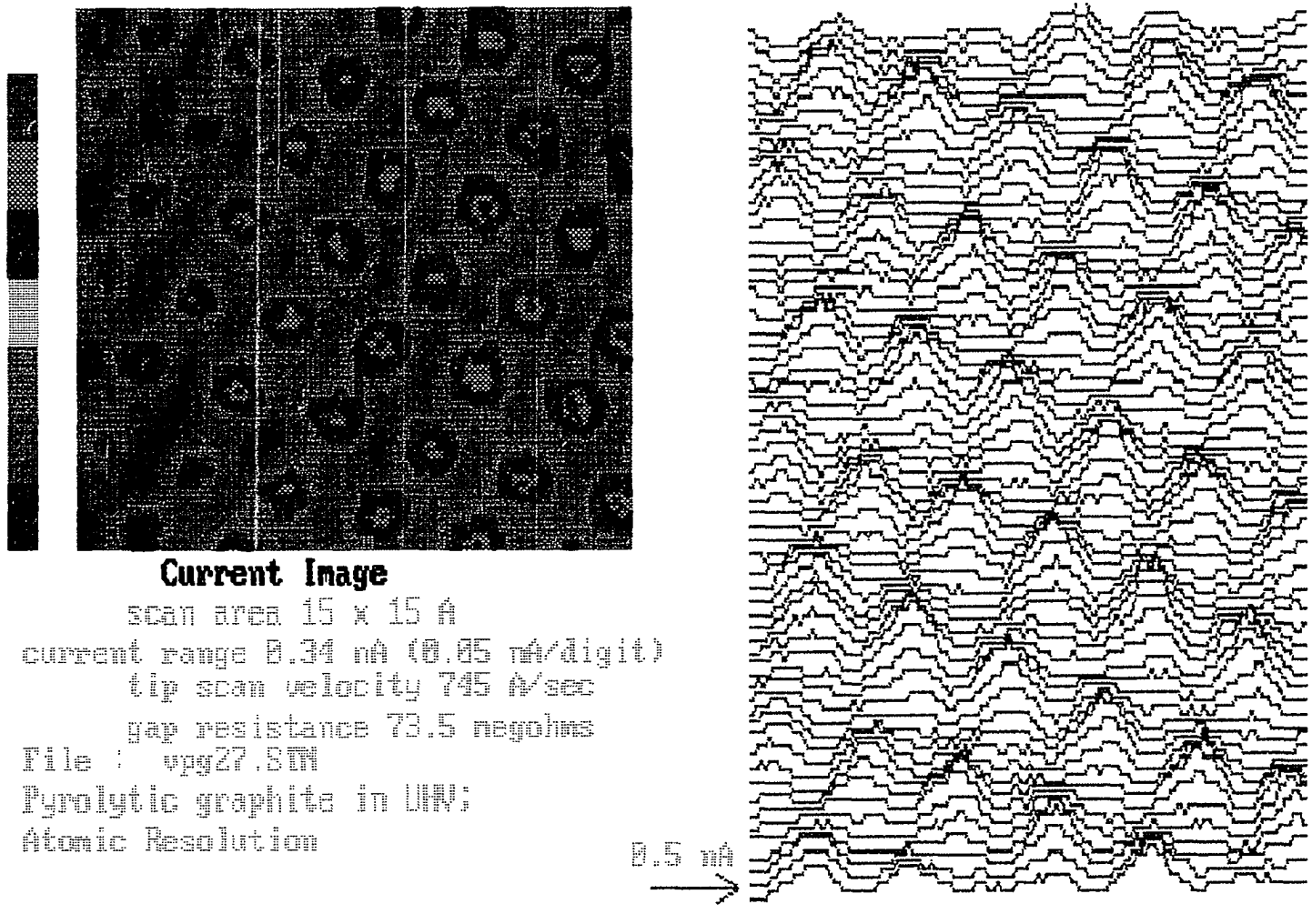

Figure 4.6. Constant height image of APG in vacuum

the system, as can be seen by comparing Figures 4.5 and 4.6. (Differences in tunneling conditions do not account for the variation in the images.) To minimize the effects of acoustic vibrations, a glass bell jar was placed over the entire microscope head. When the STM is placed in vacuum, acoustic vibrations are no longer a factor.

To calibrate the STM system, the peak-to-peak distance is determined by measuring the distance between the geometric centers of neighbors along the three reference vectors (**a**, **b**, and **c** in Figure 4.4), and averaging them. The average peak-to-peak distance for each graphite image is listed under ΔP in Table 4.1. There are two features that emerge from the information in the table. First, there is an initial variation of ΔP in the images, which is due to piezoelectric and thermal drift as the system reaches equilibrium. This can be seen in the VPG data of Table 4.1 which has been separated into three groups. VPG 14 was taken shortly after the tip was engaged and the system was still in transition. VPG 27 and VPG 29, along with other images not shown here, show signs of settling, with the average ΔP around 2.72 Å. After an hour break, images VPG 36a through 86d were the most stable group. Images taken the following day with the same tip (not presented here), show even more stability in the images and in ΔP.

Beside the variation in ΔP, the closed packed graphite pattern is skewed from that depicted in Figure 4.4. The skewed pattern is attributed to the tip not perpendicular to the surface, and non-orthogonal piezoelectric drives. This geometric distortion remains constant from scan to scan for a given set of data. Figure 4.7 compares

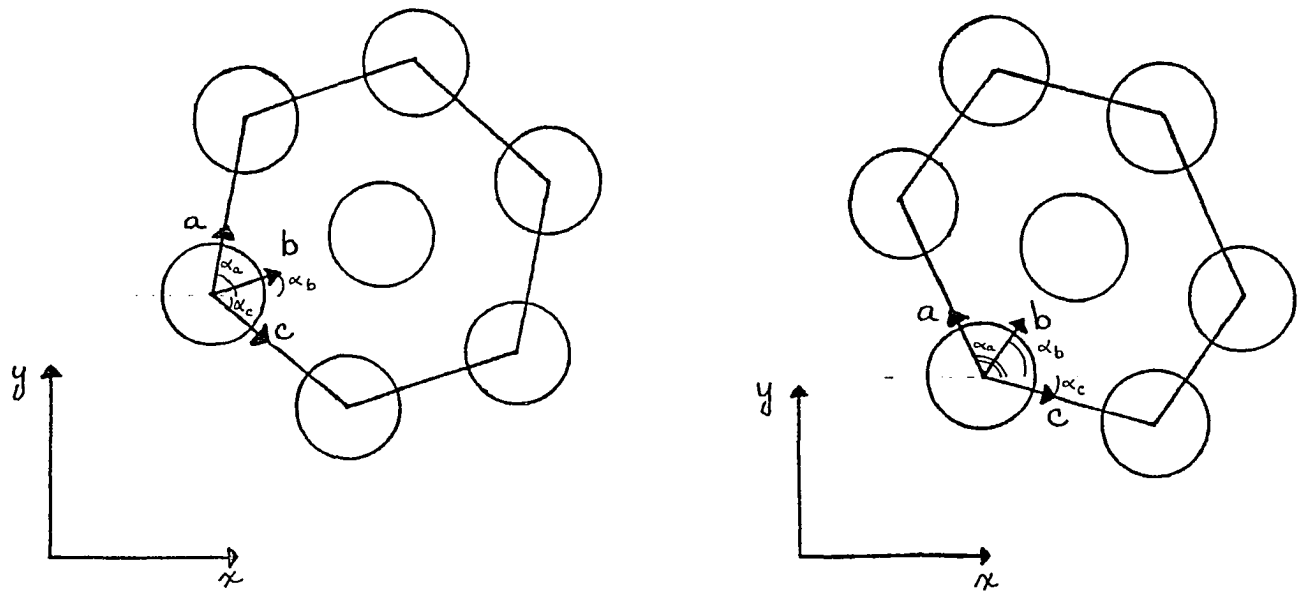

Figure 4.7. Unit cells of APG images for: a) Figure 4.5 and b) Figure 4.6. Angular orientations for the reference vectors, **a**, **b**, and **c**, are given by α_a, α_b, and α_c

the skewed unit cell of Figure 4.6 with the non-skewed cell of Figure 4.5. Table 4.2 lists the average angular orientations of the reference vectors, given as α_a, α_b, and α_c in Figure 4.7, for each graphite data set.

After the individual peak-to-peak averages were measured, the overall average for the entire set of images were obtained and listed in Table 4.2. Each data group is listed separately with the PET set used indicated. Between the air (AU and PG) and VPG images, the PETs were broken during a tip exchange and had to be replaced. Between the 829 and 615 images, the entire microscope head was replaced in an attempt to track down the source of noise that had begun to effect the STM system. The discrepancy of the listed averages with the accepted spacing of 2.46 Å is due to the piezoelectric constant for the specific PET set used. The manufacturer's listed value for the X and Y piezo constant is 15 Å/V with a tolerance of 10%, therefore, the piezo constants for the STM were re-calibrated, and the revised values, which are listed in Table 4.2, were then used in any subsequent imaging.

After the piezos were calibrated, the images were further examined for any dependence of image clarity on tunneling conditions. The images which consistently exhibited well-defined peaks and a strong current signal, were obtained with bias voltages around -50 mV and the current setpoint around 2 nA. In addition to determining the "ideal" tunneling conditions for graphite, it was noted that the peak shapes varied in many of the scans. It was further observed that the distortions were oriented in preferred directions. The following section discusses the observed

Table 4.2. Average graphite peak-to-peak spacing, corrected piezoelectric constants, and reference vector orientations for the APG results listed in Table 4.1

File Group	PET[a] Set	ΔP_{ave}[b] (Å)	% Diff	PC[c] (Å/V)	Reference Vector Orientation[d] α_a	α_b	α_c
PG	1	2.67	+8.5%	13.8	79°	18°	-41°
VPG	2	2.61	+5.9%	14.1	109°	48°	-16°
829	2	2.61	+5.9%	14.1	106°	48°	-16°
615	3	2.35	-4.5%	15.7	83°	22°	-27°

[a]PET = Piezoelectric Transducer.

[b]ΔP_{ave} = average peak-to-peak distance for APG graphite.

[c]PC = Piezoelectric Constant for the piezos used in the McAllister/RHK tripod scanner.

[d]Vector orientation is shown in Figure 4.7.

distortions, the commonly cited explanations, and the nature of the distortions.

2. Peak Distortions

Peak distortions resembling ovals or ridges, instead of circles, were seen in a number of images. The onset of the distortions was first assumed to be linked to the tunneling conditions, but no correlations of the appearance of the distortions with the bias voltage, scan speed, or tunneling current were found. Since graphite has primarily been used as a calibration tool, little attention has been given in the literature to the origin of the distortions, although most published graphite images contain similar distortions to those observed in Figures 4.8 to 4.20. (Anomalously large corrugations have been reported by some groups[93,95,101] while imaging in air and in the constant current mode, but as the corrugations do not occur in UHV nor in the constant height mode, this is not the source for the distortions.)

Left and right scan direction images were first compared to check for the existence of mini-tips. For the images presented here, there is no discernible difference between the two scan directions, as can be seen by comparing the left scan of VPG 27 in Figure 4.8 with its corresponding right scan in Figure 4.6. When the system was allowed time to reach equilibrium, thermal and piezoelectric drift were of minor importance in the imaging of graphite. Subsequent scans were monitored, with the resulting drift on the order of 1 Å per minute, which allowed features to be followed from scan to scan. Scan were usually recorded at a rate of

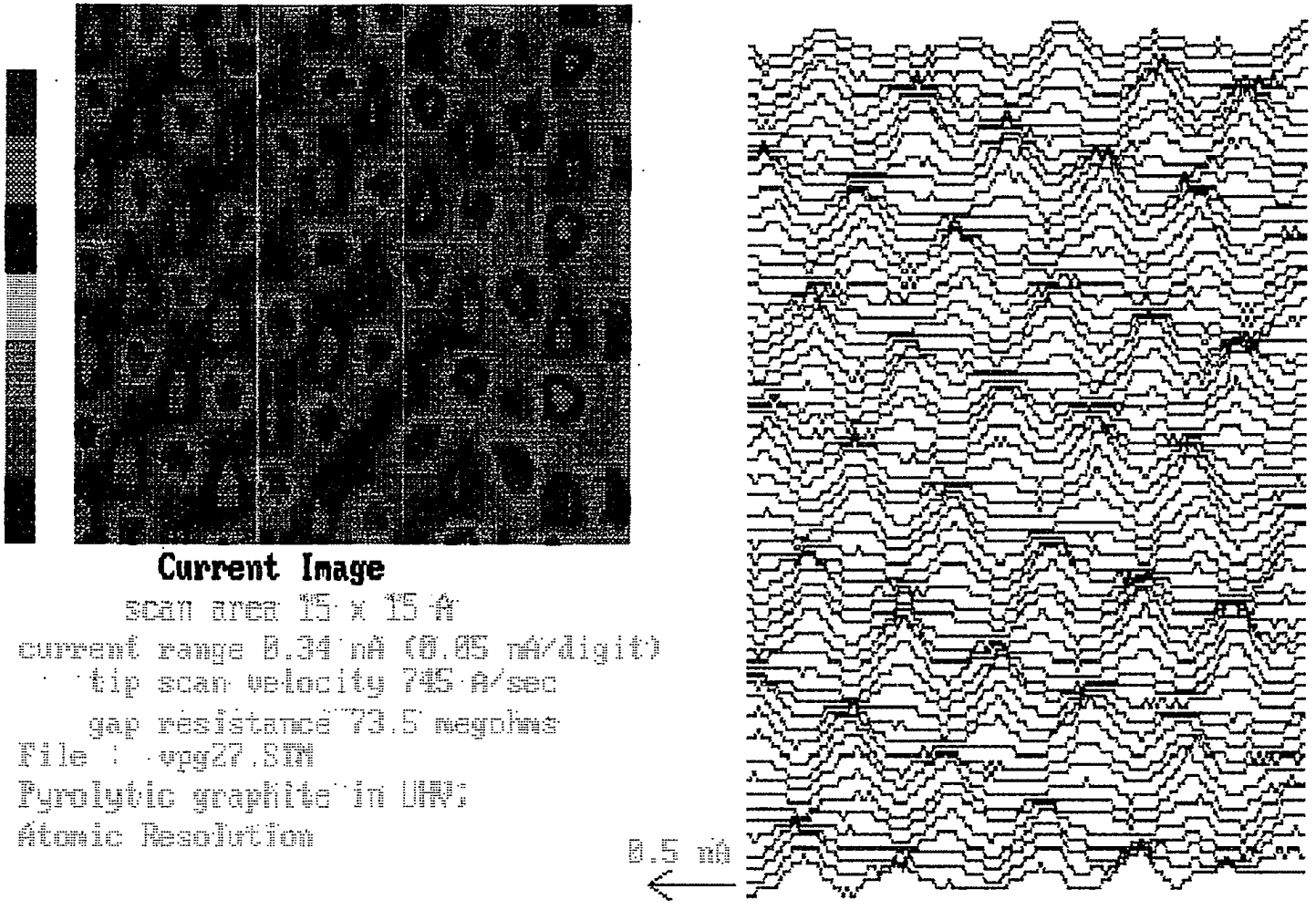

Figure 4.8. Left (-x) direction scan of Figure 4.6. Note that a comparison of the two figures results in no discernible shift in the location of features as would be caused by the existence of a multiple tip

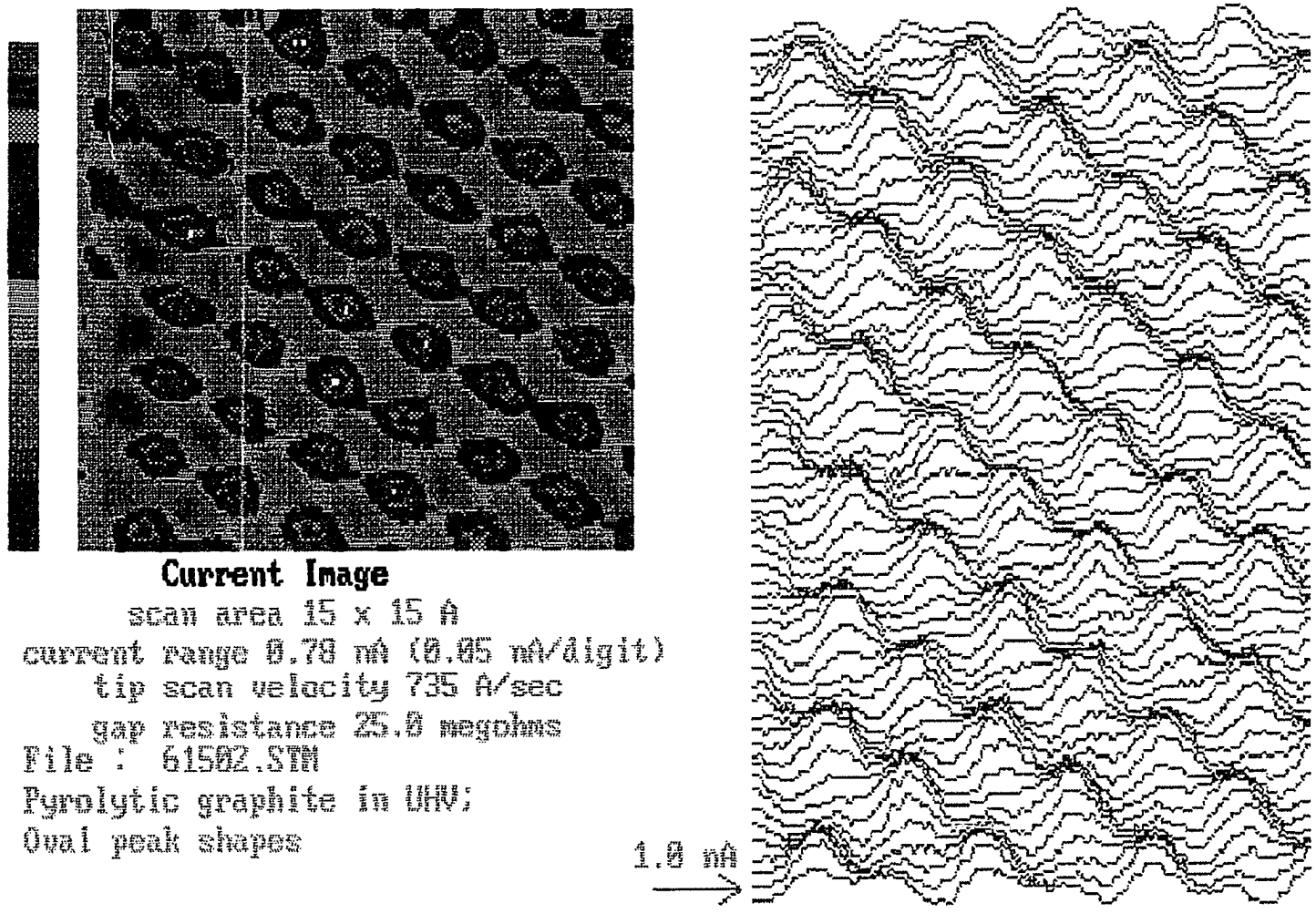

Figure 4.9. Constant height image of graphite showing oval peak distortion

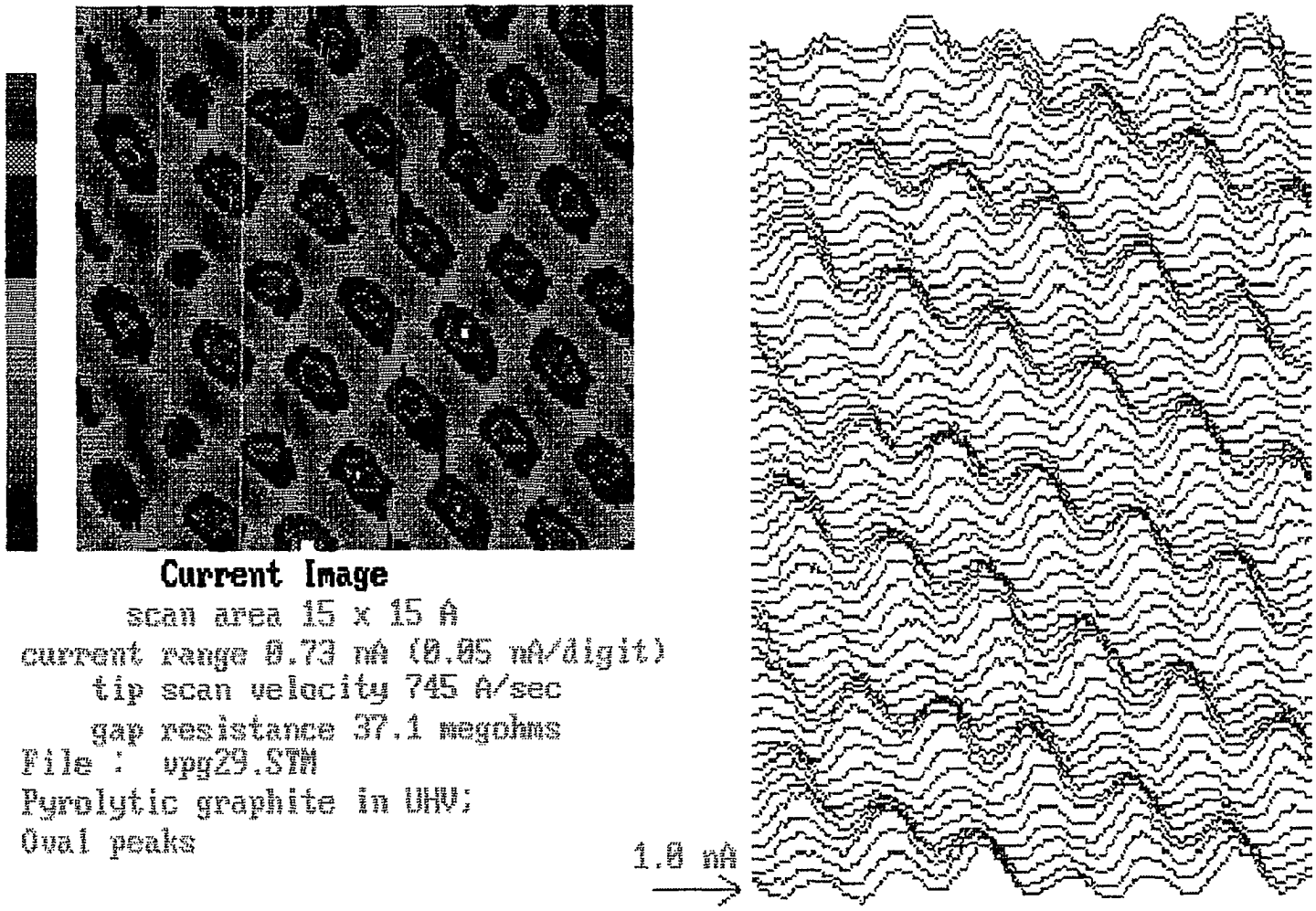

Figure 4.10. Constant height image of graphite showing oval peak distortion. Orientation of the peak varies with the orientation of the unit, as can be seen by comparing with Figure 4.9

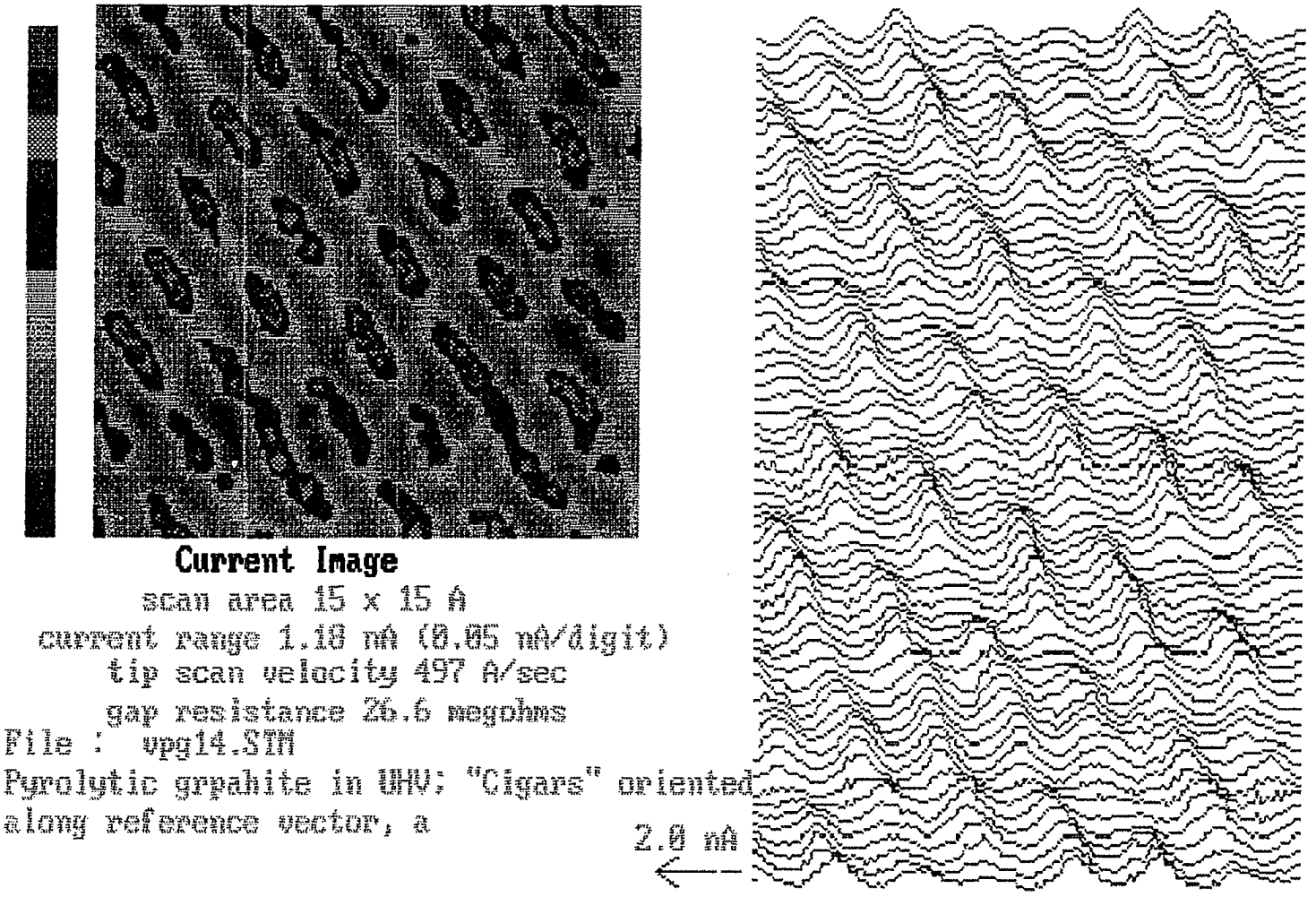

Figure 4.11. Constant height image of graphite showing cigar-shaped distortions aligned in the direction of reference vector, a

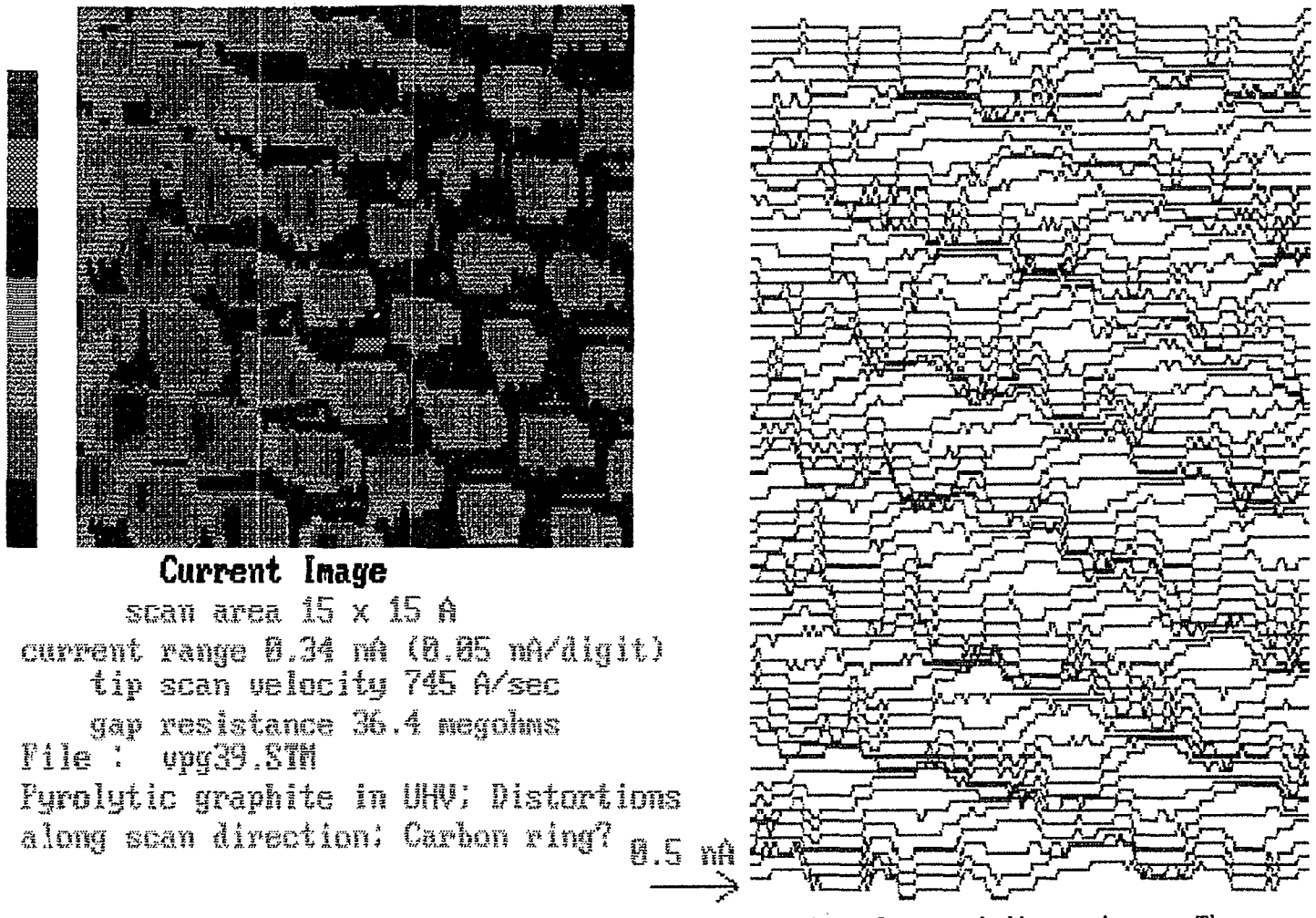

Figure 4.12. Constant height image of graphite showing elongated distortions. The elongations could be aligned with the graphite reference vector, g_c, but it is difficult to isolate from any effects due to scanning in the x-direction

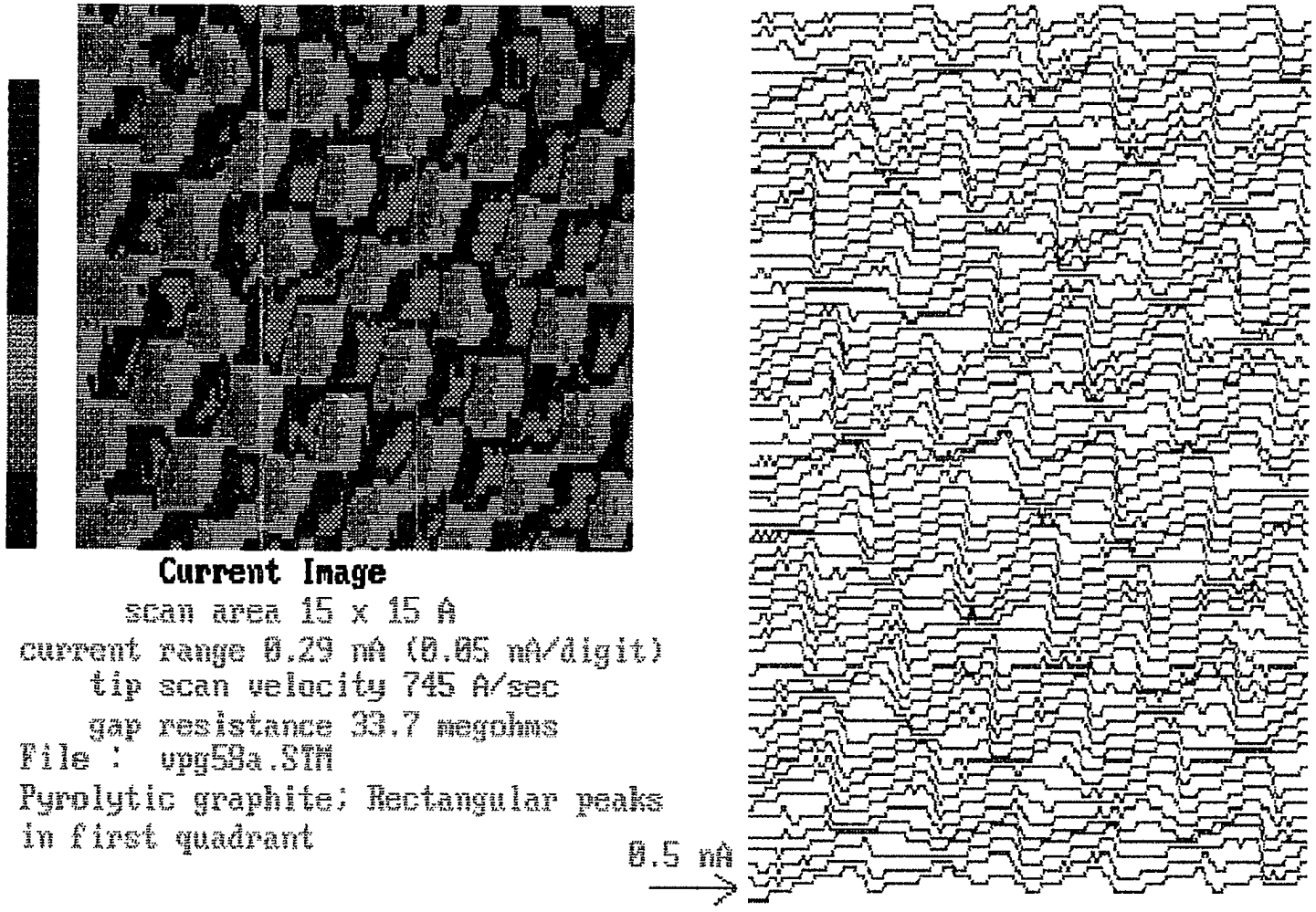

Figure 4.13. Constant height image of graphite showing rectangular distortion aligned with graphite reference vector, g_b

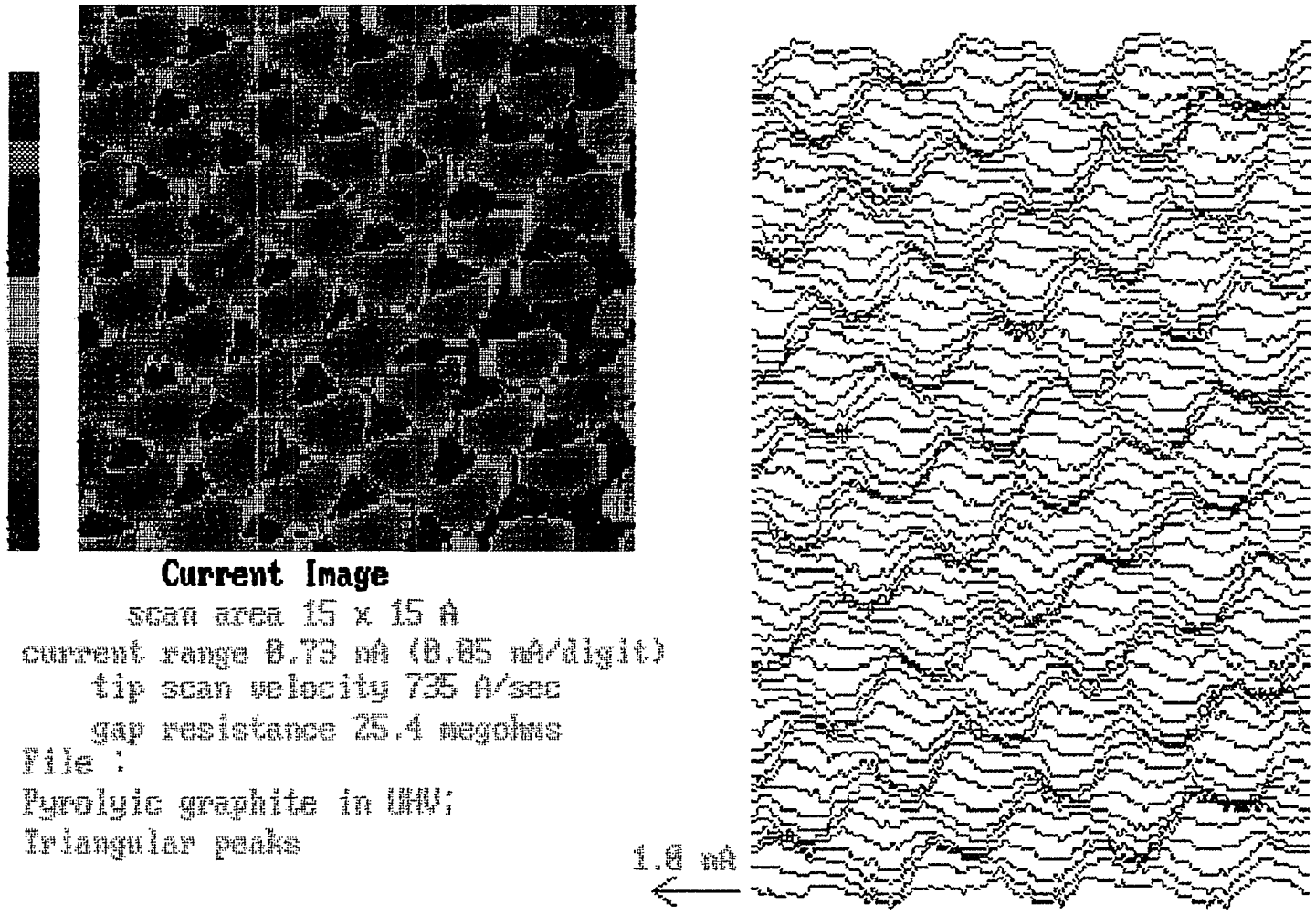

Figure 4.14. Constant height image of graphite showing triangular distortions

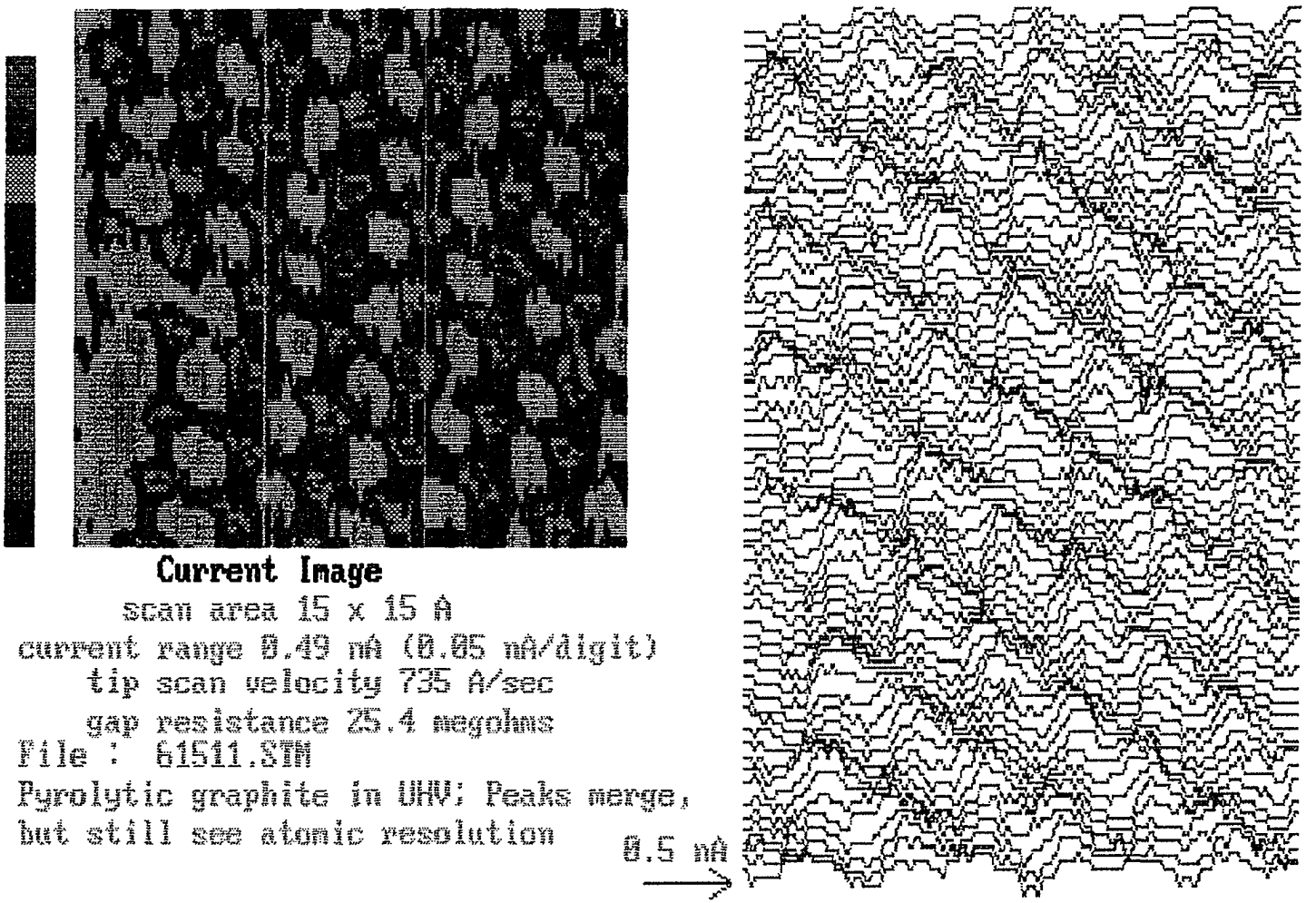

Figure 4.15. Constant height image of graphite showing irregularly shaped distortions which are interconnected along reference vector, b

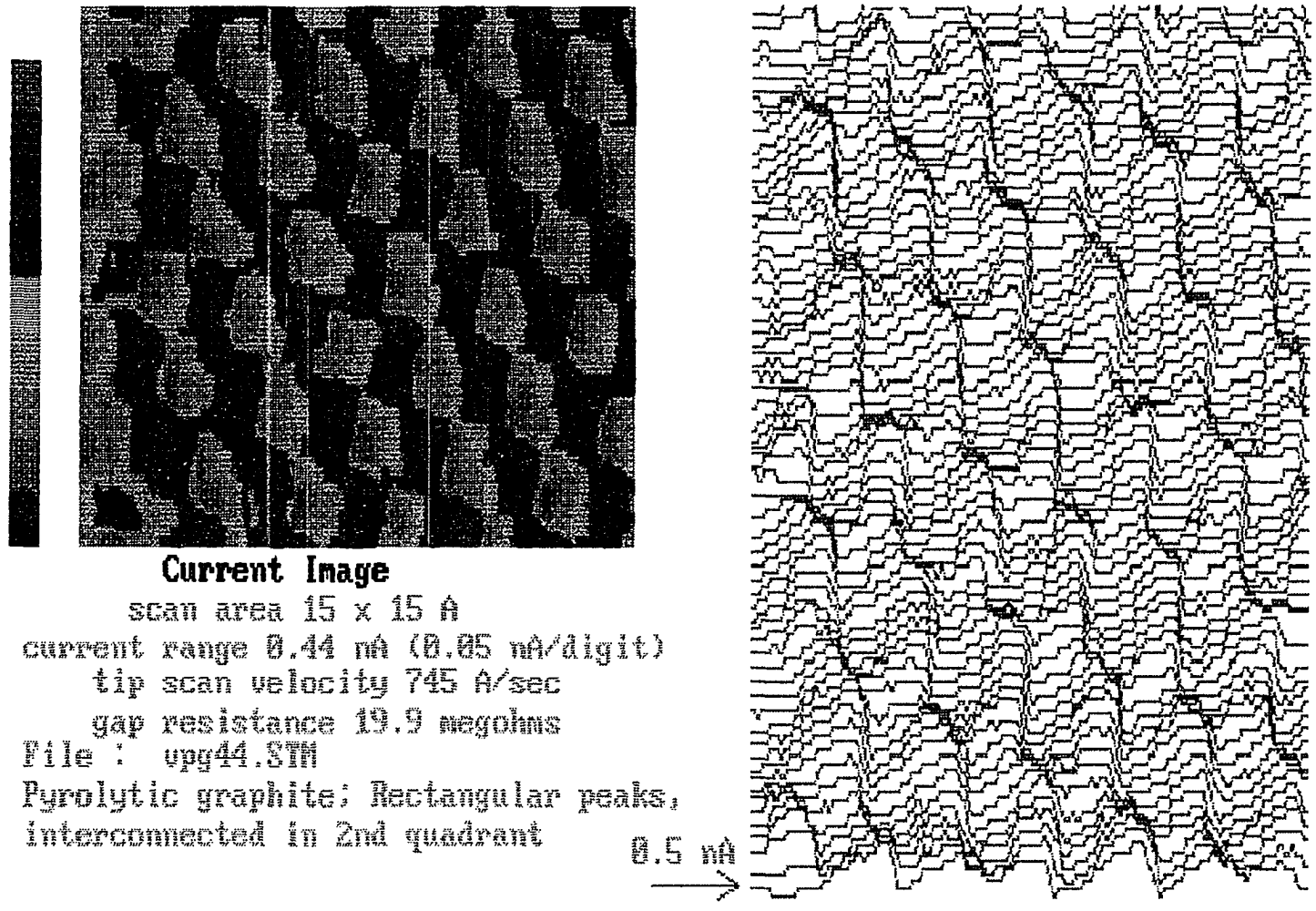

Figure 4.16. Constant height image of graphite showing rectangular distortions which are interconnected along reference vector, a

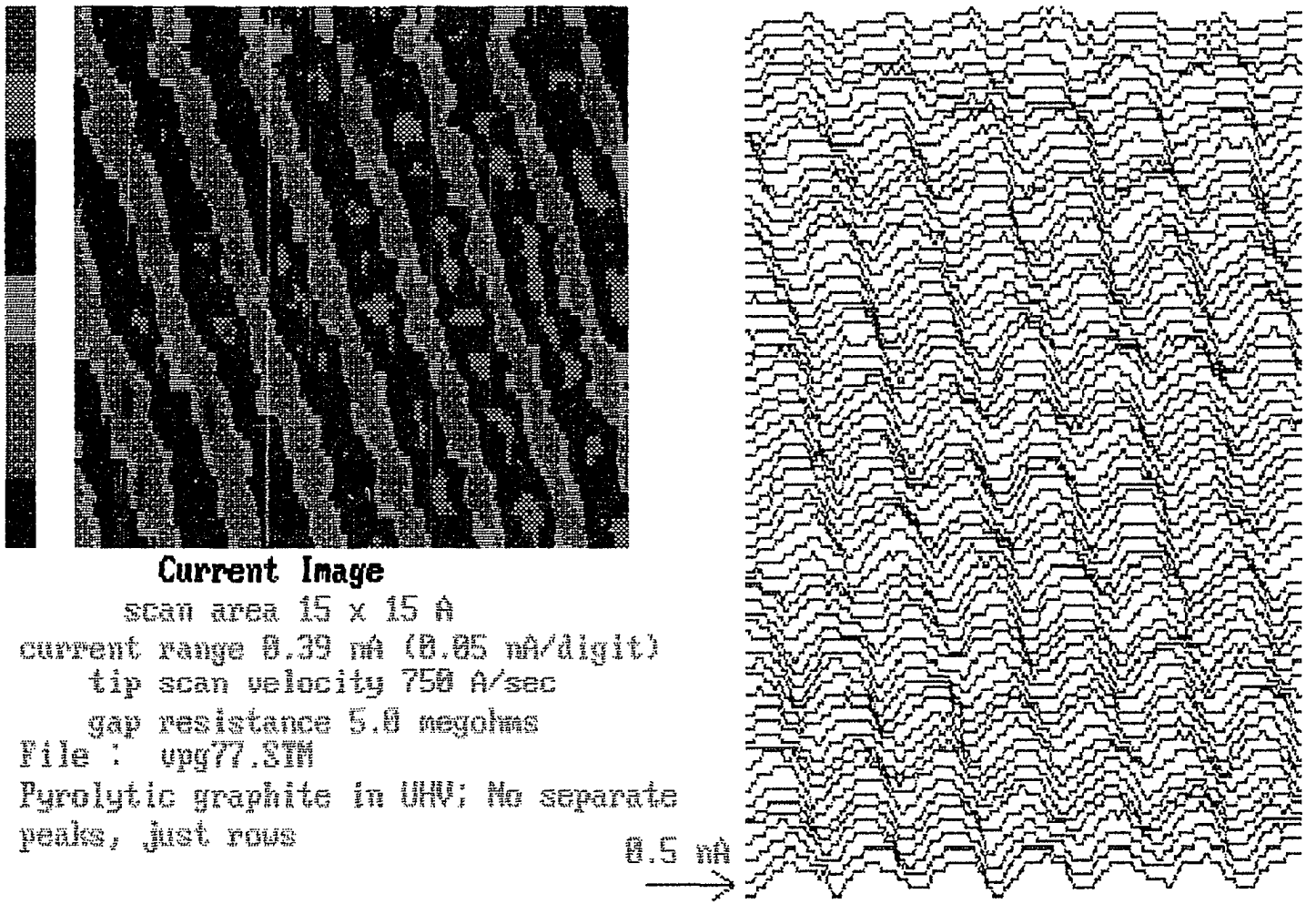

Figure 4.17. Constant height image of graphite showing row patterns along reference vector, a, with no individual peaks apparent

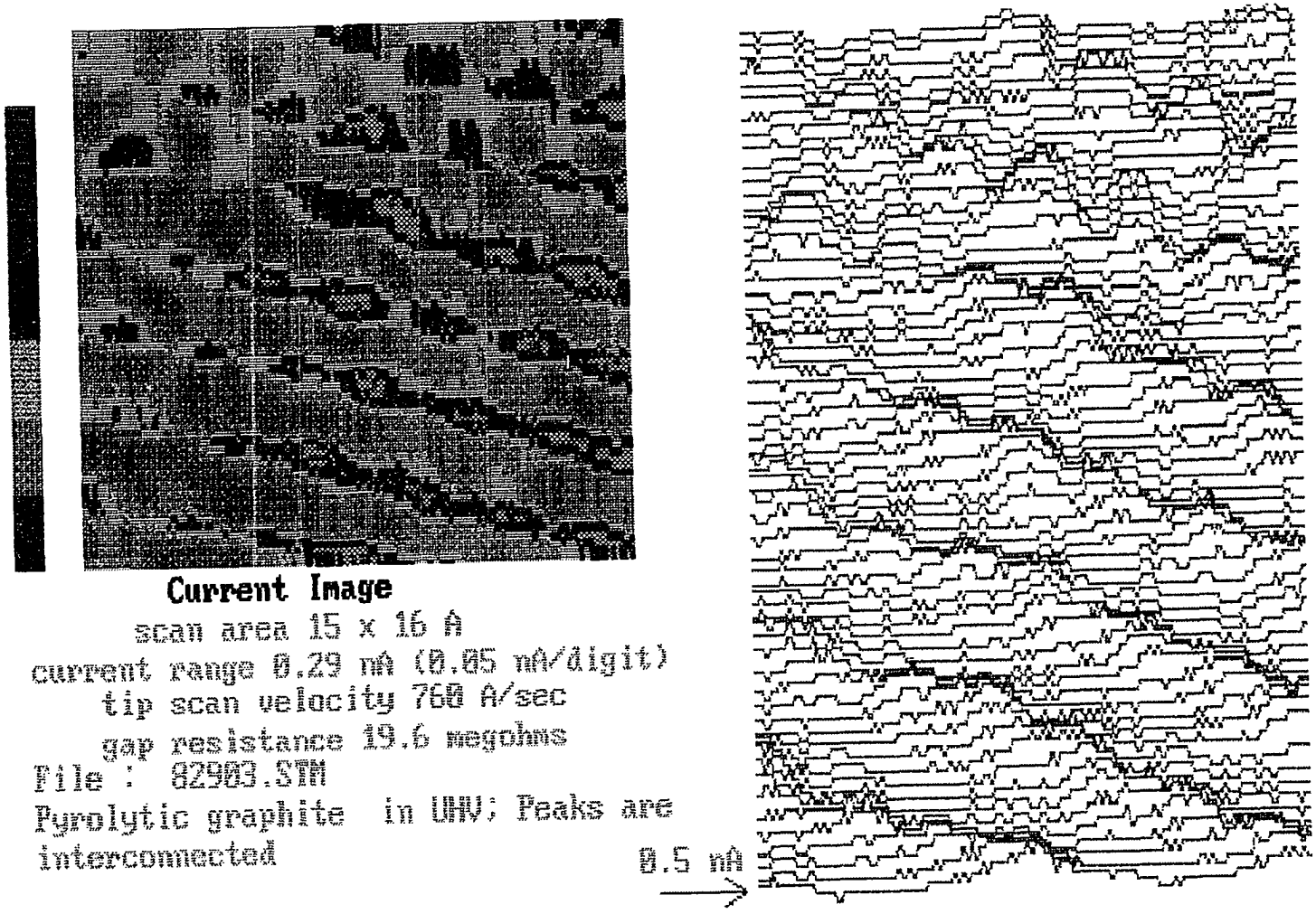

Figure 4.18. Constant height image of graphite showing elongated distortions which are interconnected along reference vector, c

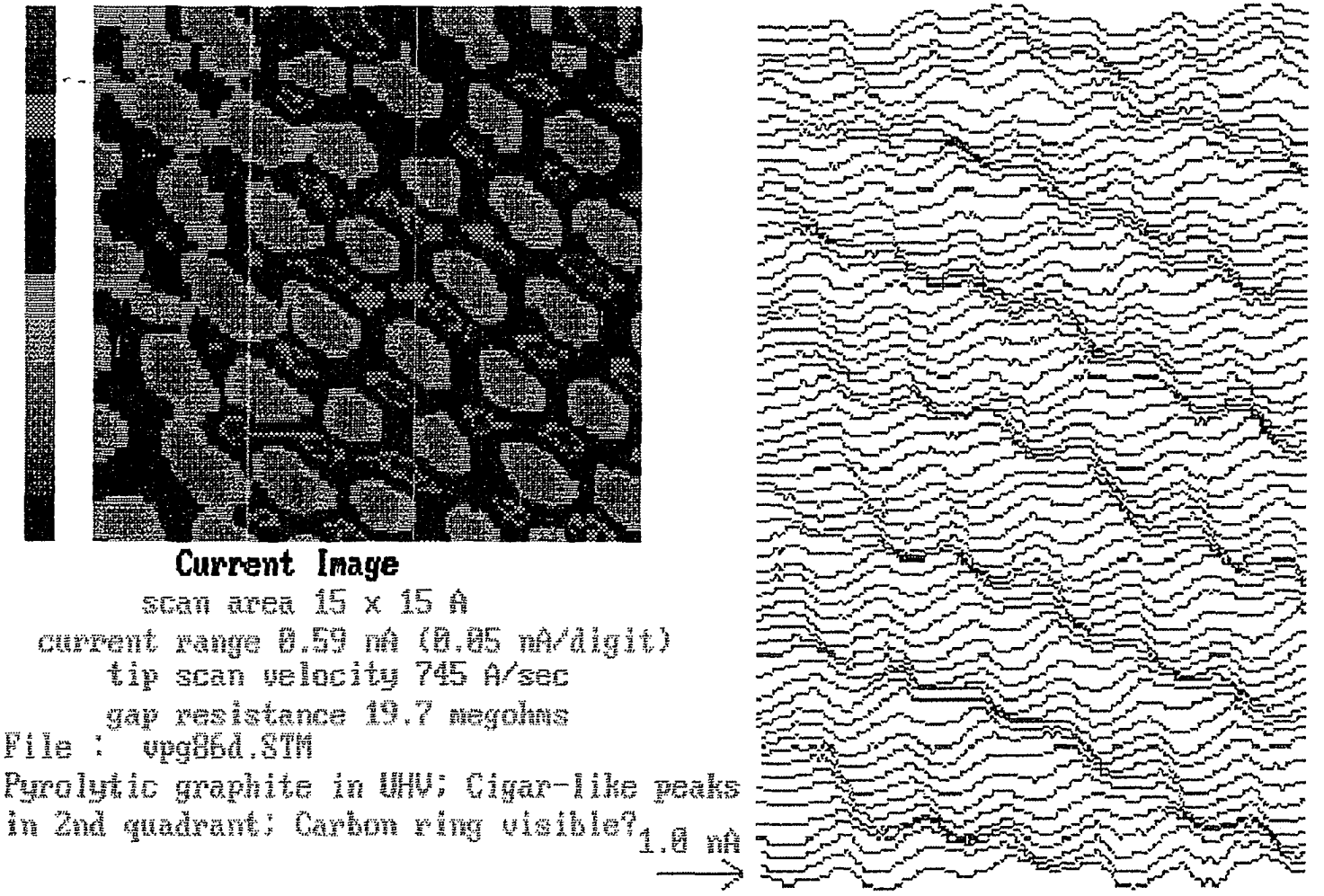

Figure 4.19. Constant height image of graphite showing elongated distortions along graphite reference vector, g_a. The outline of the graphite hexagonal unit cell, with side length, 1.42 Å, is also visible

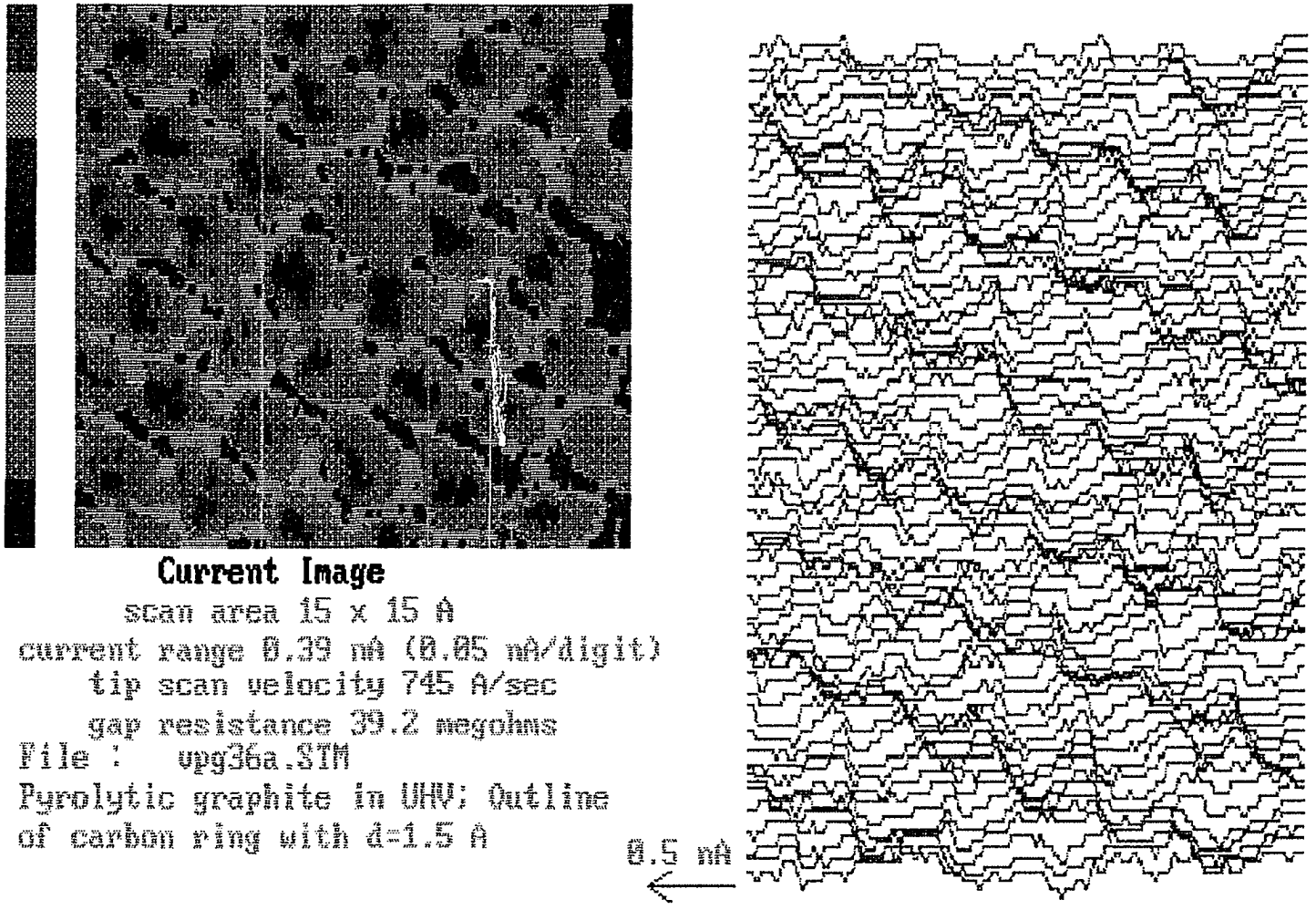

Figure 4.20. Constant height image of graphite showing the faint outline of the graphite unit cell with side length, 1.42 Å

two, or more, per minute.

The peak distortions can be broken into two main categories: peak shape and peak orientation. The most common peak shape was the cigar, oval or rectangular shape, as shown in Figures 4.9 through 4.13. The oval (or oval-like) shapes occurred approximately 40% of the time, with no dependence upon the tunneling conditions. The figures presented are a cross-section of the oval shapes that have been imaged. The round peaks, similar to Figures 4.6 and 4.8 occur around 20%, while the remaining group, the triangular peaks of Figure 4.14, complete the collection of "well-defined" shapes. Another large group of images, approximately 30% of all images, show irregular or no single peak shape, as observed in Figure 4.15. Often, the individual peaks are not clearly resolved, but appear interconnected into row patterns (Figures 4.15 through 4.18). These row patterns are oriented only in the directions along the reference vectors **a**, **b**, and **c**.

In addition to the row patterns, the peaks themselves are oriented along preferred directions, which are indicated as g_a, g_b, and g_c in Figure 4.21 (a reproduction of Figure 4.4). The g vectors correspond with the atoms in the graphite unit cell that contribute little to the tunneling current. The peaks which are aligned along the g_c direction (refer to Figures 4.12 and 4.18) are difficult to distinguish from any distortions that may arise from scanning in the x-direction, but this does not explain the peak orientations along g_b (Figures 4.13 and 4.16) nor along g_a (Figures 4.10 and 4.19). In some instances, a new pattern, based on the **g** vectors, is formed, which involves both peak orientation

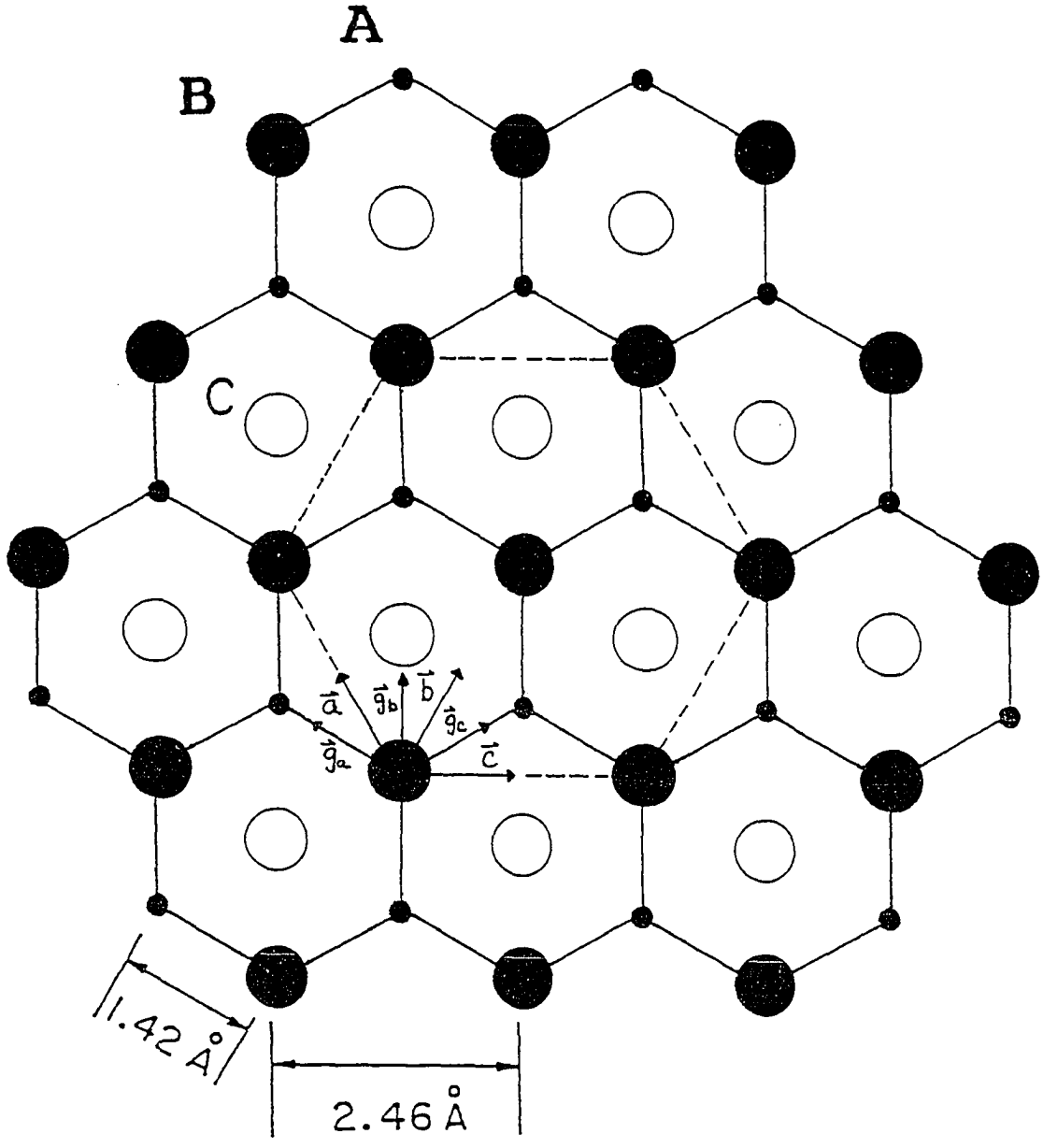

Figure 4.21. Figure 4.4 repeated with peak distortion directions indicated as g_a, g_b, and g_c, which coincides with the graphite unit cell reference vectors

and shape, as in Figures 4.19 and 4.20. The higher portions in the images outline hexagons of side length, 1.45 Å, which corresponds well with the interatomic spacing of 1.42 Å for graphite.

Those groups that have acknowledged the STM peak distortions have tried to explain the origin of the distortions as due to one, or more, of the following:

a) asymmetry in the X and Y piezo scanners;[83,102-106]

b) asymmetry in the tunneling tip;[93,107-109]

c) some other effect of the tip;[105,110,111]

d) thermal and/or piezoelectric drift;[83,87]

e) tip-sample interactions;[9,112-116] or

f) an artifact of the system that can be removed by an appropriate choice of filtering.[117]

As discussed above, piezoelectric and thermal drift are not factors due to the equilibrium of the system and the speed of the scans (2.5 sec to complete one constant height image). Asymmetrical piezo scanners or tunneling tip do not account for the preferred orientations which are observed. Multiple tip effects, on the scale of the scan sizes (15 Å or less), were not observed in the right versus left comparisons. In addition, changes in the structure of the mini-tips were not observed, as evidenced by the stability of the tunneling current and the reproducibility of the images. The quality of the current signal changes noticeably if the tip atoms closest to the sample (and, hence, the principal atoms involved in the tunneling process) rearrange or acquire adsorbates.

The peak distortions have been observed under a variety of imaging conditions:

a) in different ambient;

b) with different tunneling microscopes (The Digital Nanoscope II, used for additional imaging, will be described in Section IV.D.);

c) on different sample materials;

d) with different tip materials (tungsten, PtRh and PtIr); and

e) with different tip-sample combinations (VPG and 829 samples were taken on the same sample of APG, but with different tips, while PG and 615 were imaged with both tips and samples different.).

To eliminate the effects of the tunneling conditions (bias, current setpoint and scan speed), images (File group 615) were obtained only as a function of time. These images indicate no dependence of distortions on the external parameters of tunneling conditions, sample type, or tip material. The time dependence of the distortions does indicate, however, some form of interaction existing between the tip and the graphite.

Tersoff,[95] Tomanek and Louie,[99] and Batra and Ciraci[100] have previously examined the effects of the electronic states near the Fermi level at the K point in the Brillouin zone to explain the nature of the graphite images obtained. From their work, the B sites are now accepted as the sites contributing the most to the LDOS (local density of states), and, hence, to the tunnel current. However, interactions between the tip and the graphite surface, which may disturb the surface electronic states and, in turn, the images obtained, have only recently been investigated. In the next section, Kobayashi's and Tsukada's[118-120] theoretical work on

the effect of the contribution of the tip states to the tunneling current, is examined.

3. Effect of Tip Electronic States on Graphite Images

From Section II.D, only the LDOS of the surface is used in the calculations for the current density. This introduces a simplification in the calculation, but fails to include real tip effects that may alter the images acquired. Kobayashi and Tsukada recently performed various numerical simulations on the effects of different tip orbitals on the resulting STM graphite images.

The tunnel-active orbital of the tip was first chosen to be the bonding and anti-bonding orbitals of the hydrogen molecule, because it is the simplest case beyond the spherical orbital approach traditionally employed. The bonding orbital is distorted from a sphere, but has no nodal planes. However, the anti-bonding orbital has a nodal plane which provides some general characteristics of STM images which depend on the tunnel-active orbitals with a node.

When the tip orbital is the bonding orbital and is oriented along the x-axis, the calculated STM image of graphite as shown in Figure 4.22, exhibits a slight elongation of the peak along the tip orbital direction, with the peaks located in the appropriate B-atom sites. The shape of the peaks is similar to the triangular peaks observed in Figure 4.14. However, when the anti-bonding orbital axis is oriented along the x-axis, a chain-like image is observed (similar to Figure 4.11), with the long axis of the chain perpendicular to x. In addition, the peak position is

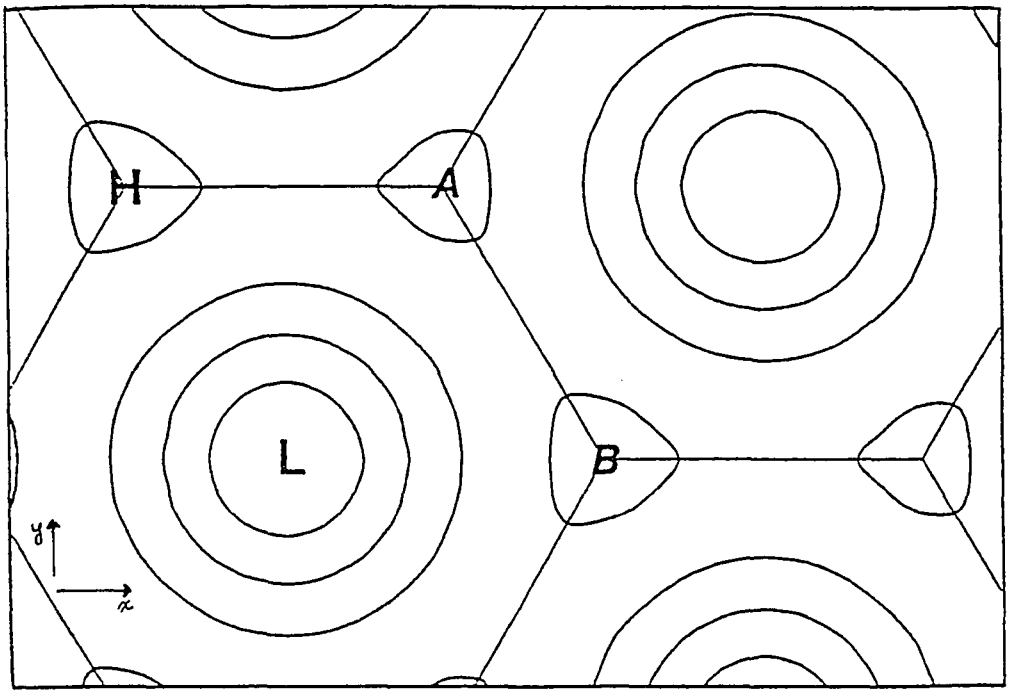

Figure 4.22. Calculated STM image of graphite when the tip orbital is H_2 bonding, and the axis of the orbital is parallel to the x-axis. H and L are the highest and lowest regions of the tunnel conductance. A and B are the A-atom and B-atom sites

no longer the B-atom site, but has shifted closer to the C-atom site, as shown in Figure 4.23.

When the anti-bonding tip orbital direction is rotated 30° from the x-axis, the hexagonal closed-packed lattice is recovered, but with some differences, as shown in Figure 4.24. The peak position has shifted from the B-atom site and the elongation is, again, perpendicular to the tip orbital axis. When the orbital is tilted 30° in the x-z plane, interference effects of two tip atoms can be seen in Figure 4.25. In Kobayashi's and Tsukada's calculations, the possibility of a double tip was included, and the expression for the current then involved a term corresponding to the interference effects (refer to Reference 119). The calculated STM image for graphite, with the interference effects included, is the same as shown in Figure 4.25. Therefore, some of the peak distortions observed in Figures 4.9 though 4.21, can be attributed to an interference effect of multiple tips, although this is not the only possibility, as explained below.

Kobayashi and Tsukada further explored the effect of the tip on the STM images by modeling their tip as a W_{10} cluster (the cluster is comprised of ten tungsten atoms), which is aligned to the [111] direction of the crystal, as shown in Figure 4.26. A first-principles local density approximation (LDA) method[120] was used to calculate the surface and tip electronic states. Previous calculations[121] for the electronic states of various tip models have indicated the tunnel current is mostly contributed by the tip states with a large d_z^2 component of the tip atom closest to the surface. When the main component of the tip orbital is

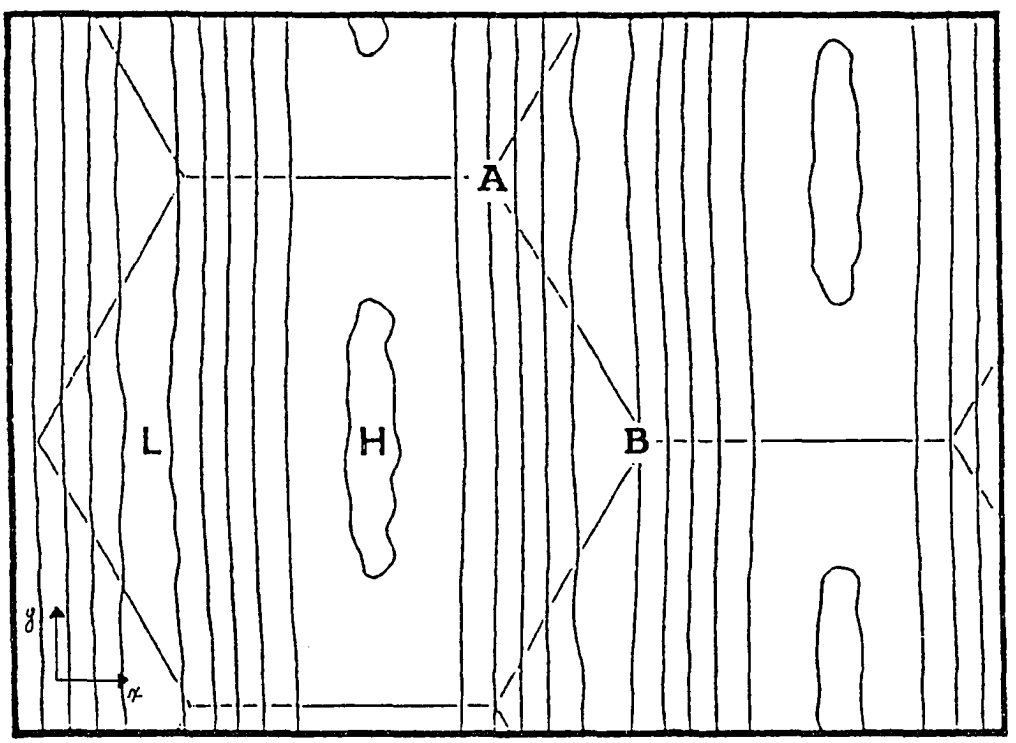

Figure 4.23. Calculated STM image of graphite when the tip orbital is H_2 anti-bonding, and the axis of the orbital is aligned with the x-axis. The chain-like features are similar to those observed in Figure 4.11

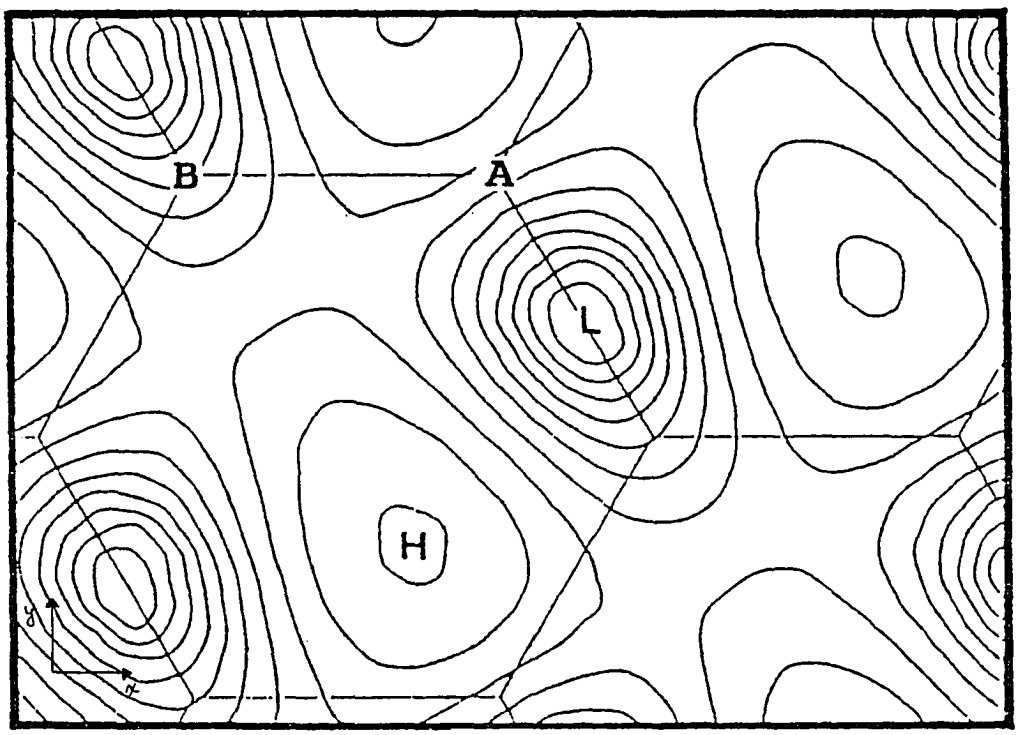

Figure 4.24. Calculated STM image of graphite when the tip orbital is H_2 anti-bonding, and the axis of the orbital is rotated 30° from the x-axis. The oval-shaped features are similar to those observed in Figures 4.9 to 4.13

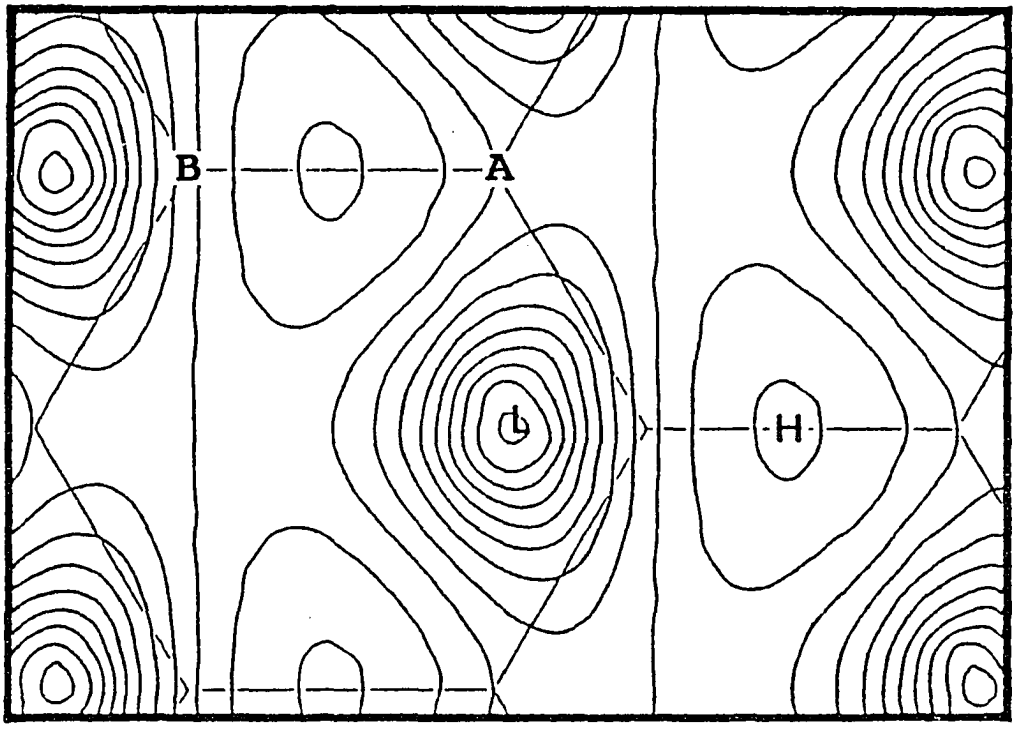

Figure 4.25. Calculated STM image of graphite when the tip orbital is H_2 anti-bonding, and the axis of the orbital is tilted 30° in the x-z plane

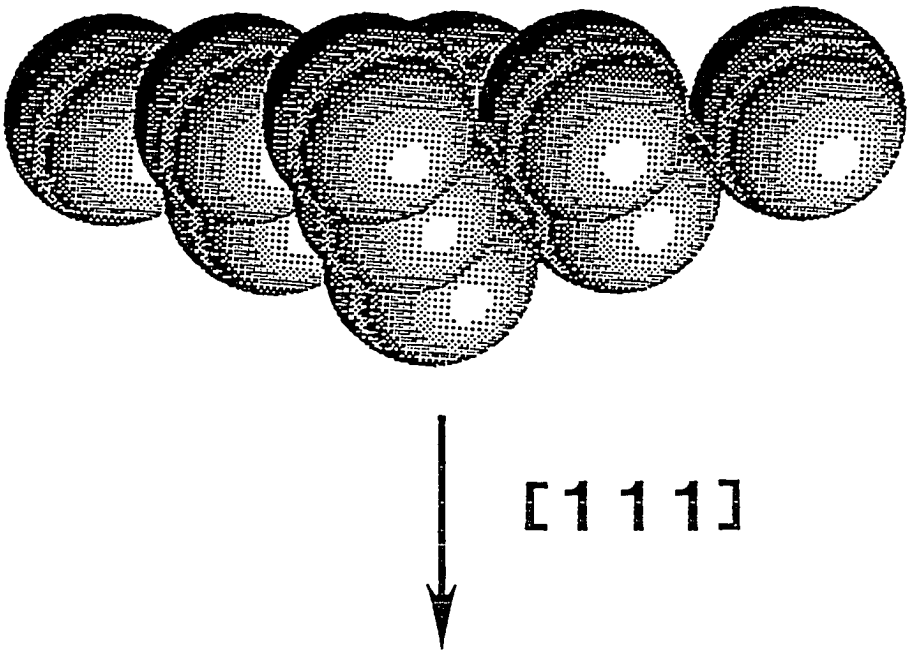

Figure 4.26. W_{10} cluster used as a model for the tip in the simulations of Kobayashi and Tsukada

d_z^2, the charge density of the top atom is symmetrical around the z-axis, as shown in Figure 4.27, and the images indicate the same triangular peak shapes as seen in Figure 4.22.

When the three-fold symmetry axis of the tip is no longer perpendicular to the surface, but is tilted, the resulting images are similar to Figures 4.24 and 4.25, where the peak position not only alters shape, but also shifts from B-atom location. The charge density of the tip orbital used in this situation, is shown in Figure 4.28. The top atomic orbital makes the largest contribution to the current, but it has no d_z^2 component and is not symmetric about the z axis. The origin of the anomalous images is, therefore, clearly due to the electronic, not the geometric, structure of the top atom.

4. Conclusions

Initially, graphite was investigated because of the ease in obtaining atomic resolution. This examination was also necessary to calibrate the piezoelectric components of the STM system. However, there are many questions surrounding the graphite STM images. The peak distortions that have been reported here, and elsewhere, can not be dismissed easily as some nebulous effect of the tip. Multiple tip effects are a possible explanation of the distortions, but such an approach avoids alternate interpretations.

The convolution of the tip and surface electronic states in the tunneling calculations has long been acknowledged as the main obstacle in obtaining a complete understanding of the measured STM images. The

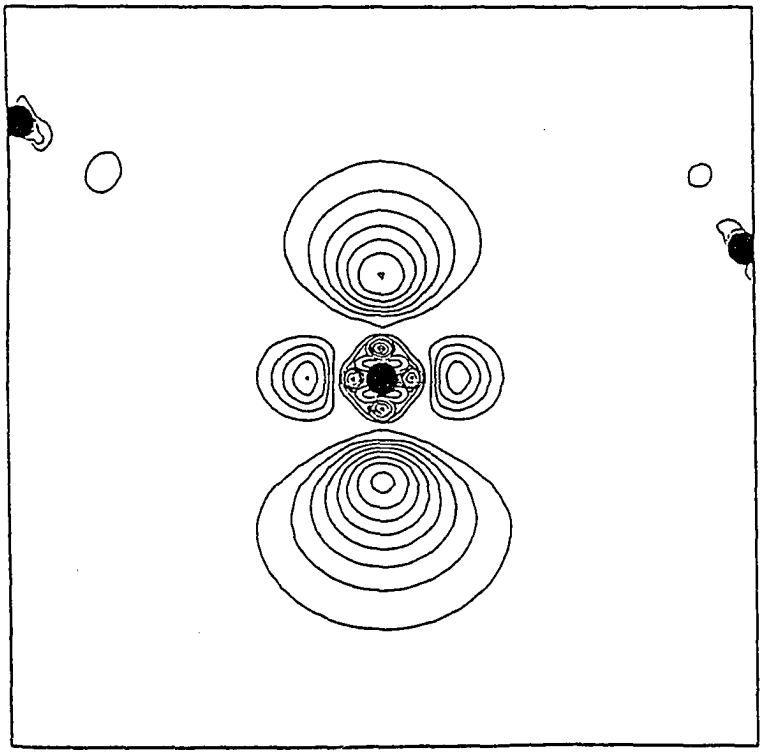

Figure 4.27. Charge density of tip orbital with a large d_z^2 component resulting in images similar to Figure 4.22

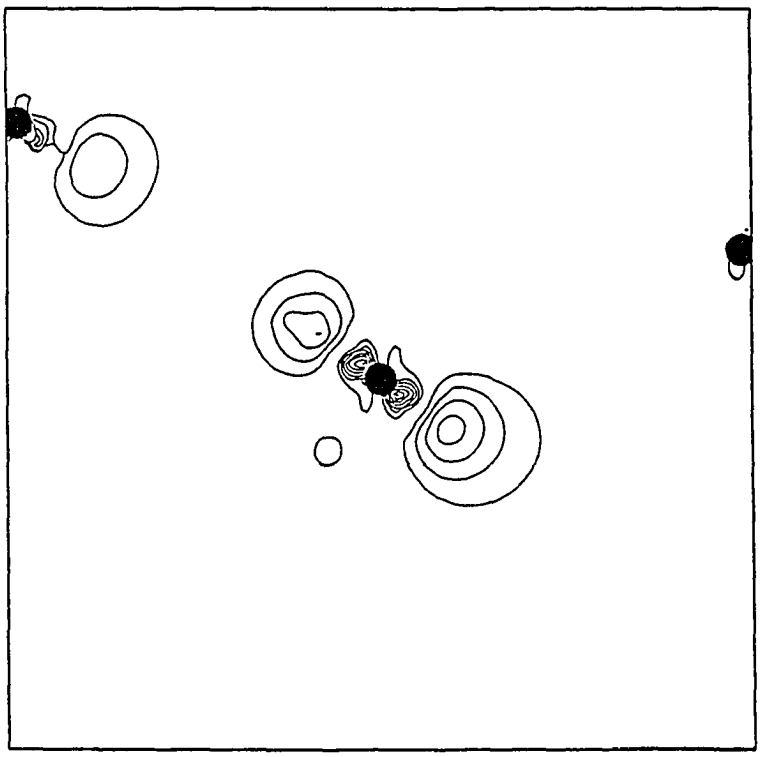

Figure 4.28. Charge density of tip orbital with the top atomic orbital making the largest contribution to the current, but with no d_{z^2} component, resulting in images similar to Figure 4.24

conventional approach has been to treat the tip orbitals as s-wave and well localized, which has resulted in current density caclculations that have qualitatively explained reported images. The modeling of the effect of real tips on graphite images by Kobayashi and Tsukada has demonstrated the importance of the microscopic behavior of the tip. Distortions of features in STM images may be due to the geometric properties of the tip in many situations, but the role of the tip electronic structure is clearly essential for a complete interpretation of the images.

In the matter of graphite, detailed calculations of the effects of the electronic states, as well as the geometric structure, of commonly used tips (tungsten, PtRh, and PtIr) on the tunnel current, need to be performed. From the experimental standpoint, quantitative information about the shifts in the peak location with respect to the graphite unit cell, as well as peak orientations, may provide further insight into the role of the tip in the STM imaging.

The experimental results obtained here for graphite clearly show that the electronic structure of the tip must be taken into account and, in fact, the results are very consistent with those predicted by Kobayashi and Tsukada.

D. Germanium on Silicon

Germanium films, grown on silicon substrates by Ion Cluster Beam (ICB) deposition[122] by Terry Holesinger of the Microelectronics Research Center (MRC) of Iowa State University, were also examined with the STM. The ICB process generates ionized atomic clusters and, by controling the

charge and kinetic energy, accelerates these clusters toward the substrate. Epitaxial growth occurs when each cluster dissociates on the substrate and spreads into a uniform layer. In general, lower substrate temperatures are possible with the ICB process than with other techniques, which is important for limiting dopant diffusion and for maintaining sharp interfaces. Recent studies of the dynamics of ICB film growth[123,124] have shown surface diffusion and cluster spreading increases with higher cluster velocities, thus reducing the need for a high substrate temperature. Although epitaxial films of germanium have been grown,[125] there are many aspects of the ICB growth process that are not fully understood, especially in the areas of cluster size and film growth.

In this section, results are reported for germanium films as a function of: film thickness, deposition conditions, and annealing. The ICB generated films were often disordered on the scale of 100 nm, making the results not only difficult to interpret, but difficult to compare with other published work,[126-128] which has primarily discussed ordered, reconstructed surfaces showing atomic resolution. Additionally, STM studies of disordered systems entail many problems not typically encountered with ordered systems:

a) inability to distinguish between the material of interest and possible contaminants;

b) tunneling conditions differ from sample to sample because of surface states and corresponding changes in the LDOS;

c) non-existence of theoretical work on the surface electronic

structure with which to compare;

d) inability to quantify the STM information; and

e) subjective nature of tunnel image interpretation.

The results, reported in the following sections, were obtained with two different tunnel microscopes. In Section VI.D.1, the McAllister/RHK microscope was operated in UHV, with scan sizes on the order of 750 Å. In Section VI.D.2, a Digital Nanoscope II, with larger scan sizes (on the order of 4500 Å), was operated in air, courtesy of Dr. Eric Henderson from the Zoology department at Iowa State University. Tunneling conditions for all images presented in this chapter are listed in Table 4.3, for the McAllister/RHK STM, and in Section IV.C.2, for the Nanoscope II.

1. McAllister/RHK Scanning Tunnel Microscope Results

a. Surface modification When the sample bias voltage is increased at a rate faster than the feedback system can compensate, the tip often crashes into the surface, and, occasionally, the tip is capable of additional imaging. This situation occurred when the bias voltage was increased from 0.5 V to 5.0 V, by switching the voltage multiplier from 1 to 10. Figures 4.29 through 4.32 are images of the hole created when the tip crashed. Before the tip crash, the surface of the germanium film was devoid of any significant features, so the hole was created by the tip and was not an inherent surface structure. Because of the location of the scan origin, only one-fourth of the hole can be seen in the upper left-hand corner of Figure 4.29.

Table 4.3. Tunneling conditions, vertical range and cleaning methods for germanium samples imaged with the McAllister/RHK Scanning Tunnel Microsocope

Sample	File	V_B (V)	I (nA)	Scan Size (Å)	VR[a] (Å)	Cleaning Method	Figure Number
3-ICB #27	9939	1.75	0.2	550	105	none	4.36
3-ICB #27	92236	2.00	0.4	800	105	none	4.38
3-ICB #27	10401	3.55	0.4	700	183	DI[b]	4.39
3-ICB #27	10506	3.00	0.5	700	163	DI[b]	4.40
3-ICB #20	103110	6.00	0.4	700	109	HF[c]	4.34
3-ICB #20	11362	5.00	0.4	500	222	HF[c]	4.29
3-ICB #20	11372	3.00	0.6	500	287	HF[c]	4.30
3-ICB #20	11380	3.00	0.4	300	187	HF[c]	4.31
3-ICB #20	11390	3.00	0.5	75	38	HF[c]	4.32
3-ICB #20	11718	3.00	0.4	700	48	HF[c]	4.33
3-ICB #20	112333	3.00	0.5	750	132	HF[c]	4.35
3-ICB #20	112521	1.80	0.5	750	---	HF[c]	4.46
3-ICB #20	112522	1.80	0.5	750	96	HF[c]	4.47
3-STM GE2	121310	3.50	0.5	750	159	HF[c]	4.42
3-STM GE2	121311	3.50	0.5	750	---	HF[c]	4.43
3-STM GE2	121319	3.50	0.5	750	---	HF[c]	4.45
3-STM GE2	121320	3.50	0.5	750	200	HF[c]	4.44
3-STM GE2	121601	3.50	0.5	750	397	HF[c]	4.37
3-STM GE2	121602	3.50	0.5	750	---	HF[c]	4.41

[a]VR = total vertical range of the imaged features.

[b]DI = de-ionized water rinse.

[c]HF = buffered hydrofluoric acid etch, de-ionized water rinse, immersion in methanol until loaded into vacuum system.

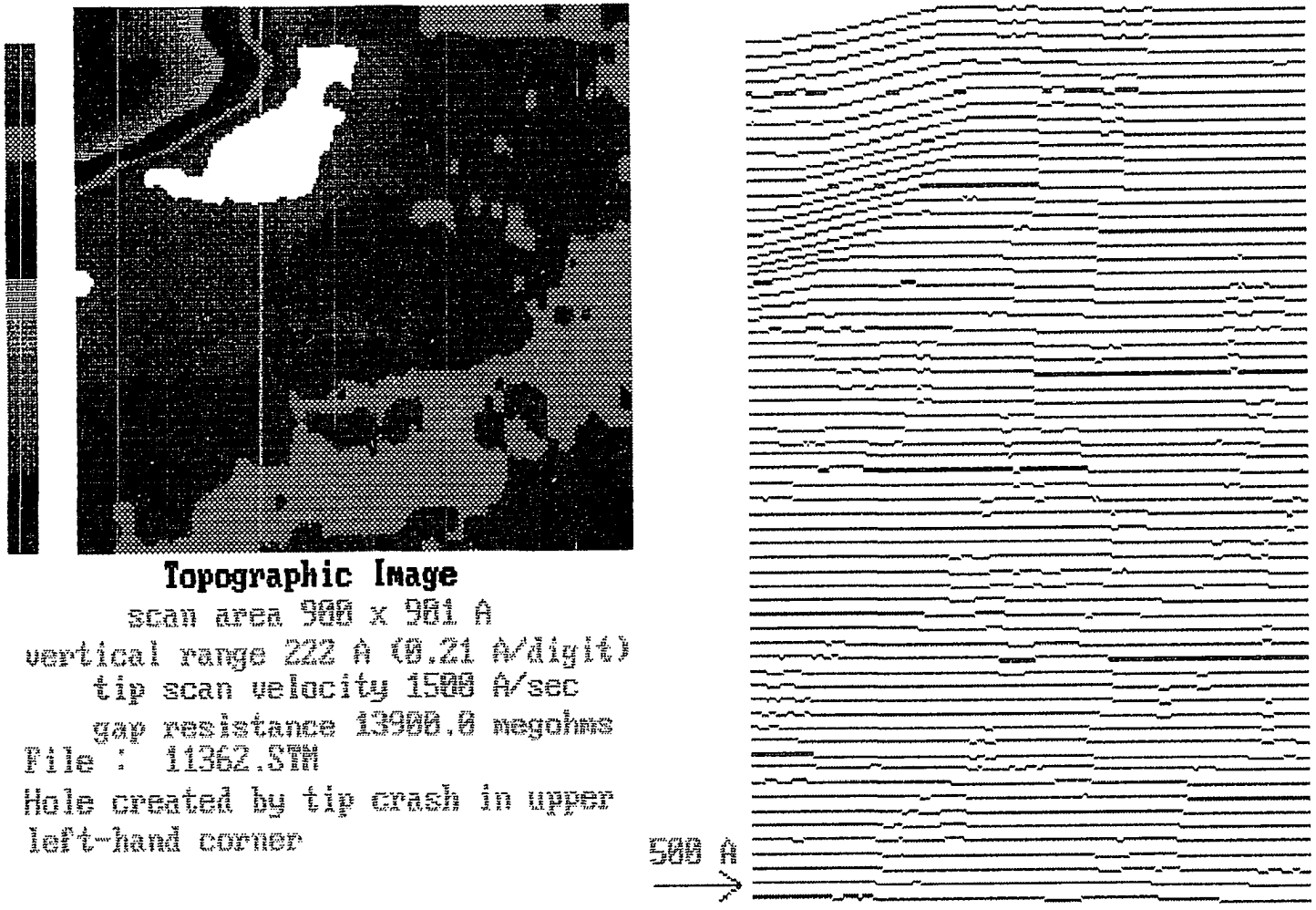

Figure 4.29. Constant current image of germanium showing one-fourth of a hole created by the tunnel tip crashing into the surface

Figure 4.30. Constant current image of germanium showing a close-up of the hole. The imprint of three mini-tips is visible, with the largest one having contributed the most to the tunnel current before it crashed. Rotating the image 90° clockwise produces an interesting effect

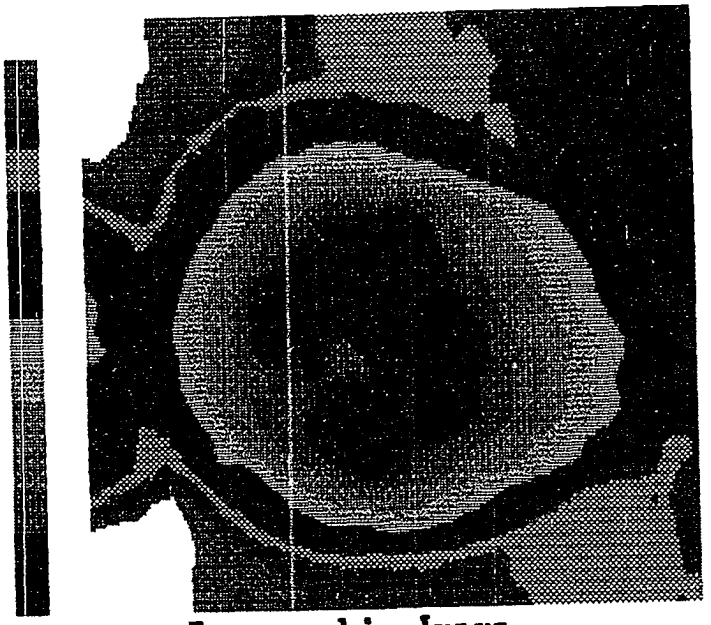

Topographic Image

scan area 502 x 500 Å
vertical range 287 Å (0.21 Å/digit)
tip scan velocity 1003 Å/sec
gap resistance 5452.7 megohms
File :
Close-up view of hole showing 2 small
and 1 large holes due to mini-tips

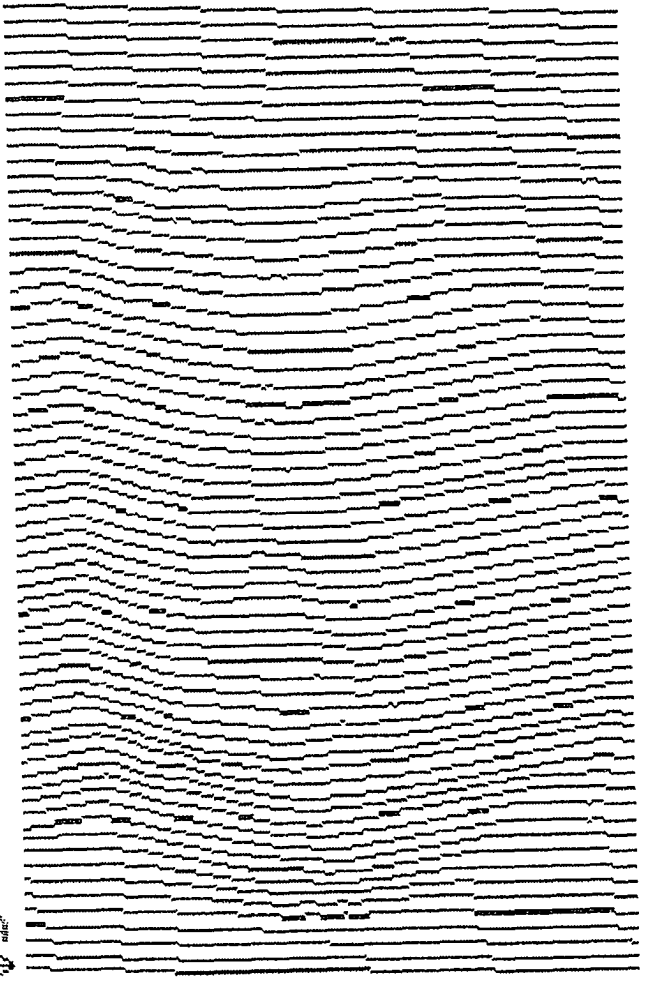

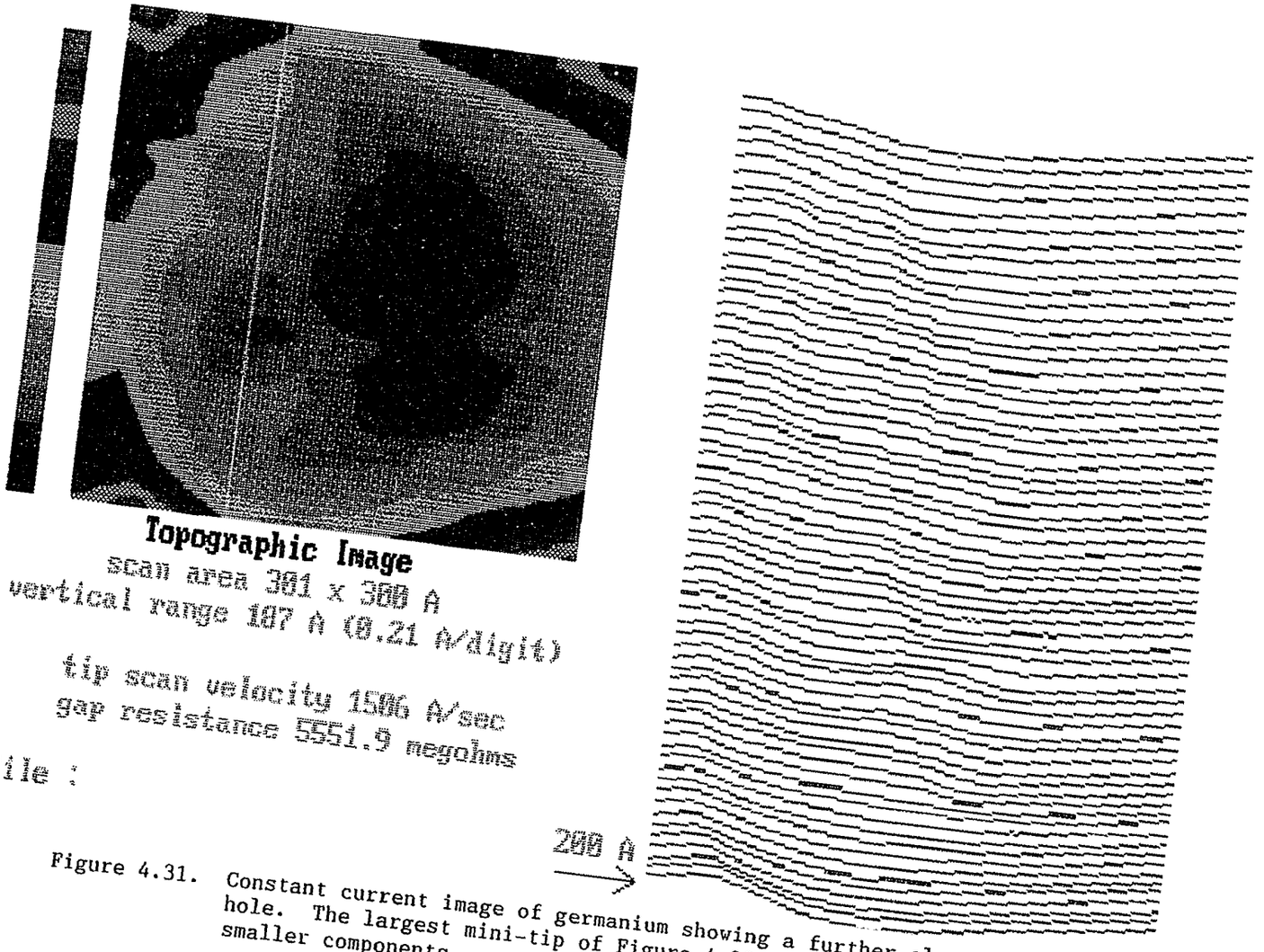

Figure 4.31. Constant current image of germanium showing a further close-up of the hole. The largest mini-tip of Figure 4.30 is now resolvable into smaller components

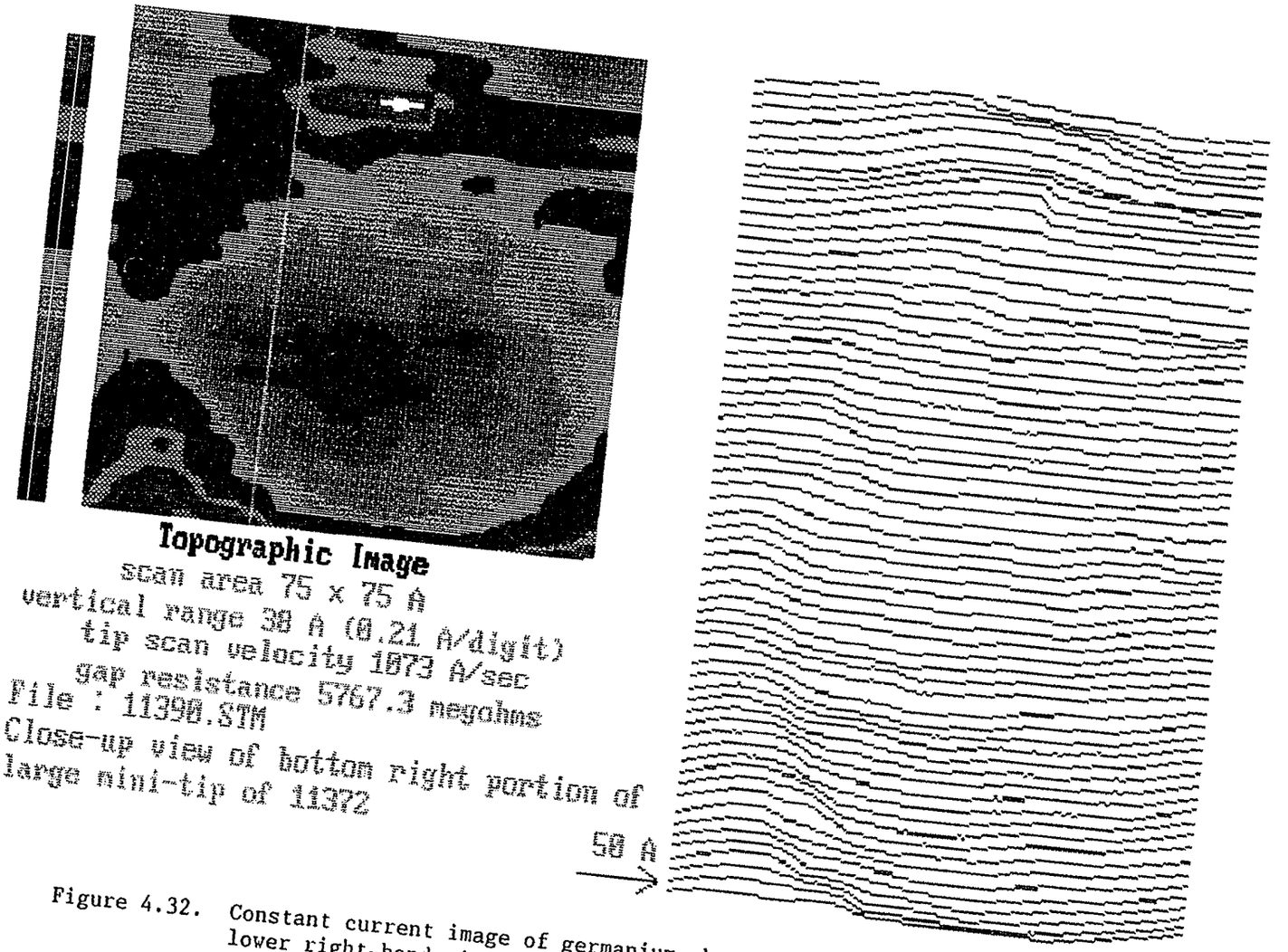

Figure 4.32. Constant current image of germanium showing further resolution of the lower right-hand mini-tip of Figure 4.30

By moving the tip location and reducing the scan size to 500 Å, more details in the hole are evident. Two features in Figure 4.30 yield information about the structure of the tip before it contacted the surface. The overall shape of the tip was a cone with a base diameter on the order of 350 Å, at a distance of more than 220 Å from the apex. In addition, the imprint of three mini-tips can be seen, with the largest mini-tip contributing the most to the current before its demise. Further reduction in the scan size resolves the mini-tips into smaller components, as can be seen in Figure 4.31. The lower right-hand mini-tip in Figure 4.31 is further resolved by an additional decrease in the scan size to 75 Å, as shown in Figure 4.32.

Attempts to image below 75 Å were unsuccessful because noise in the current signal increased to the point of obliterating useful information. The increase in noise was caused by either a change in tip shape or a commencement of tunneling from mini-tips, located along the sides of the tip, to the walls of the pit. Endeavors to create and then image subsequent holes were unsuccessful because of the poor tip quality after the second crash. Other demands on the STM forestalled further investigation into this method for possible use in direct-write-on-wafer lithography.

b. Surface features The motivation for examining ICB grown germanium was to obtain information about the mechanisms of film growth, and about the atomic scale structure of the film. Because of the limitations of the McAllister/RHK STM (refer to Section III.D), the films could not be examined in situ, and as a result, the films were exposed to

oxygen and other adsorbates during the transfer from the ICB system to the STM vacuum chamber. To minimize the effects of this contamination layer on imaging, the films had to be "cleaned" in a manner which would leave the top layers of germanium unaffected.

Conventional cleaning techniques (Ar^+ sputter etching, then annealing) could not be used because the top layers of the film, which contain information of interest, would be physically rearranged. Additionally, in some instances, the film was not thick enough, to withstand the bombardment of ions without some ions penetrating to the silicon substrate below. Two methods were determined to be non-destructive means of cleaning germanium surfaces and were subsequently employed.

Because germanium oxide is soluble in water, a de-ionized water (DI) rinse was used first. Images obtained with and without the DI rinse initially exhibited no difference in the quality of either signal or image, although a comparison of the two sets of images with the McAllister/RHK STM was difficult because of insufficient quantitative measures. One crude method employed, however, was the average vertical range (AVR) of the images, which was a very coarse indicator of surface roughness. Samples without the rinse exhibited an AVR of 165 ± 15 Å, while those that were rinsed had an AVR of 159 ± 8 Å, thus indicating no clear distinction between the two sets of images.

When the Nanoscope II became available for use, germanium films, both with and without the DI rinse, were once again compared. Optional software evaluates the average roughness of the entire image, and so is a

better measure of roughness than the AVR method. Films which were rinsed in DI water were repeatedly less rough than those without the rinse (refer to Section IV.D.2.a). This difference in roughness is predominantly due to the removal of loosely bound contaminants, but the removal and/or smoothing of the oxide layer may also be a factor.

A buffered hydrofluoric acid (HF) etch was also used to remove surface contamination, while at the same time, minimize the germanium oxide in a manner similar to the silicon studies of Feenstra and Oehrlein.[129] After a 15 sec HF etch, the sample was rinsed with DI water, blown dry with pure N_2, then immersed in methanol until the sample was ready to be loaded into the vacuum chamber. In this fashion, the oxide is believed to be thinner and more uniform than untreated films, which is supported by the reduction in the AVR for the HF treated films to 111 ± 8 Å, significantly lower than for the DI rinsed films obtained with the McAllister/RHK STM.

One problem with using HF to etch the surface, however, is the opportunity for the HF to etch the germanium. Exposure times were kept low to reduce the odds for damage, but it is possible that some of the features observed in Figures 4.33 and 4.34 were caused by the HF etch. Sample 11718 in Figure 4.33 was etched for 15 sec; sample 103110 in Figure 4.34 was etched first for 25 sec, then again for 20 sec, because the sample had been dropped onto the floor before immersion in the methanol. Both figures show a high frequency of small (on the order of 50 Å) holes, while the rest of the surface remains smooth. The image of 11718 is more detailed than 103110 because of the difference in tips

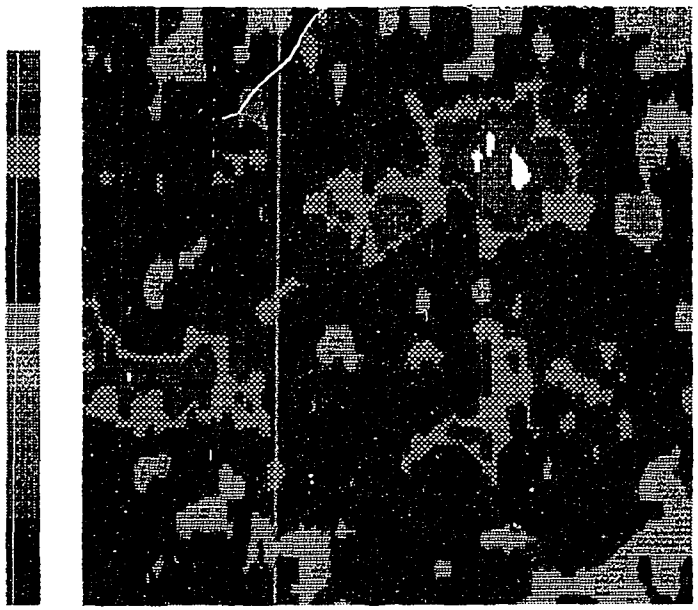

Topographic Image

scan area 700 x 701 Å
vertical range 48 Å (0.21 Å/digit)
tip scan velocity 1400 Å/sec
gap resistance 7510.0 megohms

File : 11718.STM
15 sec HF etch on germanium film

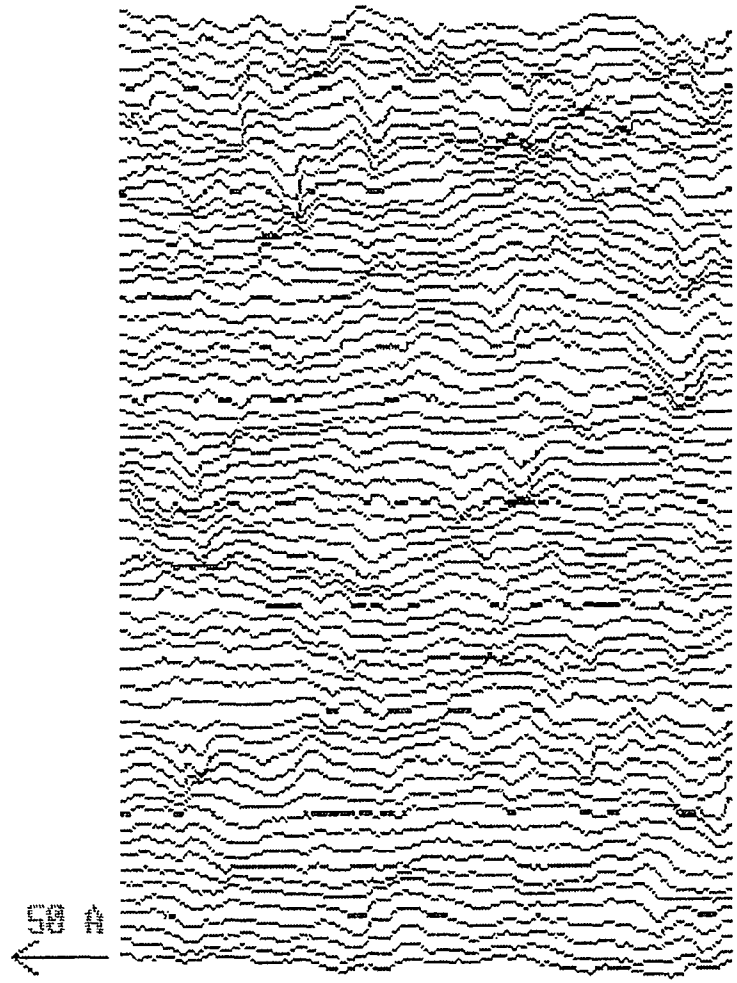

Figure 4.33. Constant current image of germanium cleaned using a buffered hydrofluoric acid (HF) etch for 15 sec. The small holes are approximately 30 Å in diameter

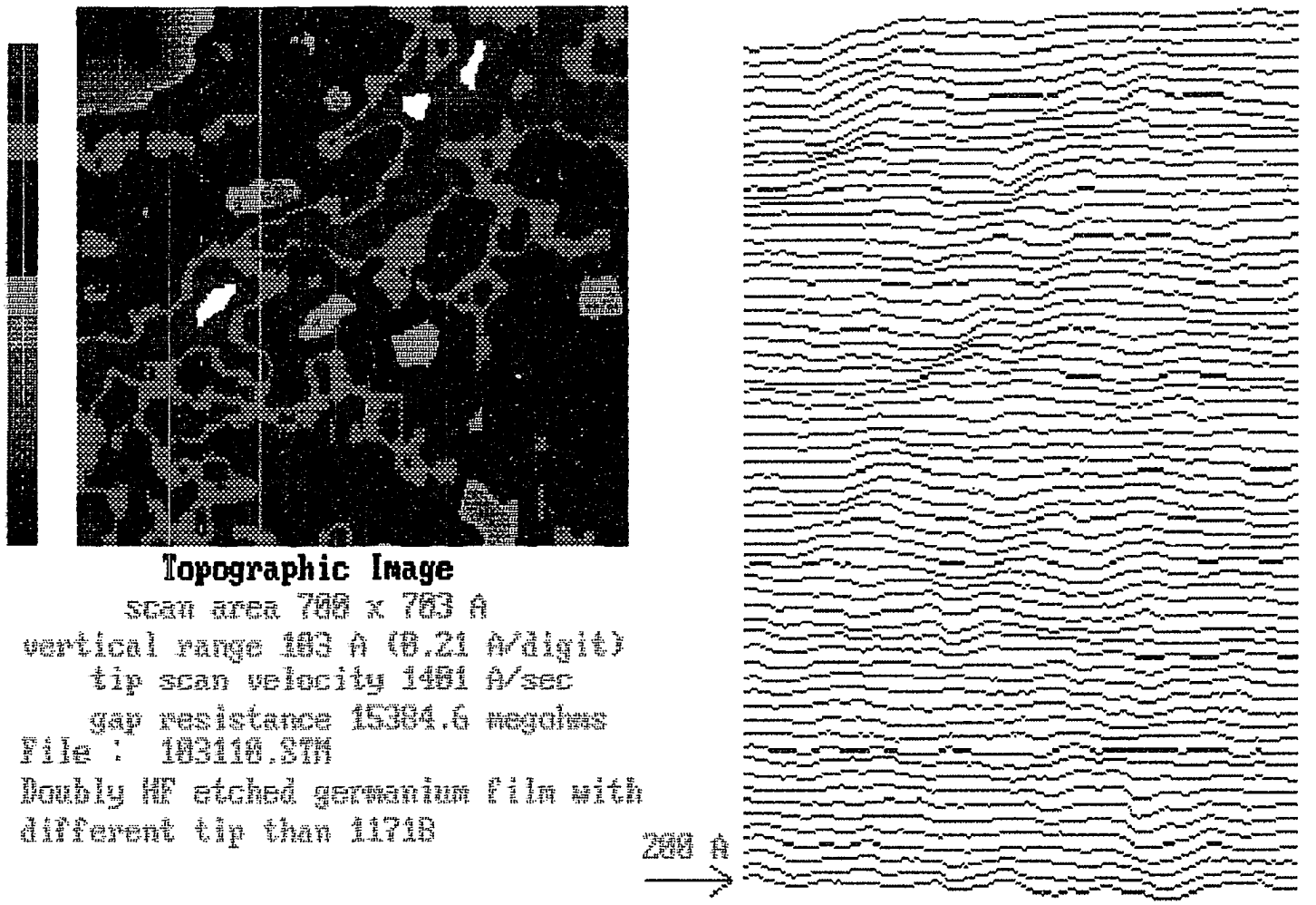

Figure 4.34. Constant current image of germanium cleaned using a buffered hydrofluoric acid (HF) etch twice (first for 25 sec, then for an additional 20 sec). The small holes are approximately 50 Å in diameter

between the two scans. The shift in right versus left (R/L shift) scan direction images for each tip indicated the existence of mini-tips, which were spaced approximately 10 Å for 11718 and approximately 45 Å for 103110. The smaller mini-tip spacing in 11718 allowed the tip to probe deeper into the holes than for 103110.

Despite the appearance of the small pits in Figures 4.33 and 4.34, the HF etch format was continued because of the overall improvement in the quality of the current signal and tunnel images, as compared to the as-is or DI rinsed samples. For etch times less than one minute, there was no corresponding increase in the number of pits with an increase in HF exposure. Additionally, only a small percentage of the total number of images showed signs of the pits, thus enforcing the view that, in this situation, the HF etch does little damage to the germanium.

Once the cleaning method was standardized, the occurrence of diverse surface features was examined for various germanium films. The features can be placed into three main categories: islands, ridges and holes. Individual islands, similar to those shown in Figure 4.35, ranged from approximately 130 to 400 Å in diameter. Islands larger than 400 Å were often linked to other islands or ridges, as shown in Figure 4.36. Ridges, which could alternately be described as long, skinny islands, also appeared as stand-only features, as in Figure 4.37, or as dividers between holes, as in Figure 4.38. Widths of the ridges ranged from roughly 125 to 200 Å, while the lengths ranged from approximately 200 Å to greater than 700 Å.

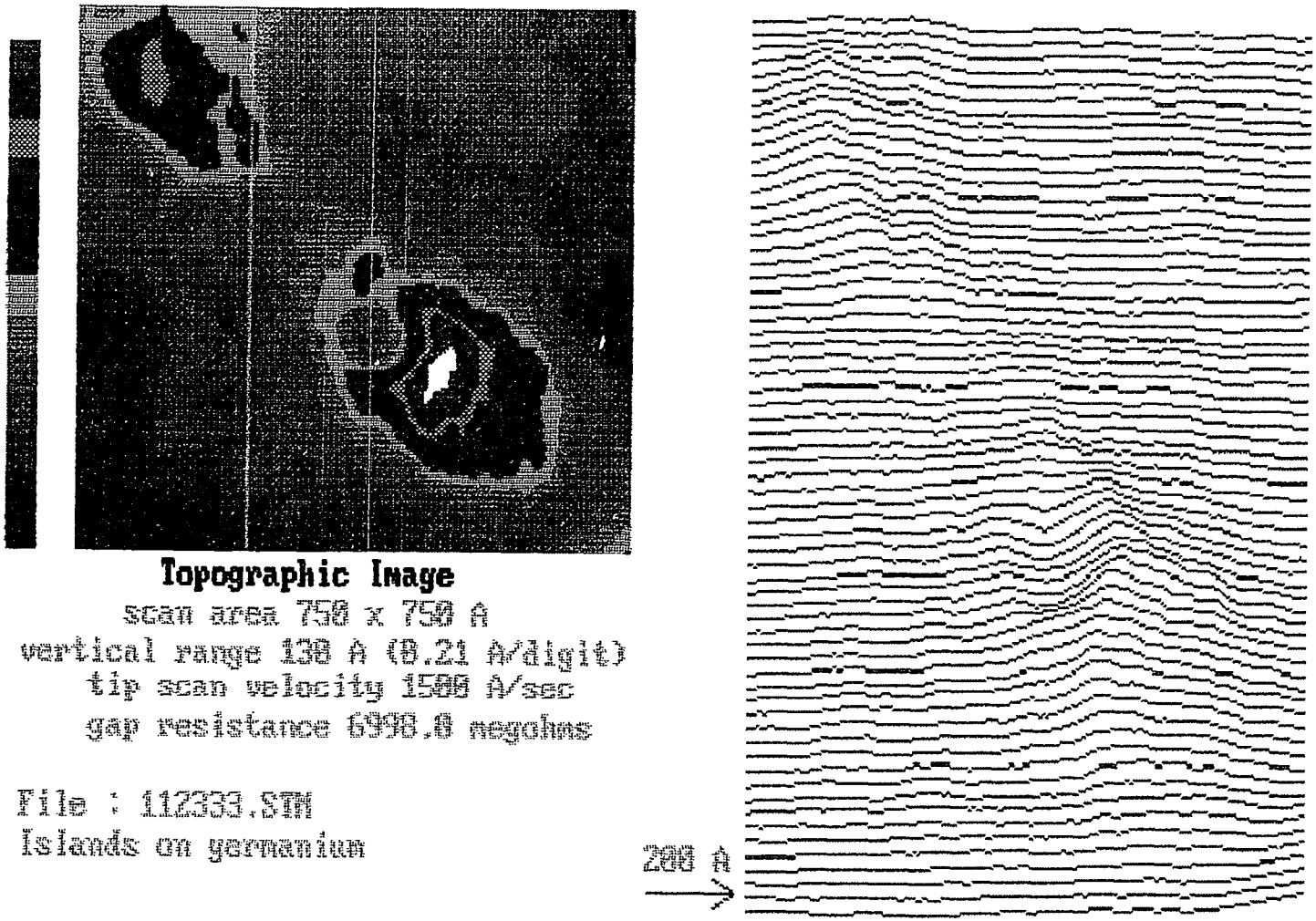

Figure 4.35. Individual islands of germanium imaged in the constant current mode

Figure 4.36. Germanium islands interconnected by a ridge, imaged in the constant current mode. The top part of the figure is an island approximately 470 Å in diameter, and the bottom island (not visible) is approximately 250 Å in diameter

Topographic Image

scan area 549 x 549 A
vertical range 89 A (0.21 A/digit)
tip scan velocity 1372 A/sec
gap resistance 0750.0 megohms
File : 9939.STM
Ridge connecting two islands at top and botton of image

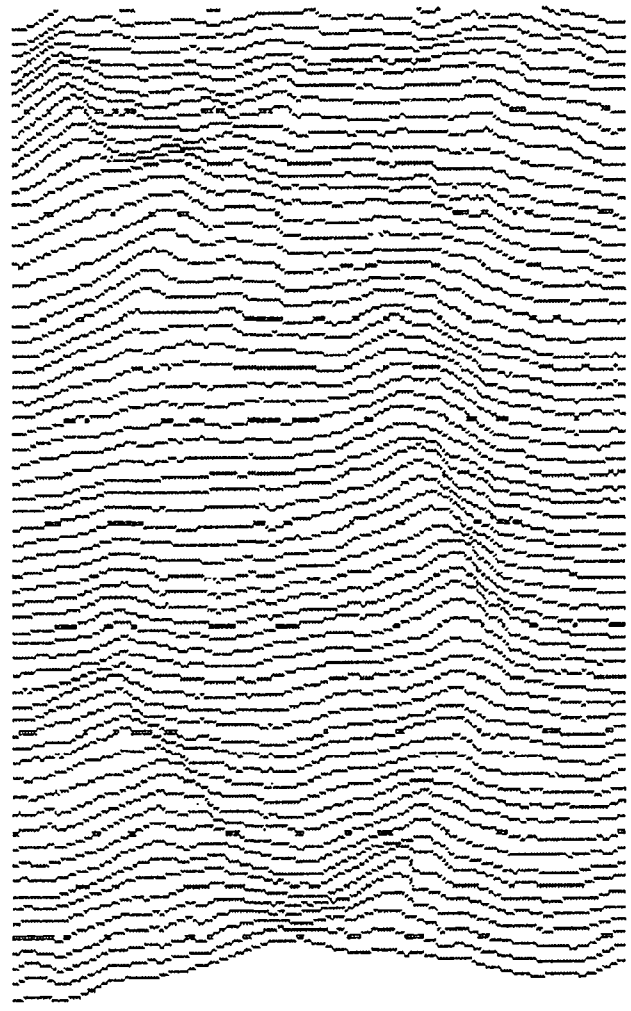

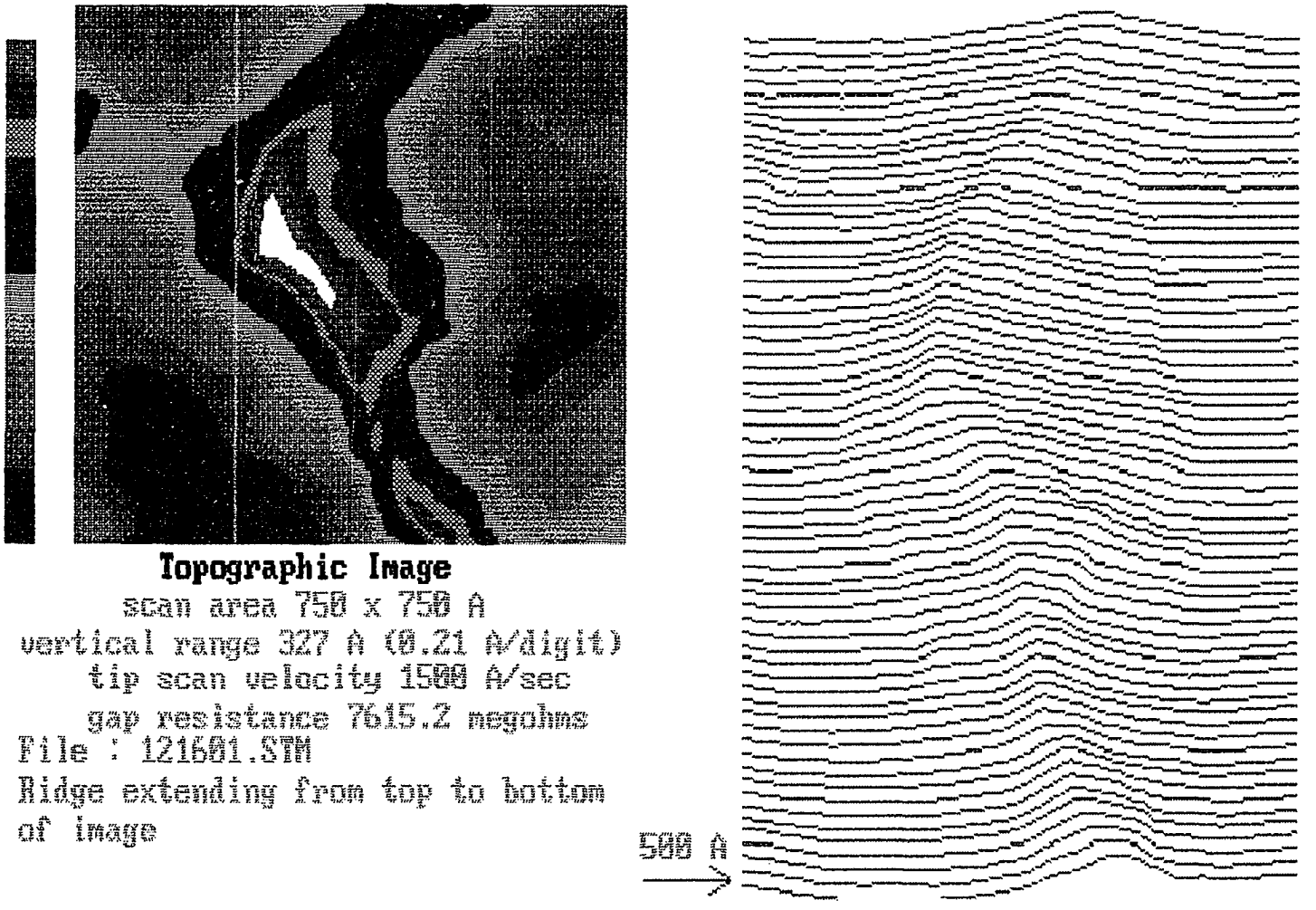

Figure 4.37. 300 Å wide, 750+ Å long ridge on germanium, imaged in the constant current mode. For this sample, the vertical range (in this instance, 327 Å) often exceeded the film thickness (100 Å)

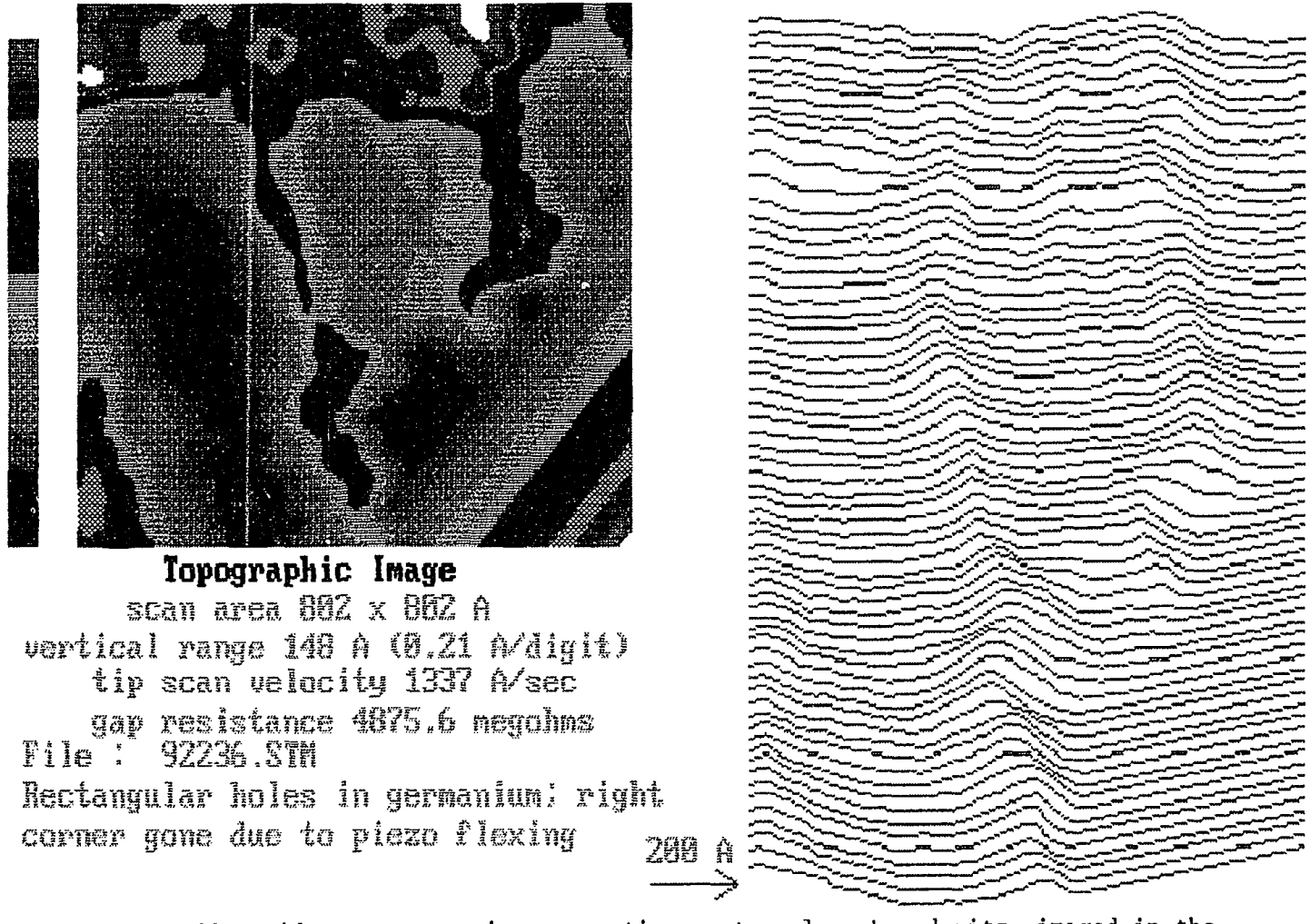

Figure 4.38. Ridges on germanium separating rectangular shaped pits, imaged in the constant current mode. The right-hand corner is an example of the Z-piezo not compensating for the large scan flex in the X and Y piezos

Holes tended to be the most varied group in terms of size, ranging from 50 to 500 Å in diameter, and in shape, as shown in Figure 4.38. Most of the holes were circular, but often they were rectangular, with no correspondence with the orientation of the underlying silicon substrate. For some of the images, the rectangular shape was caused by large scan piezoelectric transducer distortion, as discussed in Section III.A.2. If the Z-piezo is extended close to its maximum length to be in tunneling range, then the Z-piezo cannot compensate, with further expansion, for the large scan flex in the X and Y piezos. The resulting images contain an artificial slope, with the lower right-hand corner (the furthermost point in the scan) registering off scale, as can be seen by the evenly spaced color bars in Figure 4.38. The slope processing feature is unable to compensate for the off scale behavior, and this can introduce an artificial elongation of certain features. Operating at smaller scan sizes and moving the tip as close as possible to the surface, without crashing, during the mechanical approach, are two methods to reduce this problem.

Most of the images were very similar in terms of the amount and the diversity of features, except for the few instances when all three classes of features appeared in the same scan, as shown in Figures 4.39 and 4.40. It was difficult to draw any conclusions as to the frequency of one feature versus another, especially with respect to film growth. Three thicknesses of film were examined (100, 400 and 3000 Å), but no correlation between thickness and surface feature class or size could be determined.

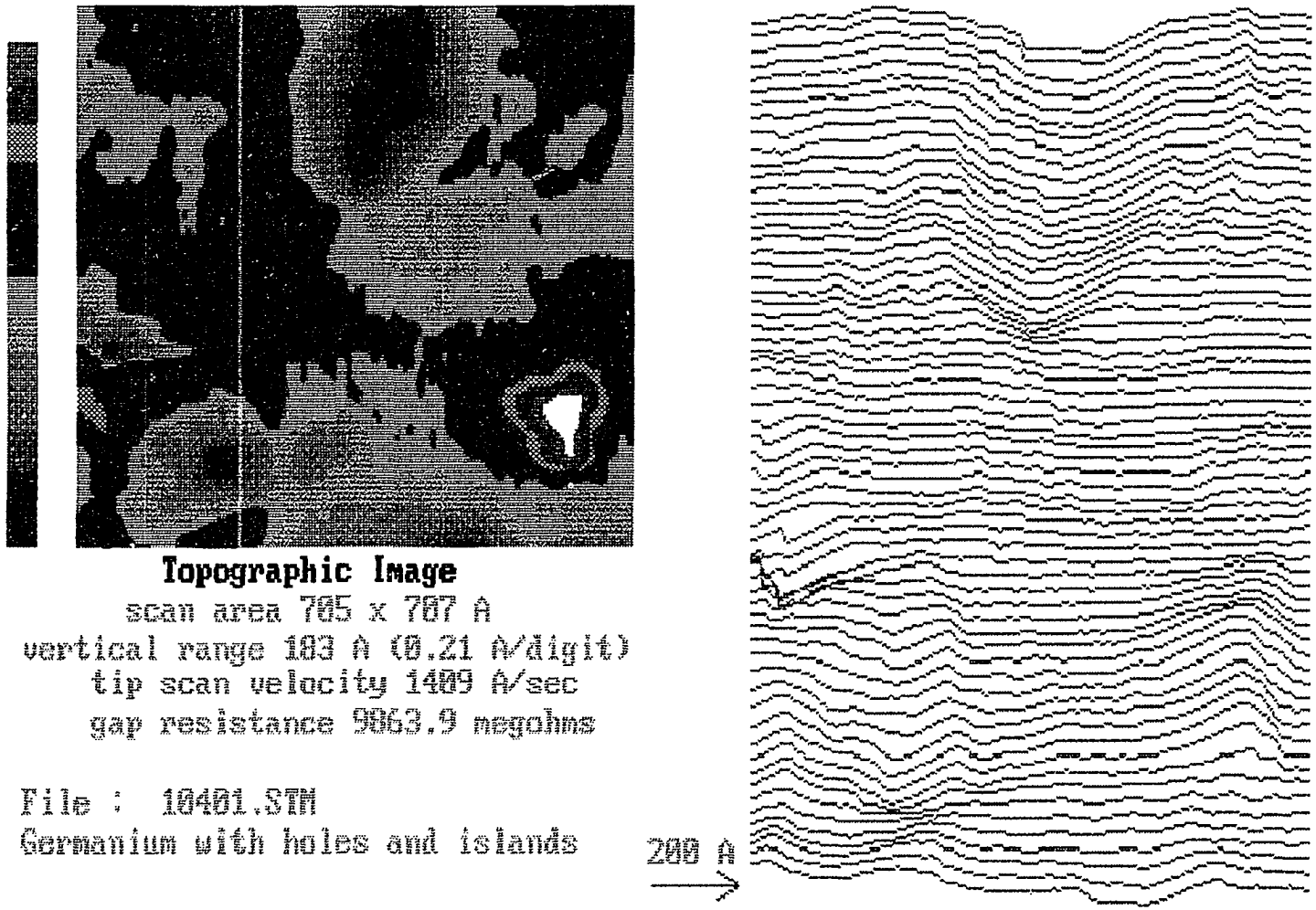

Figure 4.39. Constant current image of germanium showing holes, islands and ridges

Topographic Image

scan area 705 x 707 A
vertical range 179 A (0.21 A/digit)
tip scan velocity 1409 A/sec
gap resistance 6132.7 megohms

File : 10506.STM
Active area on germanium surface

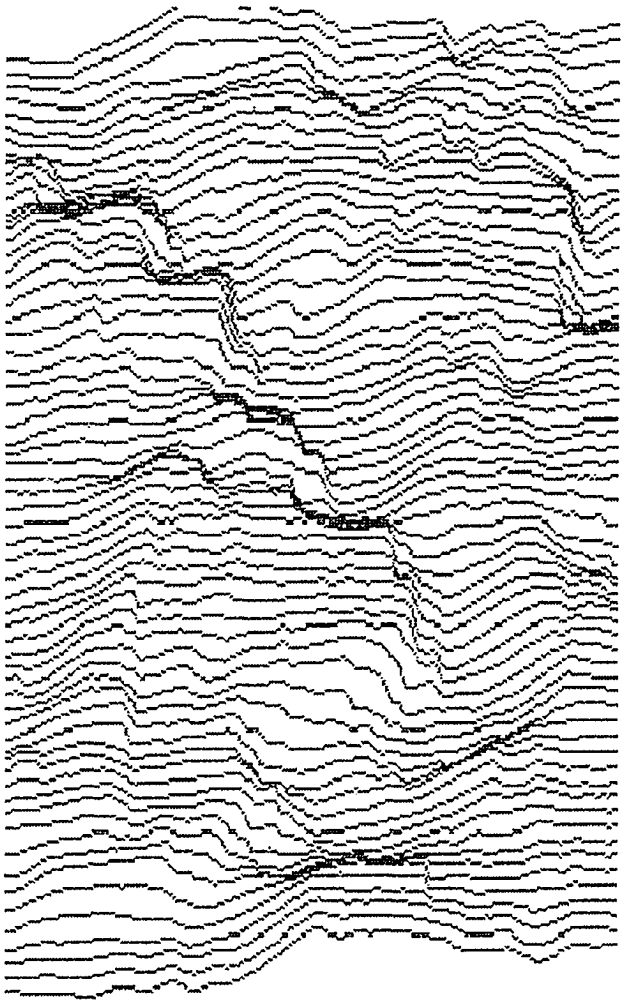

Figure 4.40. Constant current image of germanium showing a variety of surface features

However, one interesting aspect of the images did emerge. For the STM GE2 group of images, the vertical range of the image often exceeded the film thickness, as shown in Figure 4.37. For this image, the vertical range was 327 Å, as compared to the approximate 100 Å film thickness (as determined by a quartz crystal film monitor and by the time at the ICB deposition rate). The AVR for the STM GE2 images was 266 ± 71 Å, which is significantly higher than for the thicker films.

The discrepancy between the two distances can be explained in terms of the basic expression for one-dimensional tunneling given by Equation 1.1,

$$I \propto V \exp(-2\kappa d) \qquad (1.1)$$

(refer to Sections I.C and II.B). The current depends exponentially, not only on distance, but on the behavior of the potential barrier, which depends on the chemical identities of both the tip and the surface. When the surface composition alters, the tunnel current registers a change which cannot be distinguished from a change in distance. The sizable vertical ranges observed are most likely caused by a change in the chemical composition from germanium to germanium-oxide regions, and hence, not representative of surface topography. This change in composition was investigated by the barrier height method discussed below.

c. Barrier height results The voltage to the Z-piezo was modulated with a 5 kHz, 40 mV_{pp} input, and the resulting scans were imaged in the Auxiliary Mode of the STiMage 1.3 program. The barrier

height image of the ridge in Figure 4.37 is shown in Figure 4.41, where the less noisy regions of the line scans in Figure 4.41 correspond with the ridge, and the areas of greatest signal change correspond with the lower (blue) portions of Figure 4.37. The dramatic variation in the line scan character from the ridge to the low-lying regions indicates a significant change in the potential barrier, which is caused by a difference in the local work functions.

Because germanium oxide is not tightly bound to the germanium film, the oxide appears to migrate toward valleys in the film. Therefore, the current signal increase in the valley regions denotes the valleys as germanium oxide and the ridge as germanium. The behavior of the current signal in the topographic high and low areas is seen repeatedly, as depicted in Figures 4.42 through 4.45. In both sets of images, the holes are clearly indicated by the large fluctuations in the line scans. Thus, we have shown that the barrier height technique can be used to locate the oxide rich areas by mapping the transition from smooth to noisy signals.

Before this technique can be used reliably, two concerns need to be addressed: the significance of the dissimilarity between Figures 4.46 and 4.47; and the quantitative difference between the smooth and noisy regions of the line scans, and the correlation with work function differences between germanium and germanium oxide. The barrier height image of Figures 4.46, displays regions of high activity in the line scans that do not concur with the low-lying regions in the corresponding topographic image (refer to Figure 4.47). This variation in the barrier height images is probably caused by changes in the potential barrier, as

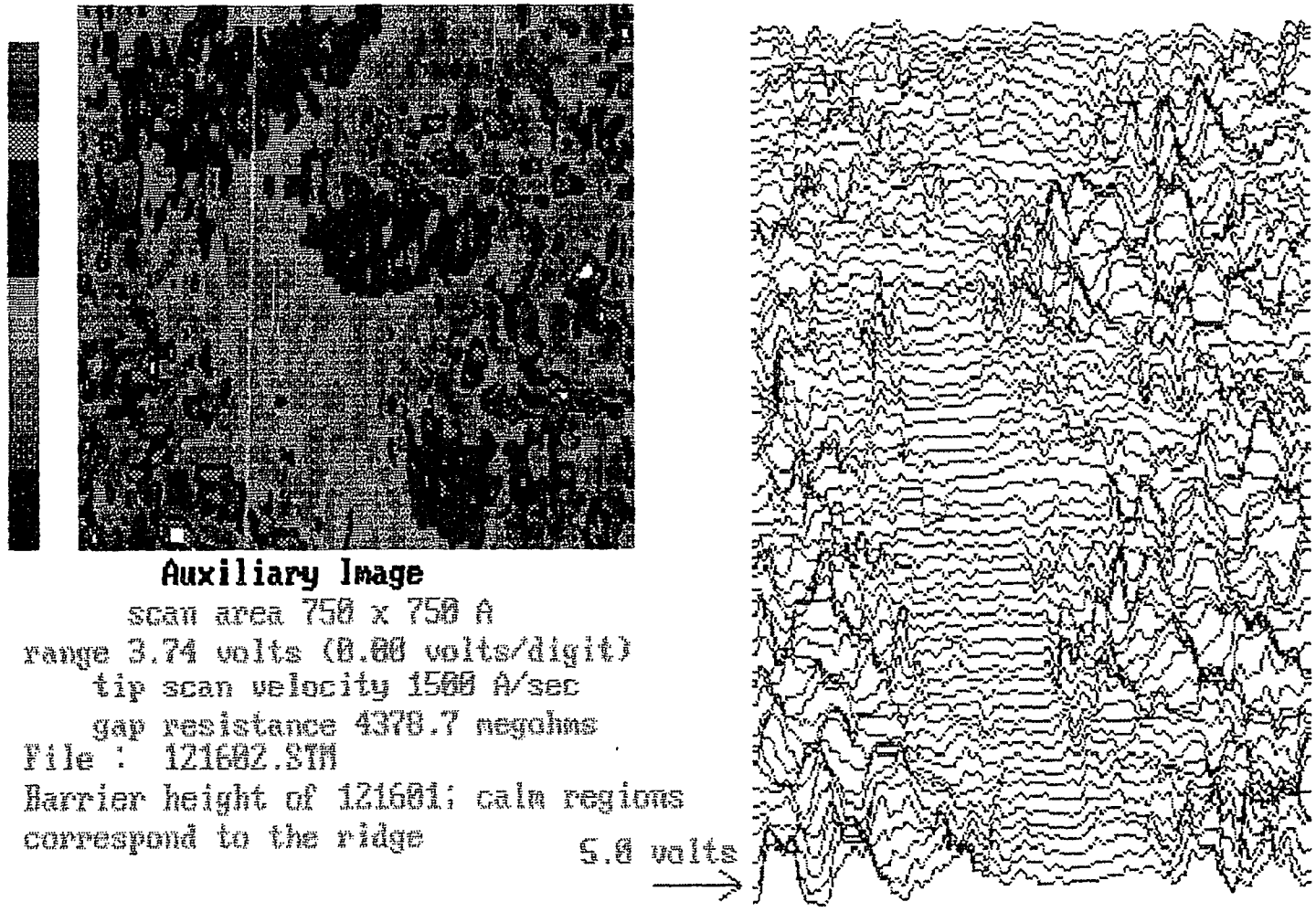

Figure 4.41. Barrier height image of the germanium ridge of Figure 4.37. Notice the decrease in line scan activity in the vicinity of the ridge

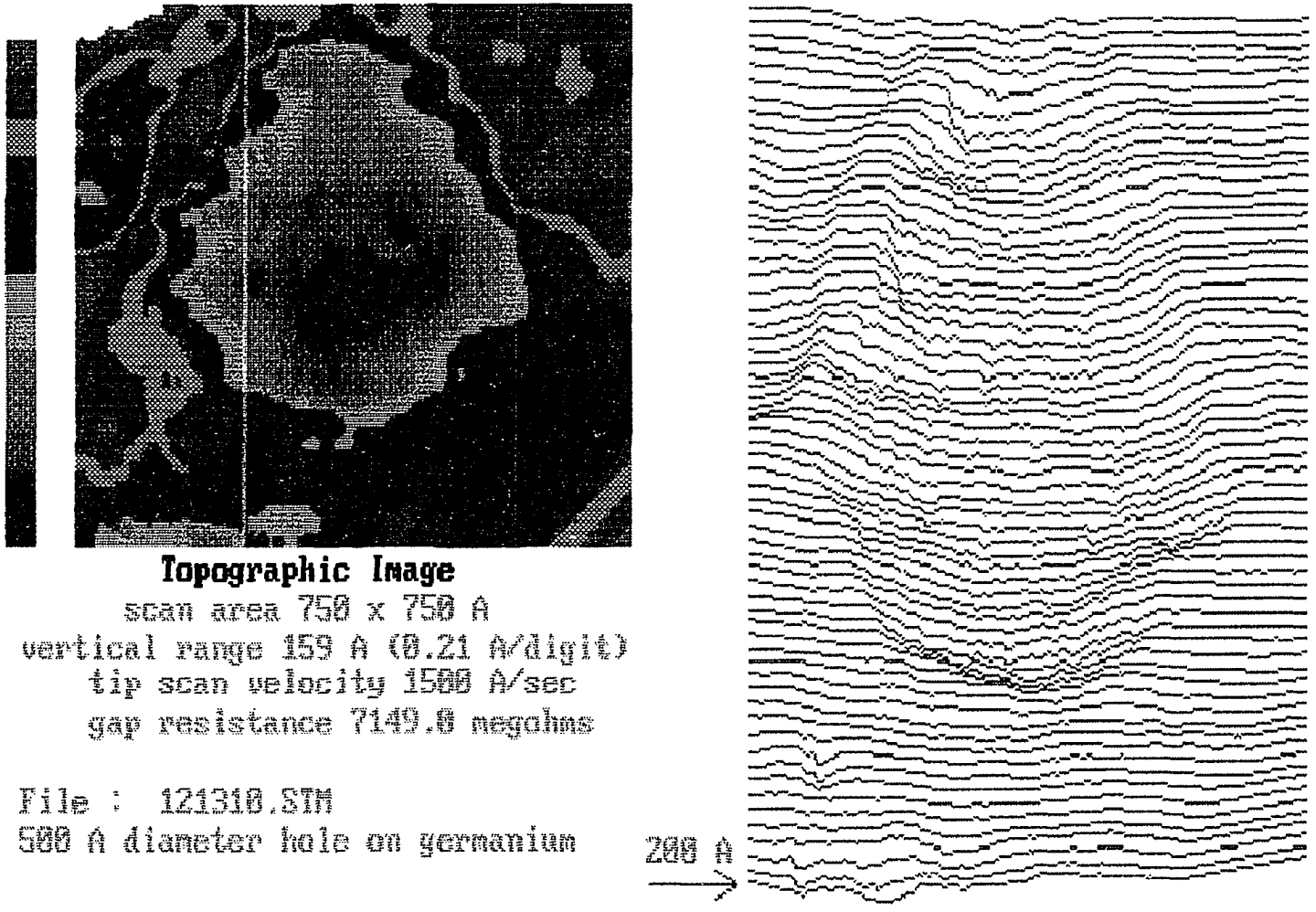

Figure 4.42. Topographic image of germanium

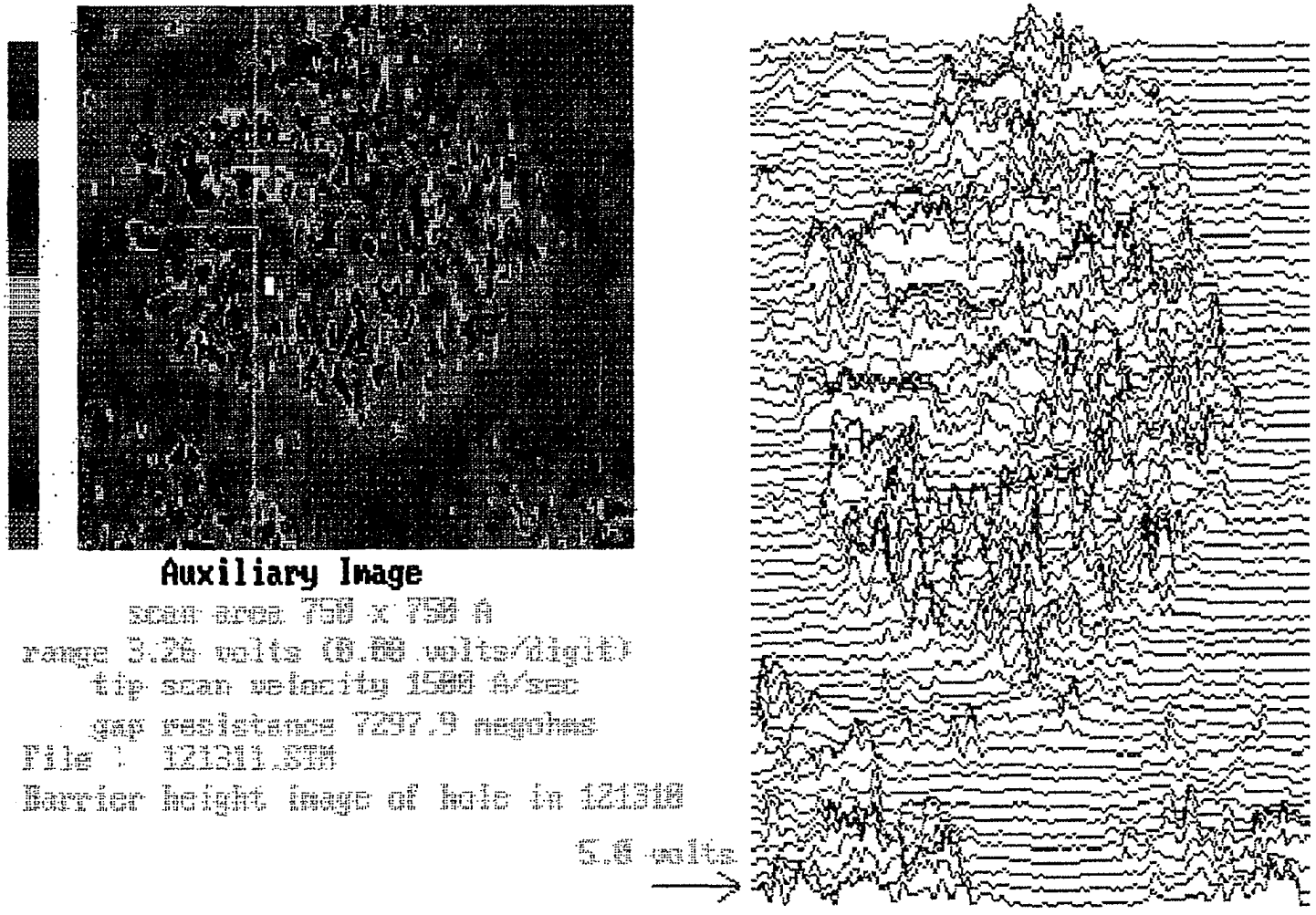

Figure 4.43. Barrier height image of Figure 4.42 showing high line scan activity in the low (blue) regions indicating a change in work function between the high (red) and low (blue) regions

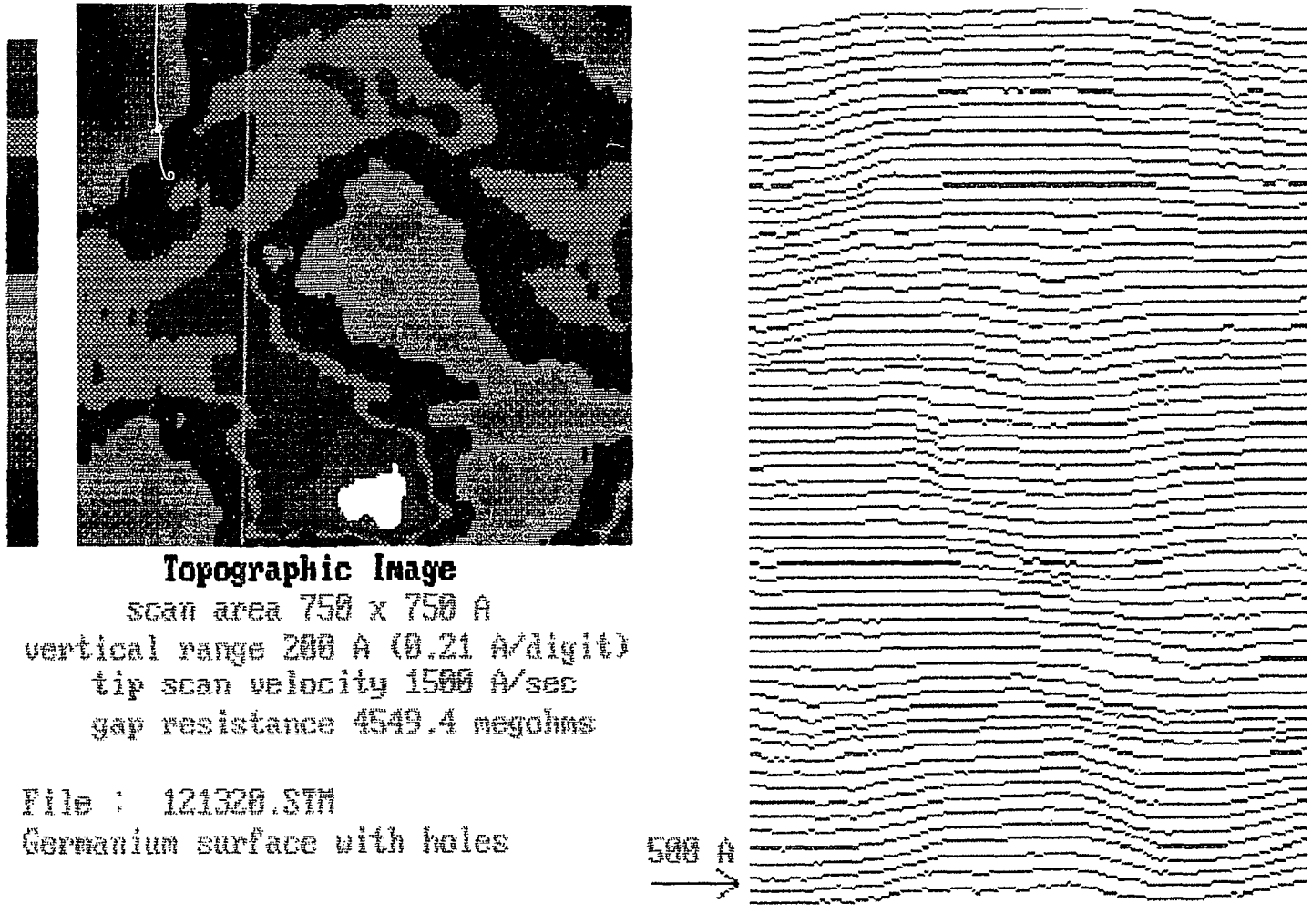

Figure 4.44. Topographic image of a 500 Å hole on germanium

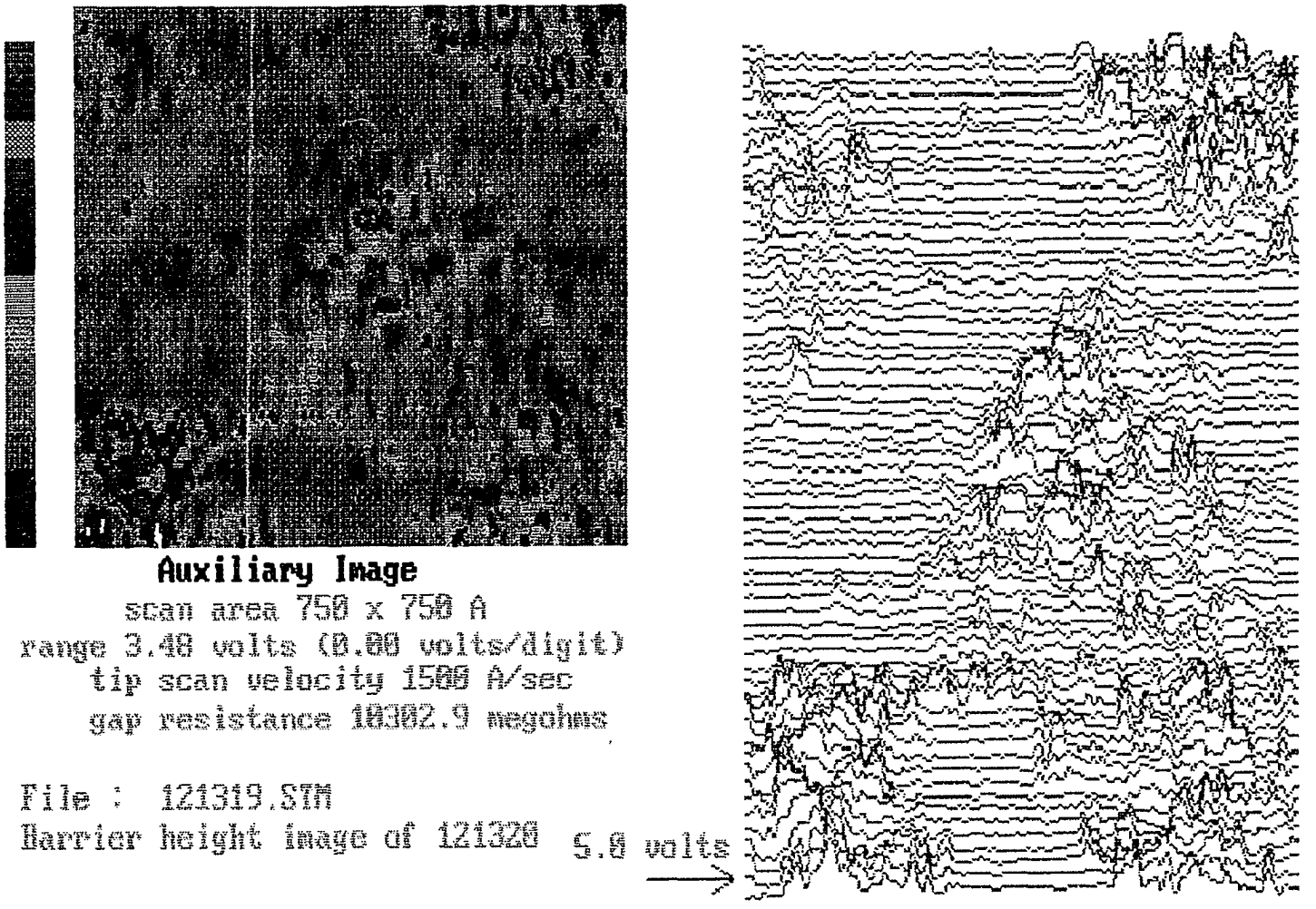

Figure 4.45. Barrier height image of Figure 4.44 showing increased line scan activity in the same area as the hole in Figure 4.44

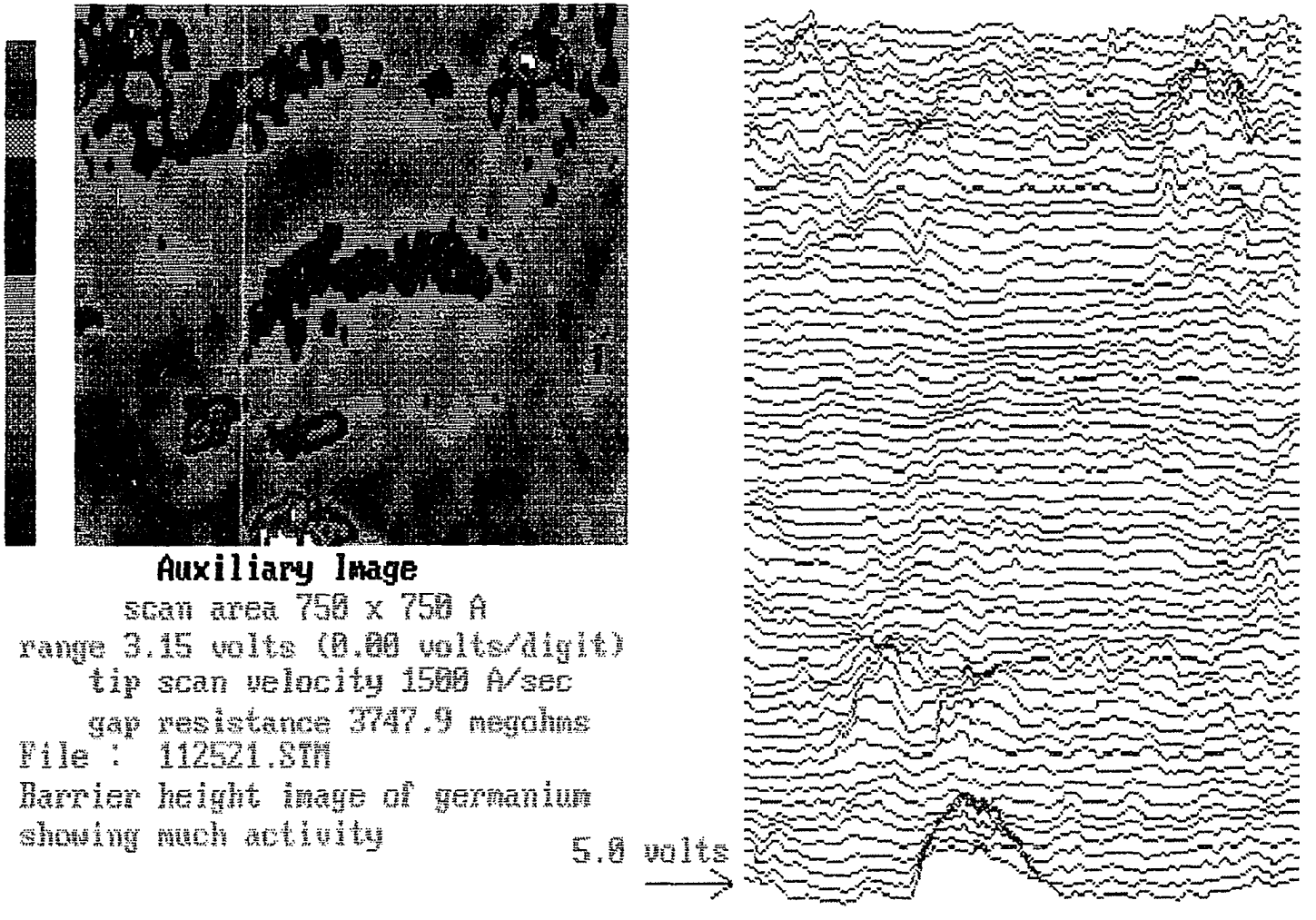

Figure 4.46. Barrier height image of germanium showing activity at the top and at the lower left of the image

Figure 4.47. Topographic image of Figure 4.46 showing far fewer features than indicated by the barrier height scan. The discrepancy between the two images may be attributable to differences in work functions due to contaminants other than germanium oxide

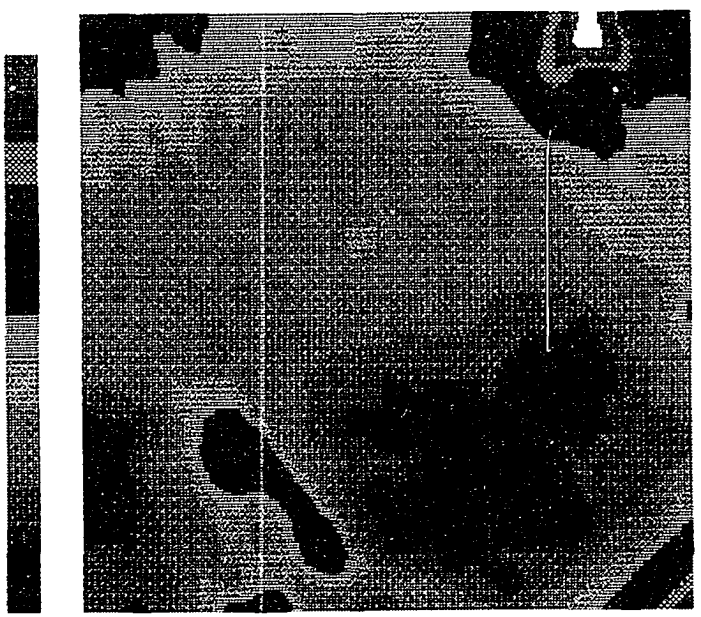

Topographic Image

scan area 750 x 750 Å
vertical range 88 Å (0.21 Å/digit)
tip scan velocity 1500 Å/sec
gap resistance 3394.3 megohms
File : 112522.STM
Topo of 112521 showing little similarity in features

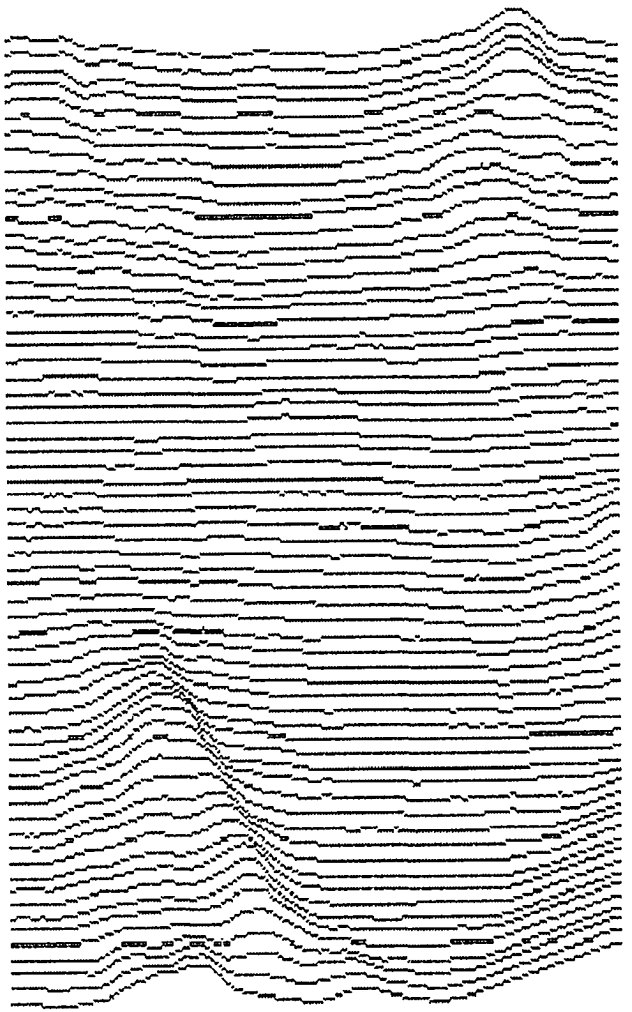

a result of either the presence of other contaminants beside germanium oxide, or from other changes in the LDOS.

An attempt was made to address the above concerns by performing more barrier height measurements with the intention of obtaining quantitative information about the variation of the line scans. Unfortunately, while calibrating the system, the STM developed noise in the current signal, which could not be corrected. Further studies on germanium were performed with the Nanoscope II, made by Digital Instruments. While the Nanoscope II has the capability of obtaining barrier height results, the method is used as a qualitative, not quantitative, means of examining the surface. Until the alternative methods become available, the barrier height issues raised here will remain unanswered.

2. Nanoscope II Results

The Digital Nanoscope II is a Scanning Tunnel Microscope which was designed for larger scan areas than the McAllister/RHK package (5500 Å versus 1000 Å scan sizes). Instead of the tripod arrangement, a piezoelectric tube scanner provides the orthogonal tip motion, which allows for higher scan speeds, less piezoelectric drift, and fewer symmetry problems in the lateral directions. The main drawbacks of the Nanoscope II are the constraint of operating only in air, and the smaller z-range of motion (100 Å versus 1500 Å). These drawbacks reduce the resolution to tens of nanometers instead of angstroms, and reintroduce the effects of contaminants on the images.

However, the initial work on germanium with the McAllister/RHK STM raised many questions, especially in terms of large area effects, which include many aspects of ICB film growth. Cluster size (50 to 100 Å), the amount of cluster spreading upon impact, and details of island formation require a larger field of view than is currently available with the McAllister/RHK system, but which is well suited for the Nanoscope II.

Sample cleaning, as well as the effect of annealing, and film growth, was examined, with the tunneling conditions for the images presented in this section, listed in Table 4.4.

a. Sample cleaning As discussed in Sections IV.C.1.b and c, the effect of germanium oxide and other contaminants is an important concern when interpreting the STM images, especially when imaging in air. To re-examine the effects of cleaning, untampered germanium films were compared with films which had surface dust removed by a compressed gas duster and with films rinsed with de-ionized water (DI). The comparisons were made visually and by using the roughness option of the Nanoscope II, which measures the average displacement of the Z-piezo for an image.

The images of dusted films appeared to contain more surface features, with more distinct boundaries, than the untampered films. The average roughness increased slightly from 3.42 ± .71, for the dusted films, to 3.56 ± .92 nm without dusting, which is well within the statistical variation of the groups. However, the increased roughness could be attributed to the debris impacting with the surface as it was blown away. Because the roughness difference was small, samples were either dusted to minimize the odds of encountering dust particles when

Table 4.4. Tunneling conditions and cleaning methods for germanium samples imaged with the Digital Nanoscope II

Sample	File	Cleaning Method	V_B[a] (mV)	I[b] (nA)	Scan Size (nm)	Figure Number
3-ICB #53	53GE.001	none	199.9	1.0	500	4.50.a
3-ICB #53	2-53GE.002	none	100.1	1.1	500	4.50.b
3-ICB #53	4-53GE.001	DI[c]	80.0	1.0	500	4.49.b
3-ICB #59	59GE.004	none	29.9	1.6	550	4.48.a
3-ICB #59	4-59GE.011	DI[c]	-29.9	1.6	550	4.48.c
3-ICB #59	5-59GE.014	PD[d]	29.9	2.0	50	4.54
3-ICB #59	6-59GE.001	PD[d]	29.9	2.0	550	4.48.b
3-ICB #59	8-59GE.003	DI[c]	-29.9	2.0	550	4.48.d
3-ICB #59	9-59GE.024*	DI[c]	29.9	2.0	100	4.52
3-ICB #59	9-59GE.027*	DI[c]	29.9	2.0	50	4.55
3-ICB #62	2-62GE.002	none	-29.9	2.0	450	4.56.a
3-ICB #62	3-62GE.001	none	29.9	2.0	250	4.57
STM GE2	GE2.001	none	-29.9	2.0	550	4.58

[a] V_B = sample bias voltage.

[b] I = tunnel current set point.

[c] DI = de-ionized water rinse.

[d] PD = pressurized duster used to remove surface dust.

*Samples were imaged 5 hours after rinse.

scanning the surface, or rinsed with DI.

The rinsed samples exhibited sizable alterations in both the visual and roughness comparisons with the untampered films, as shown in Figure 4.48. The figure displays two different scan locations for the untampered films (Figures 4.48.a and b) and for the rinsed films (Figures 4.48.c and d). The surface features for the rinsed films are smoother and have larger regions which show little surface activity, which was also reflected by the reduction in roughness measurements to 3.22 ± .68 nm. The reduction in roughness can be attributed to the removal of surface debris in a manner which is less damaging to the surface than dusting. There was also some indication of the time-dependence of the contamination layer when a portion of the film was DI rinsed and then imaged 5 hours later, with the average roughness (3.31 ± .74 nm) falling in between the untampered and rinsed values.

Germanium samples, other than 3-ICB #59, showed a similar reduction in the visual and measured roughness of the films of germanium as compared to the untampered films. The majority of films examined after 3-ICB #59, were rinsed with DI to minimize the amount of surface contaminants.

b. Annealing effects A portion of sample 3-ICB #53 was annealed at 700°C for 15 minutes, and the resulting Nanoscope II images were examined for any differences with respect to the non-annealed portion. A Scanning Electron Microscope (SEM) image (as shown in Figure 4.49.a) of the non-annealed portion indicated the existence of small balls of germanium, ranging from 90 to 1400 nm in diameter, with flat terrain in

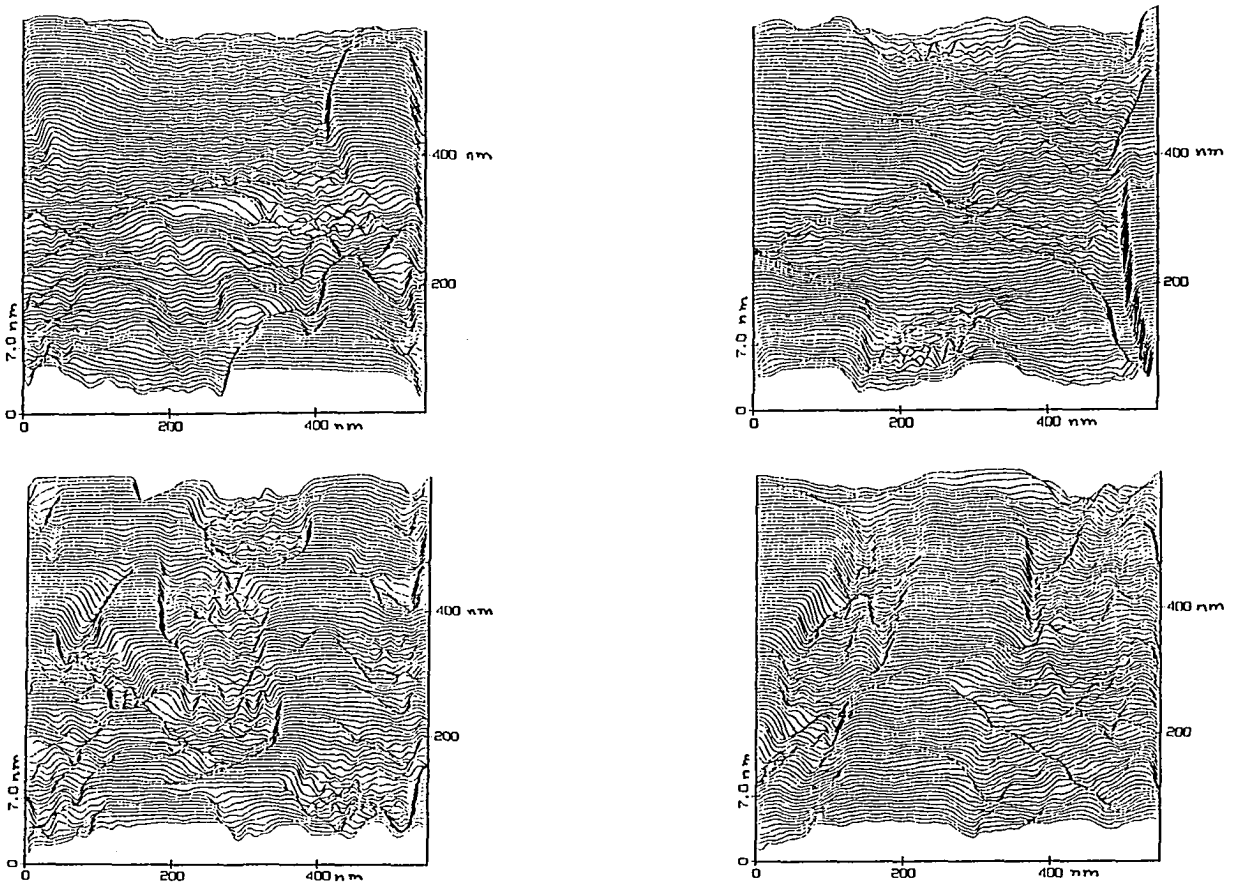

Figure 4.48. Constant current images of germanium showing the effects of a deionized water rinse to clean the surface. a) and b) image two different portions of the untampered sample. c) and d) image two different portions of the rinsed sample. The rinsed images appear to be more smooth than the untampered images

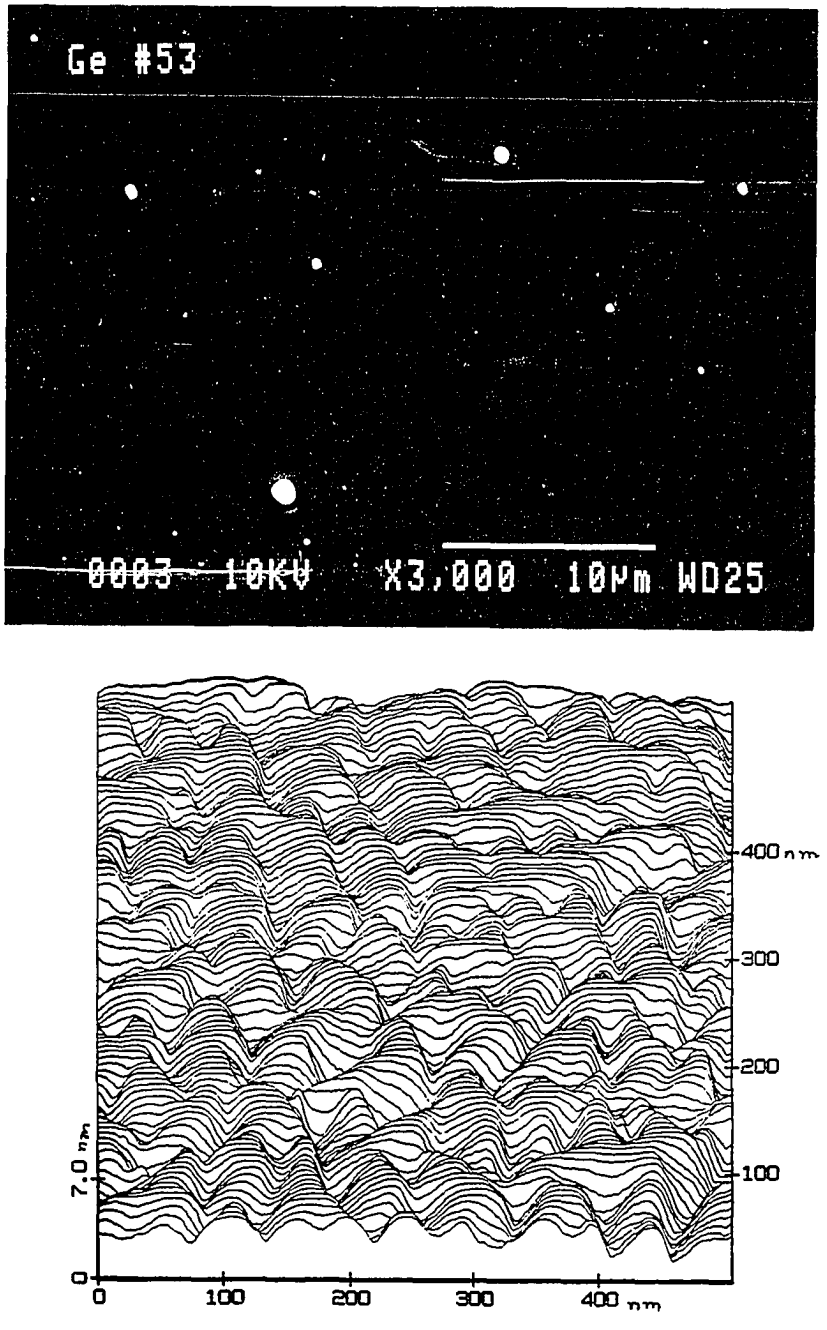

Figure 4.49. Non-annealed surface of germanium imaged with: a) SEM and b) Nanoscope II. The balls in the SEM image are caused by spitting during ICB deposition

between the balls. The balls are believed to have resulted from spitting, which occured during the ICB deposition. Spitting is caused by some of the germanium vapor condensing on the crucible, breaking free from the crucible, and then carried along, in solid form, with the remainder vapor to the substrate. (All the SEM images presented in this Section were taken by Terry Holesinger of the MRC at Iowa State University.)

The Nanoscope II images of the non-annealed portion, as shown in Figure 4.49.b, exhibited features ranging in size from 25 to 110 nm, with an average roughness of 3.74 ± .77 nm. The small balls, as seen in the SEM images, were not evident in the Nanoscope II scans, but this is most likely due to imaging an area of the film with litle or no signs of spitting. However, the annealed images displayed a much different behavior than the non-annealed images, which is shown in Figure 4.50.

The top segment of the figure indicates a region of the sample which contained some large features, roughly 90 to 130 nm in diameter and 4.0 nm in height, separated by flat terrain. The large features are believed to be the small balls caused by spitting, as observed by the SEM. The deviations of the features from a ball-like shape may be an artifact of the scanning because the large features all display the same type of curved high ridge on the right-hand section. The nature of the artifact is not understood, but there was evidence of a similar kind of distortion in images acquired on samples other than 3-ICB #53.

The distortions could also be attributed to a geometric rearrangement of the surface in the vicinity of the balls, plus any

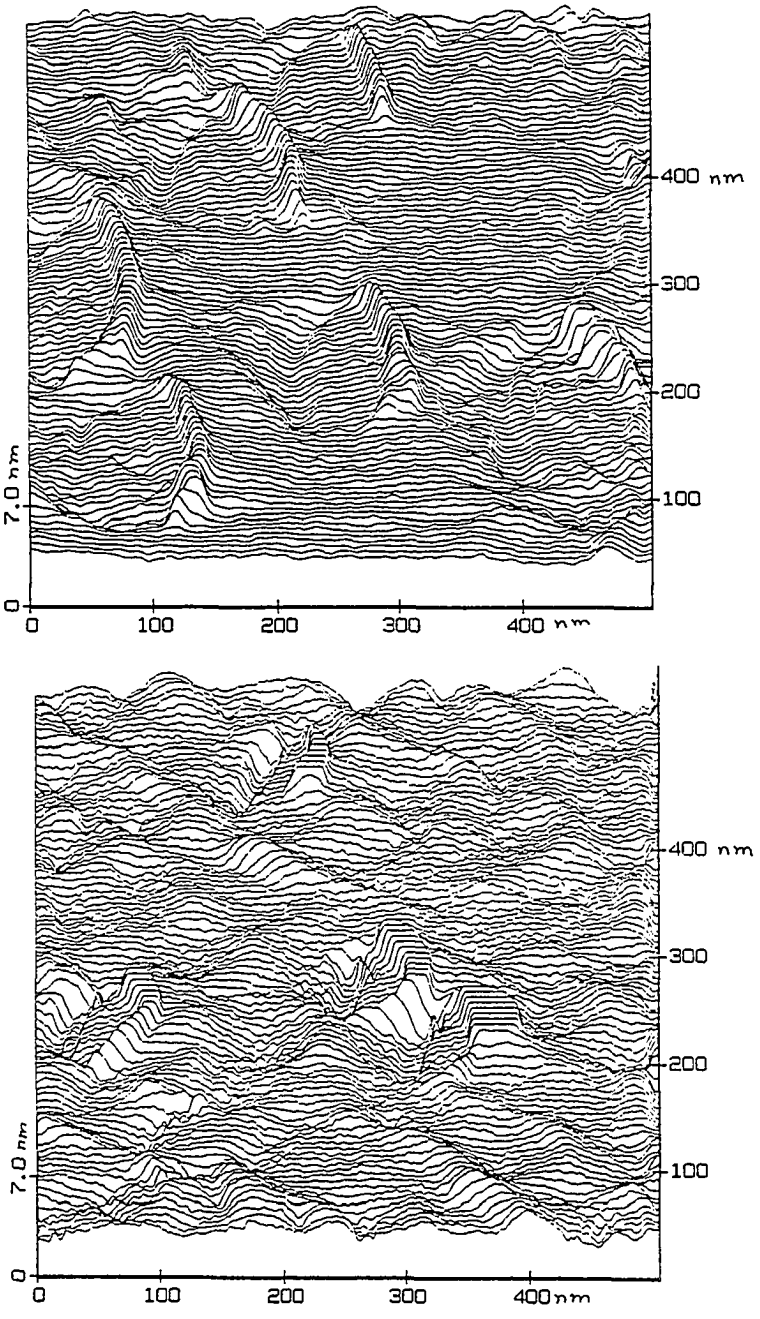

Figure 4.50. Annealed surface of germanium imaged with Nanoscope II showing large features corresponding to the balls seen in Figure 4.49.a. a) and b) are images of two different areas of the same film. In b), island growth can be seen in the background

difference in the geometric or electronic structure of the ball from the film, which would alter the LDOS and, as a result, the tunnel current. Because of limitations of the Nanoscope II in the area of barrier height measurements, additional information on the electronic nature of the features could not be obtained.

The bottom segment of Figure 4.50 shows a different area of the annealed film. The appearance of the balls is still evident, although the balls are slightly smaller (60 to 100 Å) than those in Figure 4.50.a. There is also some indication of island growth because of the shape and size of the background features, which is similar to the SEM photo of an analogous sample, as shown in Figure 4.51.

Despite the inclusion of the balls in the overall roughness, the annealed films (3.57 ± .61 nm) were more smooth than the non-annealed films (3.74 ± .77 nm). Because of a considerable amount of surface dust on the non-annealed films, those films were rinsed with DI, while the annealed films were not cleaned in any manner. Therefore, the difference in roughness between the two films was probably much greater than indicated. By imaging smaller areas of the films (and not including the balls), the difference in roughness became more evident: 2.46 ± .52 nm for the annealed and 3.40 ± .69 for the non-annealed films, using a scan size of 450 Å.

Although the annealed films appeared to contain more surface features, the overall quality of the films were better than the non-annealed samples, as measured by the roughness option. The images also were consistent with SEM images indicating germanium can be imaged in

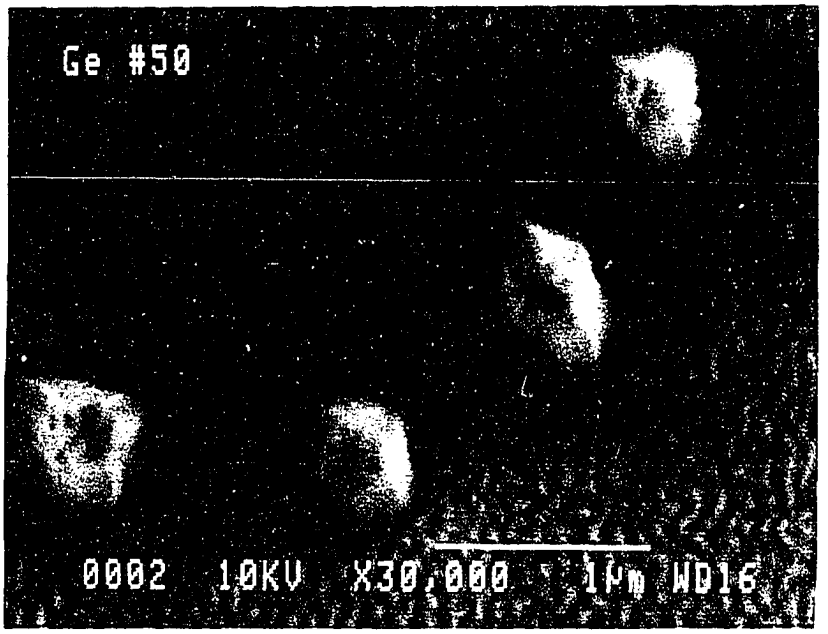

Figure 4.51. SEM image of an ICB deposited film of germanium showing similar behavior as observed in Figure 4.50.b

air, and surface features on the order of tens of nanometers can be resolved successfully.

c. Surface features All the films examined with the Nanoscope II exhibited the same classes of features as in Section IV.C.1.b: islands, ridges and holes, although the size of the features was often much larger (for example, 1300 Å versus 130 Å holes). However, new types of features appeared in many of the scans. Many small area scans (on the order of 100 nm or less) indicated areas of low activity abreast of high activity regions, as shown in Figure 4.52. Close-up views of the border between the two regions, as shown in Figure 4.53, provided no indication as to the physical nature of the activity difference. The difference could be caused by a slight change in the work function from one area to the other, which was investigated by measuring the current versus voltage (I-V) characteristics in the two regions. The I(V) curve, at constant tip-sample spacing, and other spectroscopic means (barrier height and tunneling spectroscopy), showed little distinction between the two locations, providing no resolution as to the basis of the difference.

Occasionally, steps were seen in scans on the order of 75 nm or less. While the height of the steps varied, it always occured in multiples of 1.4 Å, the atomic step height for germanium. Two examples of steps are shown in Figures 4.54 and 4.55. The step in Figure 4.54 runs from top to bottom of the image and is approximately 8.3 Å, or six atomic steps. The step in Figure 4.55 runs from the lower left of the image toward the middle of the scan. The topview for the line scans shown in Figure 4.55.a, is represented in Figure 4.55.b. The vertical

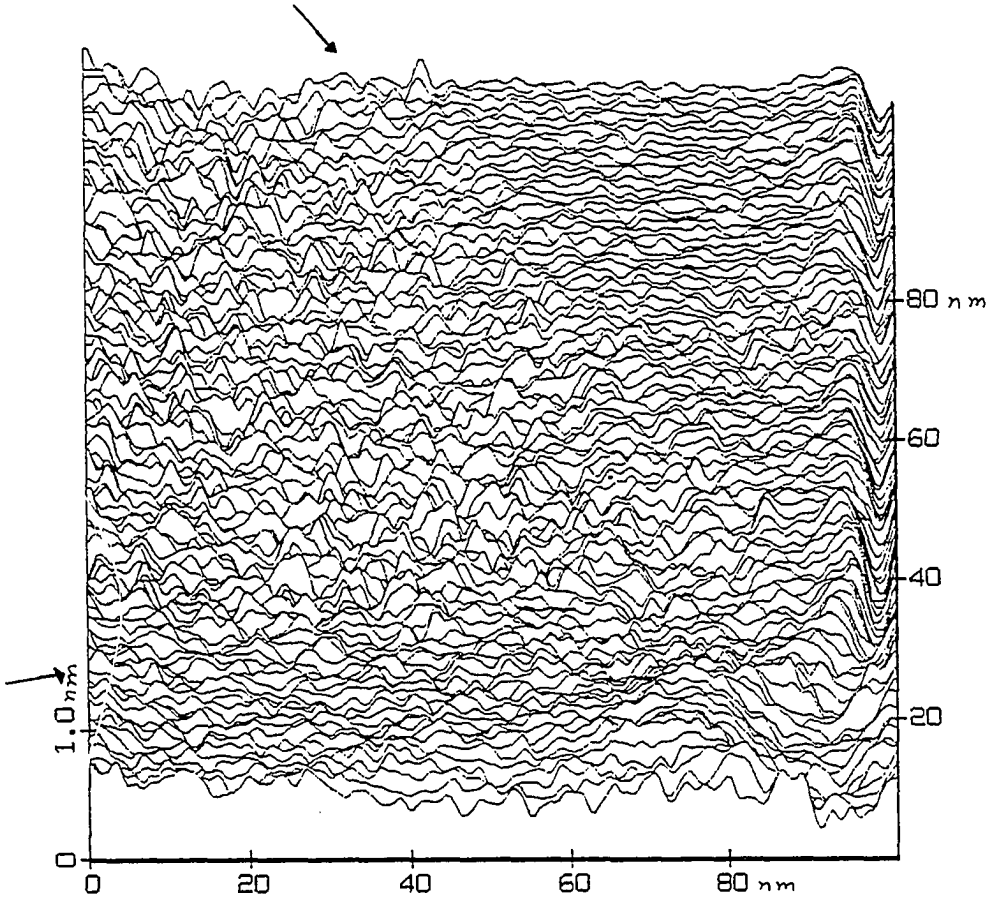

Figure 4.52. Surface feature on germanium showing quiet and noisy imaging side-by-side. The arrows indicate the boundaries between the two regions

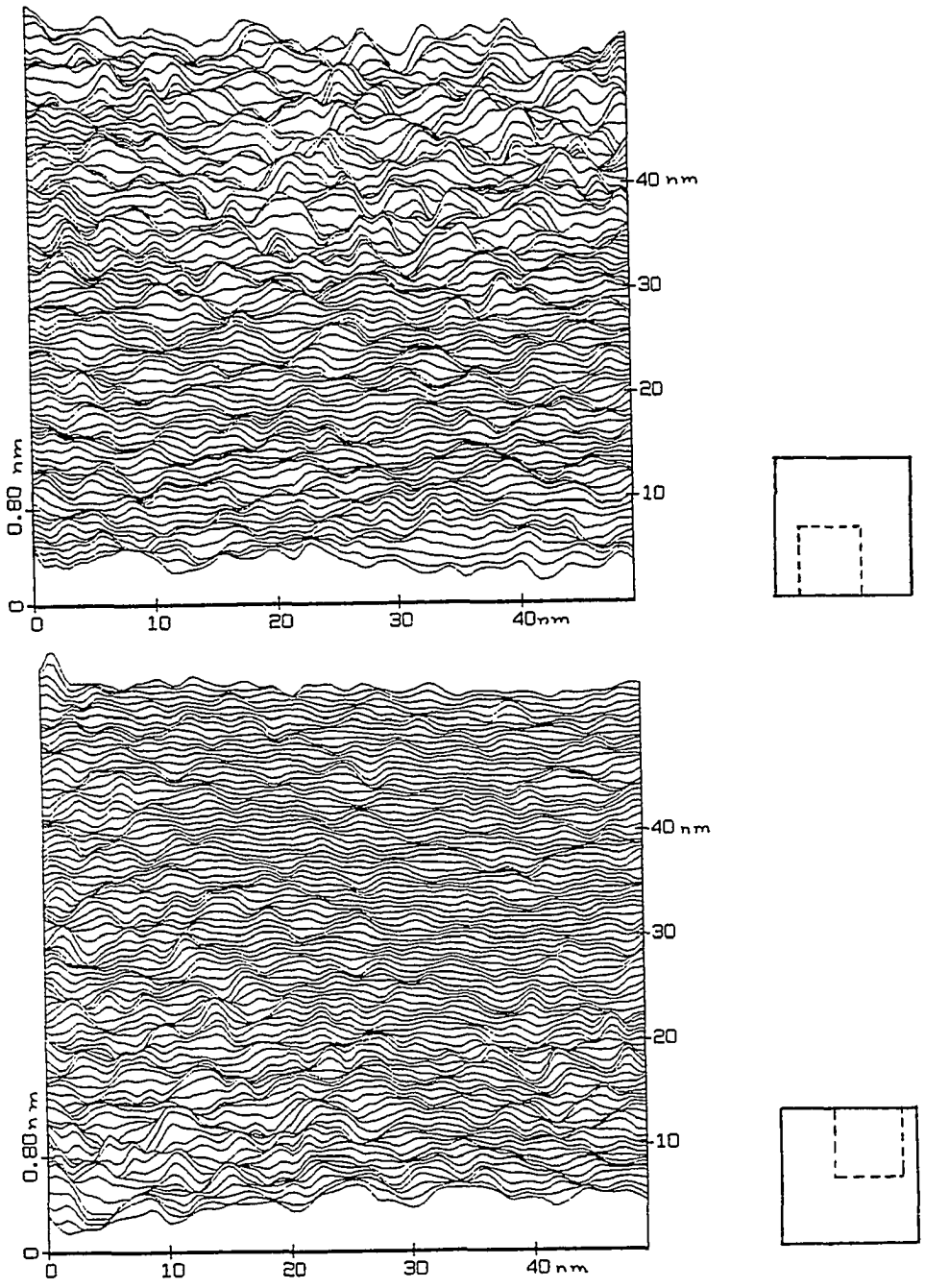

Figure 4.53. Zoomed in views of Figure 4.52 showing the difference in surface activity. The locations of the zoomed-in areas are shown along side, where a) magnifies a portion of the bottom and b) magnifies a portion of the top of Figure 4.52

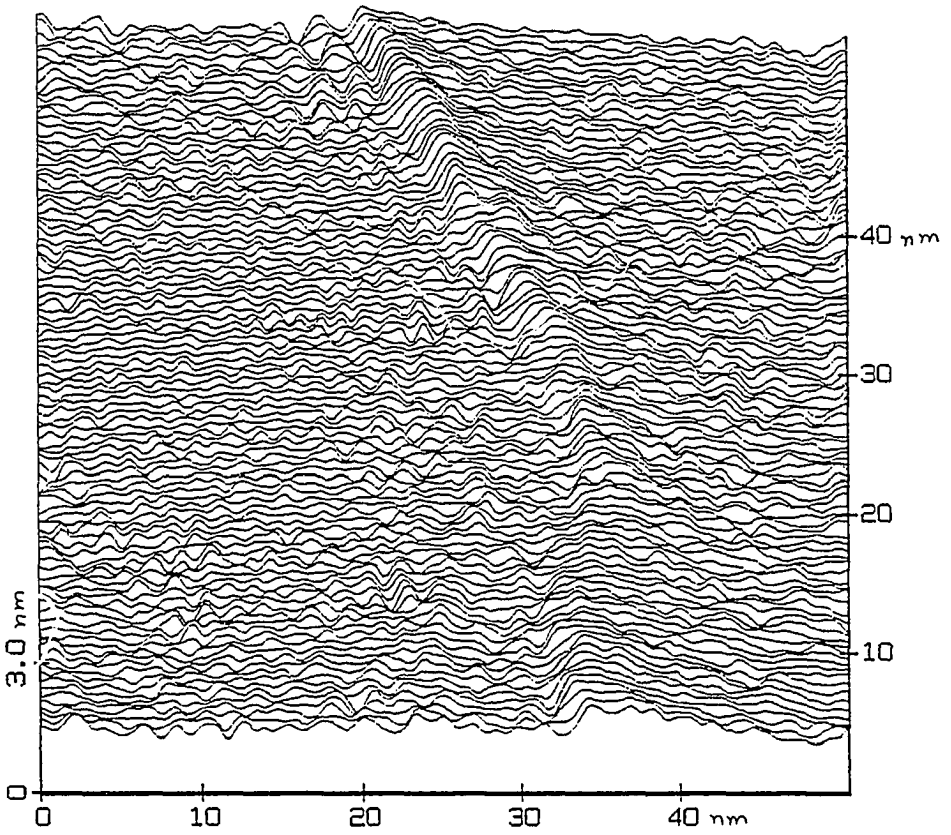

Figure 4.54. Step on germanium surface measuring a height of 8.3 Å (six atomic steps)

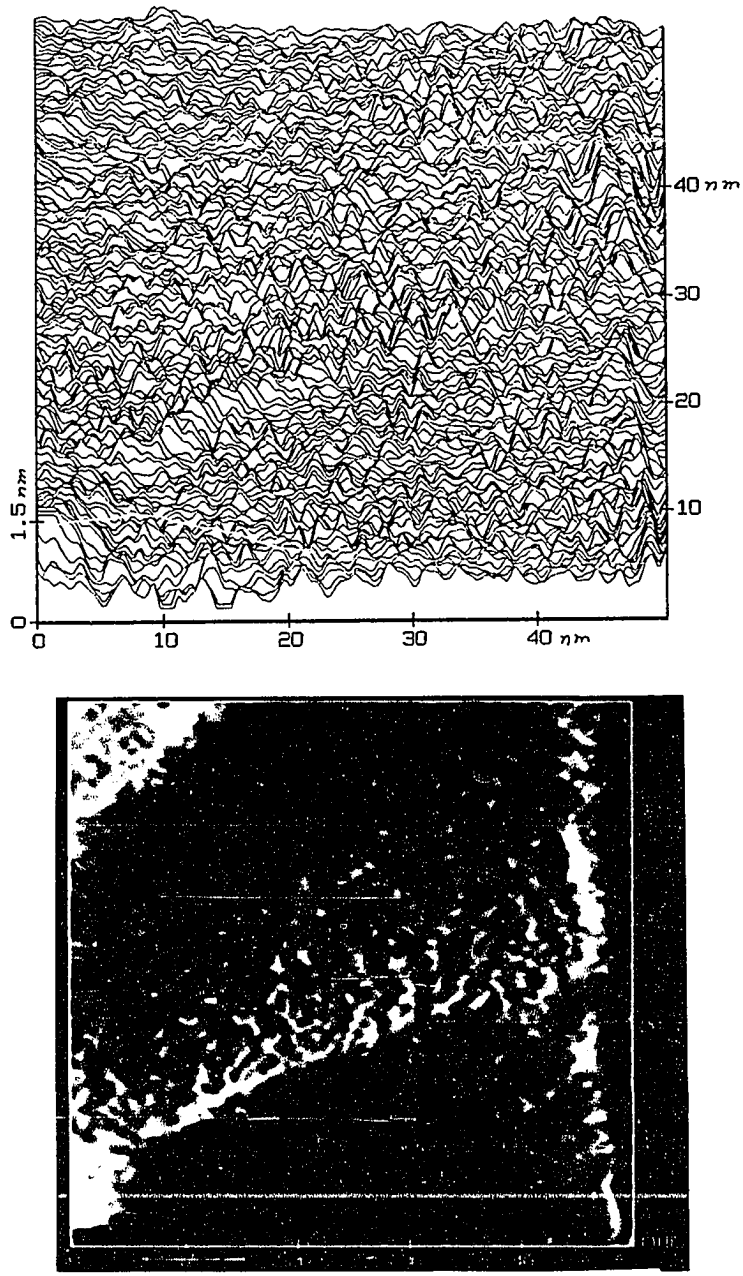

Figure 4.55. Step on germanium surface beginning at a defect (with height 4.3 Å) and gradually ending in the middle of the image. a) is the line scan representation and b) is an overhead view. The upper left-hand corner and the ridge along the right-hand side of the images are artifacts of the imaging

ridge along the right hand portion of the image is an artifact of the scanning. The bright region in the lower left is believed to be a defect, from which the step begins at a height of 4.3 Å, or 3 atomic steps. The step gradually decreases in height until the right hand portion of the image is reached, where the step disappears. The bright region in the upper left of the image was thought also to be a step, but the vertical distances were not uniform. Attempting to move to that location for further investigation was unsuccessful because the tip crashed into the surface.

The majority of the images exhibited no pattern in the appearance of islands, ridges or holes. For the samples imaged, there was a general trend toward smoother films for small film thicknesses, as shown in Table 4.5, which could be caused by difficulties achieving a uniform cluster spreading upon impact with thicker films. No effect of substrate temperature on the surface features was seen with the samples investigated. To better study the effect of deposition conditions on surface features, and film growth, more films need to be examined with the STM. The areas which require more attention are the effects of film thickness, substrate temperature, and cluster acceleration (not examined here) on the types and frequency of surface features, and on surface roughness.

d. Film growth The annealed and non-annealed films of 3-ICB #53, as shown in Figures 4.49 and 4.50, exhibited signs of island growth. With the exclusion of 3-ICB #62, the other ICB films examined also exhibited island growth. 3-ICB #62 was characterized by large rolling

Table 4.5. Ionized cluster beam (ICB) deposition conditions, average roughness, and sample cleaning methods for germanium films examined by Scanning Tunneling Microscopy (STM)

Sample	Cleaning Method	T_{sub}[a] (°C)	Thickness (Å)	Roughness (nm)
ICB #39[b]	DI[c]	500	~ 8,500	3.65 ± .78
ICB #45[b]	DI[c]	300	~ 5,300	2.64 ± .37
3-ICB #20	DI[c]	300	~ 400	2.01 ± .39
3-ICB #53*	DI[c]	350	~ 10,000	3.74 ± .77
3-ICB #53	none	350	~ 10,000	3.57 ± .61
3-ICB #59	none	450	~ 1,500	3.49 ± .81
3-ICB #59	DI[c]	450	~ 1,500	3.22 ± .68
3-ICB #59**	DI[c]	450	~ 1,500	3.31 ± .74
3-ICB #62	none	450	~ 2,700	2.35 ± .44
STM GE2	none	400	~ 100	1.43 ± .19

[a] T_{sub} = substrate temperature.

[b] Films grown by S. McCalmont.

[c] DI = de-ionized water rinse.

* Sample was annealed at 700 °C for 15 min.

** Sample was not imaged until 5 hours after rinsed.

hills, approximately 150 nm wide, as shown in Figure 4.56. Also shown in Figure 4.56 is an SEM image of a similar film, exhibiting the same behavior, but on a much larger scale. By going to higher resolutions, the rolling hills display some features approximately 100 to 200 Å in diameter, and 1.4 Å in height, illustrated in Figure 4.57. These features could correspond to clusters which have impacted the surface and have spread out, but have not yet formed islands.

However, this was not the situation with STM GE2, which clearly exhibits island growth, as seen in Figure 4.58. The islands are clearly defined, and have an average diameter of 55 nm and an average height of 19 Å. The island size is smaller than for other films, as shown by the SEM images in Figure 4.59, but this is attributed to the approximate thickness of 100 Å, instead of 750 Å for the SEM films. The islands for thin films have not yet formed into larger structures.

Barrier height measurements were attempted to investigate any difference between the high and low areas of the film because of earlier work on the locations of germanium oxide. The measurements showed similar structures as did the topography, but the manner in which the Nanoscope II displays and records the information provided no real distinction between the two areas.

3. Conclusions

Although the majority of reported work on germanium has dealt with ordered, reconstructed surfaces, the results from both the McAllister/RHK and the Nanoscope II systems indicate the utility for examining any

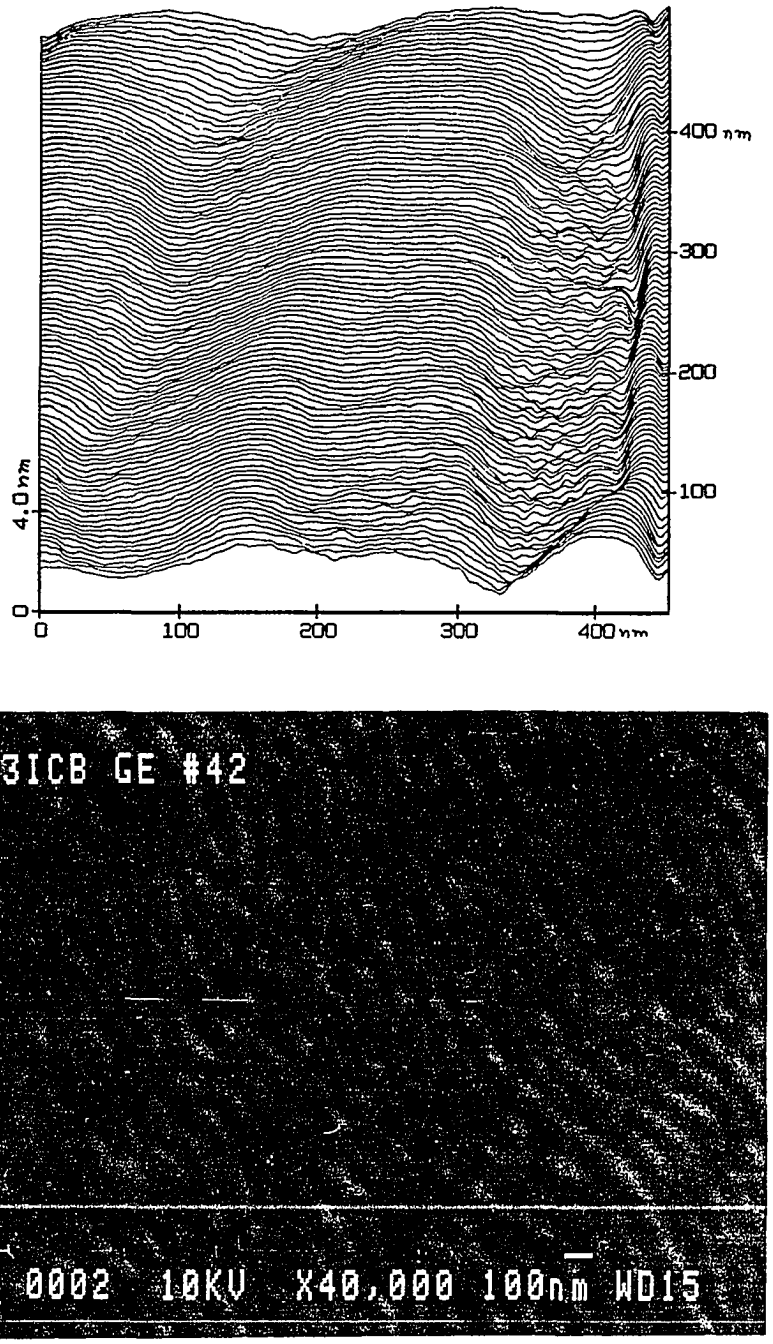

Figure 4.56. Rolling hill features, approximately 150 nm wide, on germanium. a) is the STM image and b) is an SEM image of a similar sample

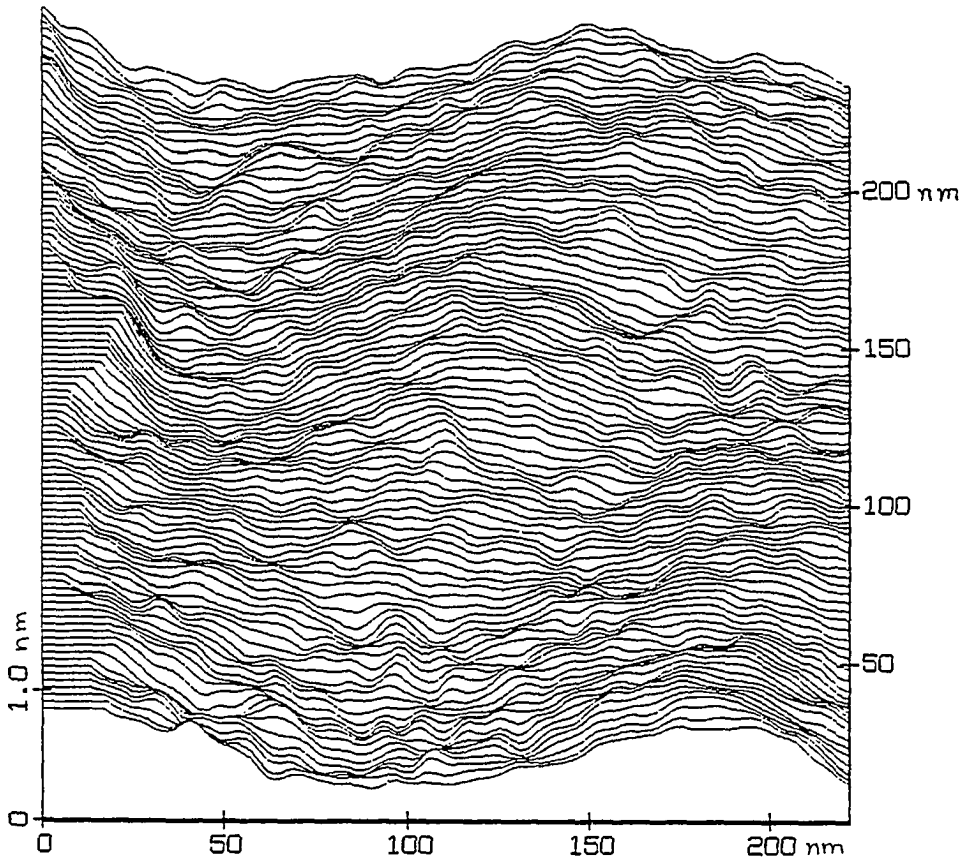

Figure 4.57. Close-up view of one of the hills showing features approximately 100 to 200 Å in diameter. These features could be signs of cluster spreading on the surface

Figure 4.58. Island growth, with an average size of 55 nm. a) is the line scan representation and b) is an overhead view

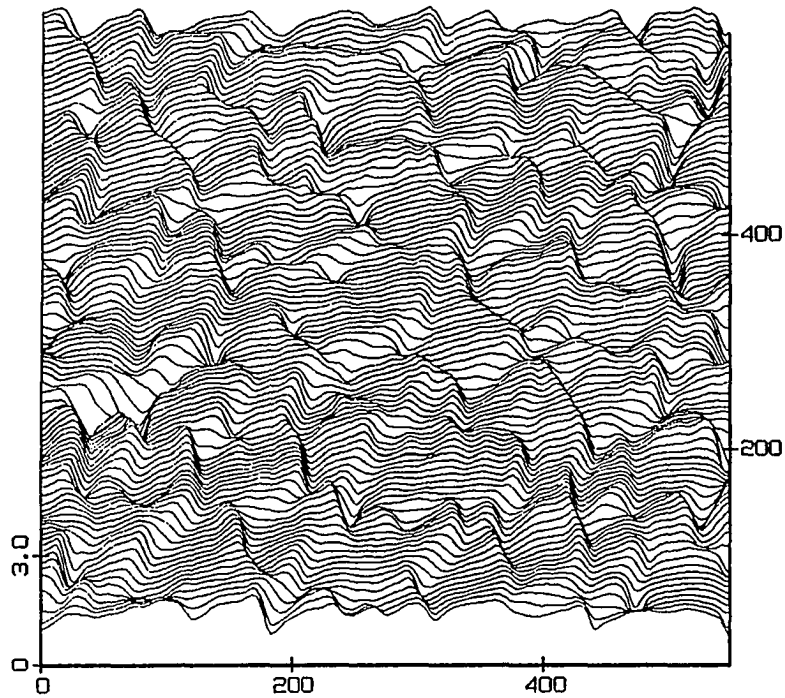
400
200
3.0
0
0
200
400

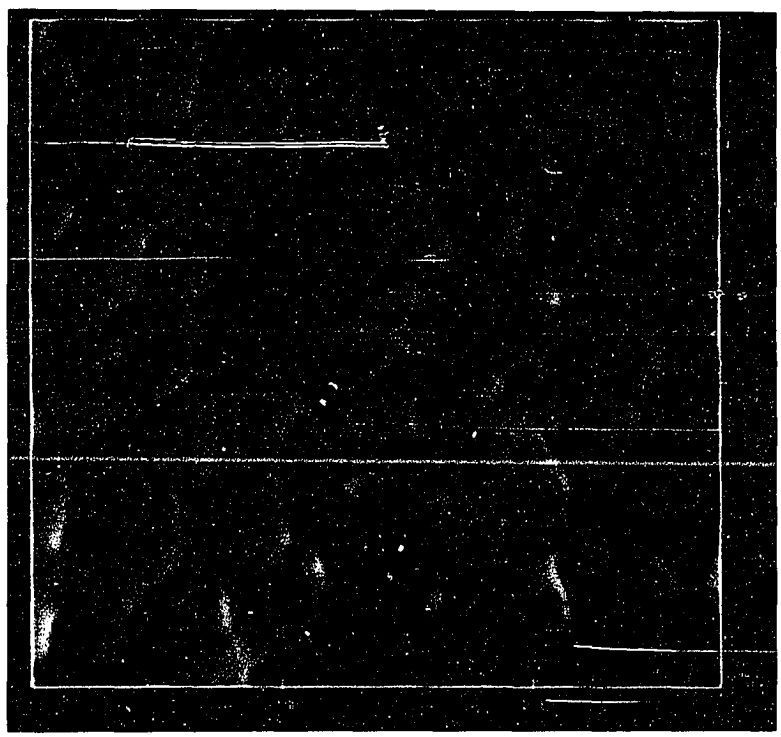

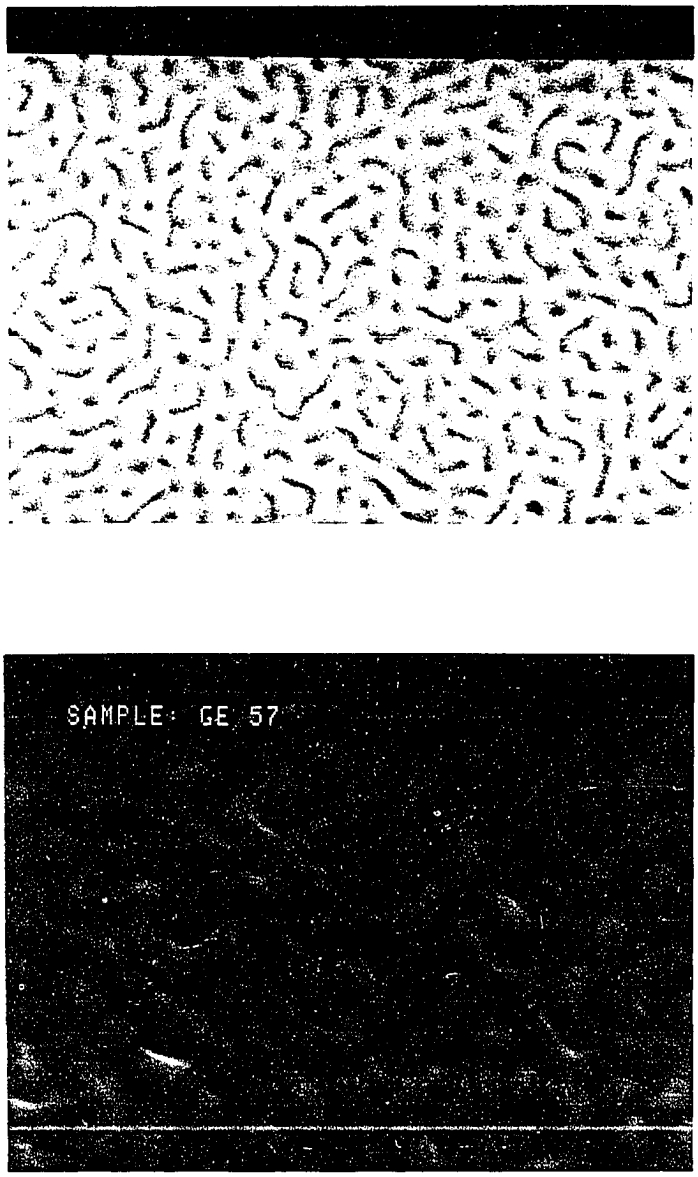

Figure 4.59. SEM images of island growth on germanium films similar to the film shown in Figure 4.58

germanium surface with Scanning Tunnel Microscopy. The germanium films chosen for this work were classified as single crystal by the Ge(400) peak in the X-ray data, but on the nanometer scale, the surface features were more often disordered than ordered, which is supported by the lack of copper K_α splitting of the Ge(400) peak. The features, imaged by both the McAllister/RHK STM and the Nanoscope II, showed similar details, despite the disparity in scan sizes.

Cleaning and annealing the films were seen to have an effect on the overall roughness of the surface, but other cleaning methods need to be investigated to understand the nature of the contamination layer and how to minimize or eliminate it. The electronic effect of the contamination layer on the tunnel current also needs to be explored.

To more fully understand the behavior of the surface, especially as it correlates with ICB deposition conditions, topographic imaging, barrier height measurements and other forms of tunneling spectroscopy need to be performed. Preliminary work in this area has indicated visual similarities exist between spectroscopy and topography, but to date no quantitative information is available.

V. SUMMARY

The Scanning Tunnel Microscope has been shown to be a useful tool for examining the behavior of surfaces with a resolution on the order of tens of nanometers and better. The preliminary work on gold showed the utility of the STM in examining features not seen on the optical scale, without damaging the surface. Investigations of other evaporated films could provide information about the effects of deposition on underlying surfaces, which is important for the manufacturing of microelectronic devices, and for coating insulating materials for SEM and STM studies.

Pyrolytic graphite, either APG or HOPG, was very easy to image with the STM, which permitted imaging on the atomic scale and calibration of the STM system. Because of the simplicity in imaging graphite, it has been customary for many image anomalies to be ignored, but these anomalies are very important for understanding the role of the tip electronic states in imaging a surface. Kobayashi and Tsukada showed the differences in tunneling image shapes can be attributed to different tip orbital states contributing to the current, which were seen in the graphite images obtained with the McAllister/RHK STM. The exact nature of the tip orbitals is not yet clear, but with further investigation into the behavior of peak distortions, it may be possible to calibrate, not only the piezoelectric transducers, but the electronic contribution of the tip as well.

The STM studies of ICB deposited germanium films seemed to raise many more questions than were answered. There appeared to be little

effect of the deposition conditions on the surface features, however, the films that were available for imaging were not a complete sampling of all possible deposition conditions. A systematic approach of examining the films soon after deposition could provide better correlation between the deposition conditions and surface features.

Cleaning and/or annealing the surface reduces the overall roughness of the films. A study of additional methods of cleaning, and other annealing temperatures and times on the surface roughness may lead to effective means of improving the quality of the surface after the film has been grown. This is important, not only for surface analysis, but for the use of the germanium films in microelectronic device fabrication.

Although many new questions have been raised, the STM has been shown to be capable of imaging, in air, films of germanium which are classified as single crystal, but which exhibit few signs of ordering on the scale of tens of nanometers. The use of the STM in conjunction with other surface sensitive techniques, in situ, would provide more information about the germanium surface, without the influences of a contamination layer. In this manner, a correlation between the topographic and the electronic behavior can be obtained as a function of the growth parameters, providing immediate feedback on the conditions required for quality epitaxial films by the ICB process.

VI. REFERENCES

1. W. Schommers and P. von Blanckenhagen in Structure and Dynamics of Surfaces I, edited by W. Schommers and P. von Blanckenhagen (Springer-Verlag, New York, 1987), p. 1.

2. K. H. Reider in Structure and Dynamics of Surfaces I, edited by W. Schommers and P. von Blanckenhagen (Springer-Verlag, New York, 1987), p. 17.

3. A. Zangwill, Physics at Surfaces (Cambridge Univ. Press, New York, 1988), Chap. 3.

4. G. Burns, Solid State Physics (Academic Press, Inc., Orlando, Florida, 1985), Chap. 17.

5. J. K. Gimzewski and A. Humbert, IBM J. Res. Develop., 30, 472 (1986).

6. G. Binnig and H. Rohrer, Helvetica Physica Acta, 55, 726 (1982).

7. R. H. Fowler and L. Nordheim, Proc. R. Soc. London, A119, 173 (1928).

8. L. Esaki, Rev. Mod. Phys., 46, 237 (1974).

9. G. Binnig and H. Rohrer, Rev. Mod. Phys., 59, 615 (1987).

10. C. F. Quate, Physics Today, 39, 26 (1986).

11. E. C. Teague, F. E. Scire, S. M. Backer and S. W. Jensen, Wear, 83, 1 (1982).

12. R. D. Young, J. Ward and F. Scire, Rev. Sci. Instrum., 43, 999 (1972).

13. G. Binnig, H. Rohrer, Ch. Gerber and E. Weibel, Appl. Phys. Lett., 40, 178 (1982).

14. G. Binnig, H. Rohrer, Ch. Gerber and E. Weibel, Phys. Rev. Lett., 50, 120 (1983).

15. G. Binnig, H. Rohrer, F. Salvan, Ch. Gerber and A. Baro, Surf. Sci., 157, L373 (1985).

16. R. M. Tromp, E. J. van Loenen, R. J. Hamers and J. E. Demuth in The Structure of Surfaces II, edited by J. F. van der Veen and M. A. Van Hove (Springer-Verlag, New York, 1988), p. 282.

17. G. Binnig and H. Rohrer, Scientific American, 253, 50 (1985).

18. R. S. Becker, J. A. Golovchenko, E. G. McRae and B. S. Swartzentruber, Phys. Rev. Lett., 55, 2028 (1985).

19. Th. Berghaus, A. Brodde, H. Neddermeyer and St. Tosch, Surf. Sci., 181, 340 (1987).

20. A. L. Robinson, Science, 234, 821 (1986).

21. E. Ruska, Rev. Mod. Phys., 59, 267 (1987).

22. J. G. Simmons, J. Appl. Phys., 34, 1793 (1963).

23. F. Salvan, A. Humbert, P. Dumas and F. Thibaudau, Ann. Phys. Fr., 13, 133 (1988).

24. G. Binnig and H. Rohrer, Surf. Sci., 126, 236 (1983).

25. G. Binnig and H. Rohrer, Physica, 127B, 37 (1984).

26. G. K. Binnig, H. Rohrer, Ch. Gerber and E. Stoll, Surf. Sci., 144, 321 (1984).

27. G. Binnig and H. Rohrer, IBM J. Res. Develop., 30, 355 (1986).

28. I. Giaever, Rev. Mod. Phys., 46, 245 (1974).

29. P. K. Hansma and J. Tersoff, J. Appl. Phys., 61, R1 (1987).

30. R. M. Feenstra, J. A. Stroscio and A. P Fein, Surf. Sci., 181, 295 (1987).

31. R. M Tromp, R. J. Hamers and J. E. Demuth, Science, 234, 304 (1986).

32. R. M Tromp, R. J. Hamers and J. E. Demuth, Phys. Rev., B34, 1388 (1986).

33. R. J. Hamers, R. M. Tromp and J. E. Demuth, Phys. Rev. Lett., 56, 1972 (1986).

34. J. E. Demuth, R. J. Hamers and R. M. Tromp in Interfaces, Superlattices and Thin Films, edited by J. D. Dow and I. K. Schuller (Materials Research Society, Pittsburgh, 1987), p. 1.

35. R. J. Hamers, R. M. Tromp and J. E. Demuth, Surf. Sci., 181, 346 (1987).

36. K. Takayanagi, Y. Tanishiro, M. Takahashi and S. Takahashi, J. Vac. Sci. Technol., A3, 1502 (1985).

37. J. J. Lander and J. Morrison, J. Chem. Phys., 37, 4 (1962).

38. F. J. Himpsel and Th. Fauster, J. Vac. Sci. Technol., A2, 815 (1984).

39. R. J. Hamers, Annu. Rev. Phys. Chem., 40, 531 (1989).

40. M. A. McCord and R. F. W. Pease, J. Vac. Sci. Technol., B4, 86 (1985).

41. M. A. McCord and R. F. W. Pease, Appl. Phys. Lett., 50, 569 (1986).

42. D. W. Abraham, H. J. Mamin, E. Ganz and J. Clarke, IBM J. Res. Develop., 30, 492 (1986).

43. J. S. Foster, J. E. Frommer and P. C. Arnett, Nature, 331, 324 (1988).

44. R. S. Becker, J. A. Golevchenko and B. S. Swartzentruber, Nature, 325, 419 (1987).

45. G. Travaglini, H. Rohrer, M. Amrein and H. Gross, Surf. Sci., 181, 380 (1987).

46. R. V. Coleman, B. Giambattista, P. K. Hansma, A. Johnson, W. W. McNairy and C. G. Slough, Advances in Physics, 37, 559 (1988).

47. S. A. Elrod, A. Bryant, A. L. de Lozanne, S. Park, D. Smith and C. F. Quate, IBM J. Res. Develop., 30, 387 (1986).

48. J. R. Kirtley, S. I. Raider, R. M. Feenstra and A. P. Fein, Appl. Phys. Lett., 50, 1607 (1987).

49. H. G. LeDuc, W. J. Kaiser and J. A. Stern, Appl. Phys. Lett., 50, 1921 (1987).

50. G. Binnig, C. F. Quate and Ch. Gerber, Phys. Rev. Lett., 56, 930 (1986).

51. N. A. Burnham and R. J. Colton, J. Vac. Sci. Technol., A7, 2906 (1989).

52. R. Guckenberger, C. Kosslinger, R. Gatz, H. Breu, N. Levai and W. Baumeister, Ultramicroscopy, 25, 111 (1988).

53. S. Park and C. F. Quate, Appl. Phys. Lett., 48, 112 (1986).

54. R. V. Coleman, B. Drake, P. K. Hansma and C. G. Slough, Phys. Rev. Lett., 55, 394 (1985).

55. D. P. E. Smith and G. Binnig, Rev. Sci. Instrum., 57, 2630 (1986).

56. R. Sonnenfeld and P. K. Hansma, Science, 232, 211 (1986).

57. R. Sonnenfeld and B. Schardt, Appl. Phys. Lett., 49, 1172 (1986).

58. J. Schneir and P. K. Hansma, Langmuir, 3, 1025 (1987).

59. H. K. Wickramasinghe, Scientific American, 261, 98 (1989).

60. R. Pool, Science, 247, 636 (1990).

61. E. Schrodinger, Ann. Phys., 79, 631 (1926)

62. D. Bohm, Quantum Theory (Prentice-Hall, Inc., New York, 1951), Chap. 12.

63. J. Bardeen, Phys. Rev. Lett., 6, 57 (1961).

64. E. L. Wolf, Principles of Electron Tunneling Spectroscopy (Oxford University Press, New York, 1985), Chap. 2

65. C. Noguera, J. Phys. France, 50, 2587 (1989).

66. J. Tersoff and D. R. Hamann, Phys. Rev., B31, 805 (1985).

67. J. Tersoff and D. R. Hamann, Phys. Rev. Lett., 50, 1998 (1983).

68. R. M. Feenstra and J. A. Stroscio, Physica Scripta, T19, 55 (1987).

69. N. D. Lang, Phys. Rev. Lett., 55, 230 (1985).

70. N. D. Lang, Phys. Rev. Lett., 56, 1164 (1986).

71. N. D. Lang, in Springer Series in Surface Sciences, Vol. 14, edited by F. W. de Wetter (Springer-Verlag, Berlin, 1988), p. 216.

72. E. Stoll, J. Micros. & Spectros., 9, 213 (1984).

73. R. M. Feenstra, J. A. Stroscio and A. P. Fein, Surf. Sci., 181, 295 (1987).

74. T. E. Feuchtwang, P. H. Cutler and N. M. Miskovsky, Phys. Lett., 99A, 167 (1983).

75. N. Garcia, C. Ocal and F. Flores, Phys. Rev. Lett., 50, 2002 (1983).

76. A. Baratoff, Physica, 127B, 143 (1984).

77. E. Stoll, A. Baratoff, A. Selloni and P. Carnevali, J. Phys. C, 17, 3073 (1984).

78. C. J. Chen, J. Vac. Sci. Technol., A6, 319 (1988).

79. T. E. Feuchtwang, P. H. Cutler and E. Kazes, J. de Physique, C9, 111 (1984).

80. A. A. Lucas, H. Morawitz, G. R. Henry, J. P. Vigneron, Ph. Lambin, P. H. Cutler and T. E. Feuchtwang, Phys. Rev., B37, 10708 (1988).

81. G. Binnig and D. P. E. Smith, Rev. Sci. Instrum., 57, 1688 (1986).

82. B. Drake, R. Sonnenfeld, J. Schneir, P. K. Hansma, C. G. Slough and R. V. Coleman, Rev. Sci. Instrum., 57, 441 (1986).

83. B. L. Blackford, D. C. Dahn and M. H. Jerico, Rev. Sci. Instrum., 58, 1343 (1987).

84. G. F. A. van de Walle, B. J. Nelissen, L. L. Soethout and H. van Kempen, Fresnius Z. Anal. Chem., 329, 108 (1987).

85. K. Besocke, Surf. Sci., 181, 145 (1987).

86. J. E. Demuth, R. J. Hamers, R. M. Tromp and M. E. Wellend, IBM J. Res. Develop., 30, 396 (1986).

87. A. Stemmer, A. Engel, R. Haring, R. Reichelt and U. Aebi, Ultramicroscopy, 25, 171 (1988).

88. J. Vancea, G. Reiss, F. Schneider, K. Bauer and H. Hoffmann, Surf. Sci., 218, 108 (1989).

89. C. E. D. Chidsey, D. N. Loiacono, T. Sleator and S. Nakahara, Surf. Sci., 200, 45 (1988).

90. J. Gomez, L. Vazquez, A. M. Baro, C. Alonso, E. Gonzalez, J. Gonzalez-Velasco and A. J. Arvia, J. Electroanal. Chem., 240, 77 (1988).

91. B. T. Kelly, Physics of Graphite (Applied Science, London, 1981), p.267.

92. A. W. Moore, in Chemistry and Physics of Carbon, Vol. 11, edited by P. L. Walker, Jr. and P. A. Thrower (Dekker, New York, 1973), p. 69.

93. G. Binnig, H. Fuchs, Ch. Gerber, H. Rohrer, E. Stoll and E. Tosatti, Europhys. Lett., 1, 31 (1986).

94. S. Park and C. F. Quate, Appl. Phys. Lett., 49, 936 (1986).

95. J. Tersoff, Phys. Rev. Lett., 57, 440 (1986).

96. S. Ciraci, Surf. Sci., 181, 126 (1987).

97. A. Selloni, P. Carnevali, E. Tosatti and C. D. Chen, Phys. Rev., B31, 2602 (1985).

98. C. Horie and H. Miyazaki, J. de Physique, C6, 85 (1987).

99. D. Tomanek and S. G. Louie, Phys. Rev., B37, 8327 (1988).

100. I. P. Batra and S. Ciraci, J. Vac. Sci. Technol., A6, 313 (1988).

101. J. M. Soler, A. M. Baro, N. Garcia and H. Rohrer, Phys. Rev. Lett., 57, 444 (1986).

102. O. Albrektsen, L. L. Madsen, J. Mygind and K. A. Morch, J. Phys. E, 22, 39 (1988).

103. A. Bryant, D. P. E. Smith and C. F. Quate, Appl. Phys. Lett., 48, 832 (1986).

104. A. Bryant, D. P. E. Smith, G. Binnig, W. A. Harrison and C. F. Quate, Appl. Phys. Lett., 49, 936 (1986).

105. O. Marti, B. Drake, S. Gould and P. K. Hansma, J. Vac. Sci. Technol., A6, 2089 (1988).

106. O. Marti, B. Drake and P. K. Hansma, Appl. Phys. Lett., 51, 484 (1987).

107. R. J. Colton, S. M. Baker, R. J. Driscoll, M. G. Youngquist, J. D. Baldeschwieler and W. J. Kaiser, J. Vac. Sci. Technol., A6, 349 (1988).

108. J. Schneir, R. Sonnenfeld, P. K. Hansma and J. Tersoff, Phys. Rev., B34, 4979 (1986).

109. J. E. Yao and Y. K. Jiao, J. Vac. Sci. Technol., A8, 508 (1990).

110. H. A. Mizes, S. Park and W. A. Harrison, Phys. Rev., B36, 4491 (1988).

111. T. R. Albrecht and C. F. Quate, J. Appl. Phys., 62, 2599 (1987).

112. C. M. Mate, G. M. McClelland, R. Erlandsson and S. Chiang, Phys. Rev. Lett., 59, 1942 (1987).

113. G. E. Poirier and J. M. White, Rev. Sci. Instrum., 60, 3113 (1989).

114. D. P. E. Smith, G. Binnig and C. F. Quate, Appl. Phys. Lett., 49, 1166 (1986).

115. K. Sakamaki, K. Itoh, A. Fujishima, Y. Gohshi and H. Nakagawa, Bull. Chem., 62, 2890 (1989).

116. S. L. Tang, J. Bokov and R. H. Storz, Appl. Phys. Lett., 52, 182 (1988).

117. E. Stoll and O. Marti, Surf. Sci., 181, 222 (1987).

118. K. Kobayashi and M. Tsukada, J. Phys. Soc. Jpn., 58, 2238 (1989).

119. M. Tsukada and K. Kobayashi, J. Vac. Sci. Technol., A8, 160 (1990).

120. M. Tsukada and K. Kobayashi, J. Vac. Sci. Technol., A8, 170 (1990).

121. S. Ohnishi and M. Tsukada, Sol. St. Comm., 71, 391 (1989).

122. T. Takagi, in Ion Implantation and Ion Beam Processing in Materials, edited by G. K. Hubler, O. W. Holland, C. R. Clayton and C. W. White (North Holland, New York, 1984), p. 501.

123. R. Biswas, G. S. Grest and C. M. Soukoulis, Phys. Rev., B38, 8154 (1988).

124. I. Kwon, R. Biswas, G. S. Grest and C. M. Soukoulis, Phys. Rev., B41, 3678 (1990).

125. J. S. McCalmont, H. R. Shanks and K. M. Lakin, J. Vac. Sci. Technol., A5, 1911 (1987).

126. J. A. Kubby, J. E. Griffith, R. S. Becker and J. S. Vivkers, Phys. Rev., B36, 6079 (1987).

127. H. J. W. Zandvliet and A. van Silfout, Surf. Sci., 211/212, 544 (1989).

128. R. Becker and J. Vickers, J. Vac. Sci. Technol., A8, 226 (1990).

129. R. M. Feenstra and G. S. Oehrlein, Appl. Phys. Lett., 47, 97 (1985).

VII. ADDITIONAL REFERENCES

This section has been added to provide additional information about equipment and research pertaining to the STM that is beyond the scope of this paper.

A. Proceedings of STM Conferences

IBM J. Res. Develop., 30 (1986).

J. Microcop., 152 (1989).

J. Vac. Sci. Technol., A6 (1988).

J. Vac. Sci. Technol., A8 (1990).

Surface Science, 181 (1987).

B. Review Articles

T. E. Feuchtwang and P. H. Cutler, Physica Scripta, 35, 132 (1989).

J. J. Hren and G. Shedd, Ultramicroscopy, 24, 169 (1988).

Y. Kuk and P. J. Silverman, Rev. Sci. Instrum., 60, 165 (1989).

C. Tunneling

R. P. Bell, The Tunnel Effect In Chemistry (Chapman and Hall, New York, 1980).

E. Burstein and S. Lundqvist, editors, Tunneling Phenomena in Solids (Plenum Press, New York, 1969).

C. B. Duke, Tunneling in Solids (Academic Press, New York, 1969).

P. K. Hansma, editor, Tunneling Spectroscopy (Plenum Press, New York, 1982).

T. Wolfram, editor, Inelastic Electron Tunneling Spectroscopy (Springer-Verlag, New York, 1978).

VIII. ACKNOWLEDGEMENTS

The long and arduous process of obtaining my doctoral degree would have been more difficult were it not for the love and support of many individuals. I would like now to express my heartfelt appreciation to:

My advisor, Howard Shanks, for his support and encouragement;

Those at the Microelectronics Research Center who were instrumental in helping me complete my research, especially: Ruth Shinar, for her listening skills, and words of encouragement; and Dave Turner, for his help with computer programs and ICB films;

Dr. Eric Henderson of the Zoology Department at Iowa State University for the timely use of his Nanoscope II. Without his generous nature and help, the results section would have suffered;

My family for their continual belief in and support (at times, financial support) of my efforts. I particularly thank my mother for her never-ending words of wisdom, encouragement and love;

My friends, for their patience and understanding during the trying times, especially: my belladas, Kathy, for always believing in me and for reminding me of my options; and Chris, for those much needed distractions at all hours of the day (and night);

Dr. Brad Paulson for proofreading my dissertation, supplying peanut M & Ms, and bestowing his friendship on me; and

The Supreme Being, without whom, none of this would have been possible.